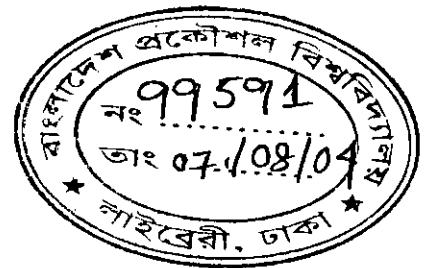
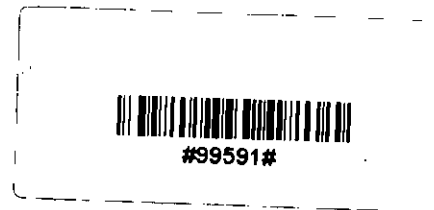


Study of Magnetoresistive Properties of Double Layer Perovskite Manganite



Md. Mahabubar Rahman Shah



*A Dissertation submitted to the Department of Physics,
Bangladesh University of Engineering & Technology, Dhaka, in
Partial fulfillment for the degree of Master of Philosophy*

**Department of Physics
Bangladesh University of Engineering & Technology,
Dhaka 1000, Bangladesh
June 2004**

Candidate's Declaration

It is hereby declared that this thesis or any part of it has not been submitted elsewhere for the award of any degree or diploma.

M. Rahman Shah

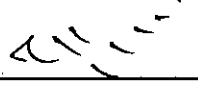
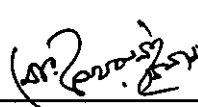


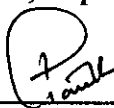
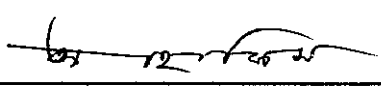
Md. Mahabubar Rahman Shah

**Bangladesh University of Engineering & Technology,
Department of Physics, Dhaka 1000, Bangladesh**

Certification of Thesis

The thesis titled "Study of Magnetoresistive Properties of Double Layer Perovskite Manganite" submitted by **Md. Mahabubar Rahman Shah**, Roll No : 100014002F, Session October'2000, has been accepted as satisfactory in partial fulfillment of the requirement for the degree of **Master of Philosophy** in Physics on June 26, 2004.

BOARD OF EXAMINERS

1. 
(_____)
Dr. Mominul Huq (Supervisor) Chairman
Professor, Department of Physics, BUET
2. 
(_____)
Dr. Md. Fakhru Islam (Co Supervisor) Member
Associate Professor,
Department of Materials & Metallurgical Engineering, BUET
3. 
(_____)
Dr. Mominul Huq Member
Professor & Head, Department of Physics, BUET (Ex-officio)
4. 
(_____)
Dr. Md. Abu Hashan Bhuiyan Member
Professor, Department of Physics, BUET
5. 
(_____)
Dr. Feroz Alam Khan Member
Associate Professor, Department of Physics, BUET
6. 
(_____)
Dr. A. K. M. Abdul Hakim Member
Principal Engineer, Magnetic Materials Division (External)
Atomic Energy Center, Dhaka.

ACKNOWLEDGEMENTS

This Research Work has been carried out under the continuous supervision of Professor Dr. Mominul Huq, Head, Department of Physics, Bangladesh University of Engineering & Technology (BUET). It is an immense pleasure to express my profound sense of gratitude, sincere appreciation and indebtedness to my reverend supervisor for his scholastic and indispensable guidance, keen interest, constructive suggestion and constant inspiration through out the research work.

I would like to express my indebtedness to my co-supervisor Dr. Md. Fakhru Islam, Associate Professor, Department of Materials & Metallurgical Engineering, BUET for his help in preparing the specimens & constructive suggestions.

I would like to thank Professor Giasuddin Ahmed, Professor M.A. Asgar, Professor M.A.H Bhuiyan, Professor Nazma Zaman, Professor Jiban Podder, Department of Physics, BUET for their encouragement during this research work.

I am also grateful to Mrs. D.A. Ahmed, Dr. Md. Feroz Alam Khan, Mrs. Fahima Khanam, Dr. A.K.M. Akther Hossain, Dr. Md. Mostak Hossain, Dr. Md. Nazrul Islam, Mrs. Afia Begum, Mr. Rafi Uddin of Physics Department, BUET for their encouragement and help during this work. I am very grateful to BUET authority for providing the financial support for this research work.

I would also convey my sincere thanks to Head, Materials & Metallurgical Engineering (MME) Department, BUET for permitting me to use the facilities of high temperature furnace and X-ray diffractometry. I would also like to thank Mr. Yusuf Khan, Mr. Tariq Chowdhury and Mr. Tamjid Chowdhury of MME Department, BUET for their encouragement and occasional help.

I would like to thank the staff of Physics Department, BUET for their occasional help.

I wish to offer my sincere thanks to all my friends and students of Physics Department, BUET for their encouragement and inspiration.

Finally, I would like to express my heartfelt gratitude to my parents and other family members for their constant support and encouragement during this study.

The author

CONTENTS

	Pages
CHAPTER 1 : Introduction	1
1.1 Objectives	3
1.2 Summary of the thesis	3
CHAPTER 2 : Literature Review	5
2.1 Introduction	5
2.2 Materials	6
2.2.1 Structure and electronic spectrum	6
2.2.2 Layered compounds	12
2.3 Properties of CMR materials	14
2.3.1 Intrinsic properties	14
2.3.2 The paramagnetic phase	14
2.4 Transport properties	18
2.4.1 High temperature transport in perovskites- evidence for polarons	18
2.4.2 High-temperature resistivity, thermopower	18
2.4.3 Low-temperature transport-low field magnetoresistance	20
2.4.4 Low-temperature resistivity inter grain transport, noise	20
2.4.5 Low-temperature resistivity-intrinsic	22
2.5 Theory of Manganites systems	23
2.5.1 Double exchange model	23
2.5.2 Orbital ordering from superexchange	25
2.5.3 Orbital ordering	26
2.6 Orbital state study of Mn in CMR material by magnetic compton profile measurement	28
2.7 Effect of doping Ca on polaron hopping in $\text{LaSr}_2\text{Mn}_2\text{O}_7$	31
2.8 O(Mn) vibrational bands in double-layered manganites	34
2.8.1. First-order Raman scattering	35

2.8.2.	Second-order Raman scattering	37
2.9	Local structure of the CMR oxides from polarized EXAFS	40
2.10	Manganite-based device	43
CHAPTER 3 : Sample Preparation and Experimental Techniques		49
3.1	Sample Preparation	49
3.1.1	Solid state reaction method	49
3.1.2	Solution method	49
3.1.3	Melt-quenched or glass ceramic method	49
3.1.4	Thin film method	50
3.2	Preparation of the present samples	50
3.3	Calcinations schedule	52
3.4	Preparation of pellets	52
3.5	Sintering and oxidation of the pellets	52
3.6	Construction of a liquid nitrogen cryostat	52
3.7	Construction of electromagnet	54
3.8	Construction of the sample rod	57
3.9	Magnetoresistance measurement set-up	59
3.10	The van der Pauw technique	61
3.11	Magnetoresistance	63
CHAPTER 4 : Results and Discussion		64
4.1	Polycrystalline $(La_{2-x}Nd_x)(Ba_{1-y}Ca_y)Mn_2O_7$	64
4.1.1	X-ray diffraction analysis	65
4.2	Microstructures of $(La_{2-x}Nd_x)(Ba_{1-y}Ca_y)Mn_2O_7$	70
4.3	DC electrical resistivity	73
4.3.1	DC electrical resistivity of $(La_{2-x}Ba_x)BaMn_2O_7$	73
4.3.2	DC electrical resistivity of $(La_{2-x}Nd_x)BaMn_2O_7$	77
4.3.3	DC electrical resistivity of $(La_{1.8}Nd_{0.2})(Ba_{1-y}Ca_y)Mn_2O_7$	80
4.4	Magnetoresistance	84
4.4.1	Magnetoresistance of $(La_{2-x}Ba_x)BaMn_2O_7$	84

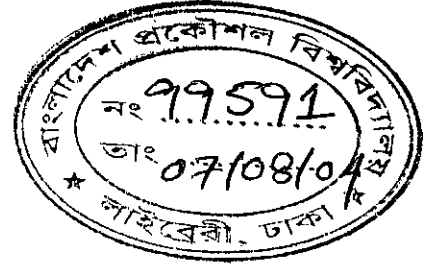
4.4.1.1	$MR(T)$ for $(La_{2-x}Ba_x)BaMn_2O_7$	84
4.4.1.2	$MR(H)$ for $(La_{2-x}Ba_x)BaMn_2O_7$	86
4.4.2	Magnetoresistance of $(La_{2-x}Nd_x)BaMn_2O_7$	89
4.4.2.1	$MR(T)$ for $(La_{2-x}Nd_x)BaMn_2O_7$	89
4.4.2.2	$MR(H)$ for $(La_{2-x}Nd_x)BaMn_2O_7$	91
4.4.3	Magnetoresistance of $(La_{1.8}Nd_{0.2})(Ba_{1-y}Ca_y)Mn_2O_7$	94
4.4.3.1	$MR(T)$ for $(La_{1.8}Nd_{0.2})(Ba_{1-y}Ca_y)Mn_2O_7$	94
4.4.3.2	$MR(H)$ for $(La_{1.8}Nd_{0.2})(Ba_{1-y}Ca_y)Mn_2O_7$	96
4.5	Explanation of the extrinsic MR	99
CHAPTER 5 : Conclusions		101

ABSTRACT

The polycrystalline samples of $(\text{La}_{2-x}\text{Nd}_x)(\text{Ba}_{1-y}\text{Ca}_y)\text{Mn}_2\text{O}_7$ were synthesized by using the solid state reaction method. Powders of La_2O_3 (99.99%), CaCO_3 (99.9%), Nd_2O_3 (99.9%), MnO_2 (99.9%) and BaCO_3 (99.9%) were mixed thoroughly in an appropriate amount in dry and acetone media. The mixed powders were calcined at high temperature 1100°C for 72 hours with intermediate grinding after 24 hours. The calcined powder was ground thoroughly to fine powder and pressed uniaxially into pellets of 12 mm diameter and 1-3 mm thick under a pressure of 12000 P.S.I for about 1 to 3 minutes. The prepared pellets were sintered at 1400°C and 1500°C in air for 5 hours. The structural characterization was carried out using an X-ray diffractometry. All samples were of single phase within the resolution of the X-ray measurements. The dc electrical resistivity of the samples was measured by using the four-point probe technique from room temperature down to liquid nitrogen temperature in zero applied field and in presence of 0.65T magnetic field. The normalized resistivity $\rho(T)/\rho(RT)$ as a function of temperature for various $(\text{La}_{2-x}\text{Nd}_x)(\text{Ba}_{1-y}\text{Ca}_y)\text{Mn}_2\text{O}_7$ polycrystalline samples were measured. It was observed that most of the samples show metal-insulator ($M-I$) transition at certain temperature, T_p . The $M-I$ transition temperature, T_p and the value of $\rho(T)/\rho(RT)$ curves were found to vary with compositions. The variation of $M-I$ transition temperature, T_p and $\rho(T)/\rho(RT)$ are due to the charge transfer $\text{Mn}^{3+}-\text{O}-\text{Mn}^{4+}$, substitution of the trivalent by divalent cation and also different atomic size of the molecules. It was also observed that as the sintering temperature increase, resistivity of the samples decrease throughout the measured temperature range. This is probably due to the decrease of pores and increase of grain size of the samples, which result in the decrease in the grain boundary and hence decrease in resistivity of the samples. In the presence of 0.65T magnetic field, $M-I$ transition temperature enhance by few Kelvin as the magnetic field accelerate magnetic ordering. This is suggested to be due to the fractional ordering of magnetic moment in the paramagnetic regime hence change the transition temperature, T_p due to the applied magnetic field. The magnetoresistance (MR) as a function of temperature, $MR(T)$ was measured. Also the magnetoresistance (MR) as a function of applied magnetic field, $MR(H)$ for all polycrystalline samples were measured at room temperature (295K) and liquid nitrogen temperature (77K). The MR behavior at room temperature for all samples show almost a linear field dependence of MR . The MR at 77K for all polycrystalline samples exhibit two distinct regimes as a function of magnetic field. Highly sensitive low field MR observe up to an applied magnetic field H^* . For $H < H^*$, the MR change rapidly with H followed by a gradual change as H is increase further. Beyond H^* , MR has a weak dependence in applied magnetic field.

Chapter 1

Introduction



Despite a long history of research going back to the 1950s [1], the recent discovery of colossal magnetoresistance (CMR) [2] in thin films of manganites has generated enormous excitement and great activity among the scientific communities. This is because it opens up the possibility of producing highly sensitive devices for a range of sensor and storage applications from crystal and thin films of manganites. This effect is usually obtained at low temperatures (below room temperature) and in a high magnetic field (several Tesla), but a practical application would require the operating conditions of both room temperature and a low magnetic field. Furthermore, with particular respect to technological applications of magneto electronic devices in microelectronic integrated circuits, epitaxial thin films would be highly desirable. Hence, the exploration of CMR material that is functional at room temperature and in a low magnetic field is very important [3]. Properly doped manganites behave as ferromagnetic metals at low temperatures and paramagnetic insulator at high temperatures. This generic behavior as well as CMR effect that occurs near the transition have been understood within the framework of double exchange [4,5,6] and superexchange [7] interactions mediated through the oxygen ions located between the Mn ions. In order to generalize super exchange a semi covalent exchange [8] has also been proposed. However, recently there has been an increasing realization that though these magnetic interactions are very important for understanding the behavior of manganites [9,10] are not adequate to explain the CMR behaviour of manganites.

Detailed studies [11] have shown that electron-phonon due to Jahn-teller effect is responsible for the observed properties in manganites and a more coherent picture has emerged [12] for the lattice polaron formation associated with the insulator-metal (M-I) transition in these materials. There is also a proposal [13] that M-I transition is a consequence of the large to small polaron transition induced by the reduction of effective hopping integrals at temperature near T_c . Moreover, it has become increasingly evident that the correlation between local structure changes and polaron formation can provide an adequate description for the anomalies observed in many

experiment, such as the unusual temperature dependence of Debye-Waller factors and lattice parameters [14,15], large frequency shifts of the internal infrared modes [16] and variations in the local structure as seen by pair distribution function (PDF) analysis [17]. In spite of above success there are indication that Jahn-Teller polaron formation does not take place in magnetic compound like $\text{La}_{2/3}\text{Sr}_{1/3}\text{MnO}_3$ so that an alternative disorder induced localization mechanism [18] for non-polaronic localization of charge carriers has been introduced. In addition, an empirical spin dependent hopping model [19] has also been suggested to describe the field dependent transport at constant temperatures. However, theoretical considerations are still not sufficient and more efficient physical models would have to be developed.

This thesis deals with the study of Magnetoresistance (MR) in manganite polycrystalline samples. Recently it was observed that for manganite, there is a huge decrease of resistance in presence of magnetic field. This phenomenon is called colossal magnetoresistance (CMR). For manganite, magnetoresistance (MR) is very high, it is about 99% for some samples in the presence of 10 T applied magnetic field. So manganite pose one of the most interesting and complex systems studied so far in the condensed matter physics. Here one has strong interactions between electrons that form quasi-localized moments, Ferro and antiferromagnetism, canted antiferromagnetism, metal-insulator transition, spin degree of freedom, charge and orbital ordering effects, strong electron-phonon coupling and spatial separation of these phase [20]. The coexistence and competition among these phases leads to physical complexity as a characteristic of their behavior. Thus manganites involve very rich physics with potential applications.

The initial work was done on the infinite layer cubic compounds, viz $\text{T}_{1-x}\text{D}_x\text{MnO}_3$ where T is a trivalent lanthanide cation (e.g. La) and D is divalent, e.g. alkaline-earth (e.g. Ca, Sr, Ba) cation. The parent compound LaMnO_3 is an antiferromagnetic insulator, which contains Mn^{3+} ions ($S=2$) with $t_{2g}^3 e_g^1$ configuration. As a result of substituting small amount of divalent cation (e.g., Ca, Sr, and Ba) for trivalent cation (La) in LaMnO_3 , the valence state of a few Mn will change from Mn^{3+} to Mn^{4+} and this is believed to be responsible for the occurrence of CMR transitions

[21]. This doped sample leads to a ferromagnetic metallic ground state. The ferromagnetic metallic state undergoes a metal-insulator transition to an insulating paramagnetic state at (or close to) the ferromagnetic transition temperature T_c . The doped sample shows a very large resistivity at T_c , which is reduced drastically by the application of magnetic field. This colossal magnetoresistance effect has been initially interpreted in terms double-exchange model in which carrier hopping between Mn^{3+} ($t_{2g}^3 e_g^1$) and Mn^{4+} (t_{2g}^3) depends on the relative alignment of ionic local magnetic moments [22].

1.1 Objectives

Many works on CMR materials thus far have been focused on $AMnO_3$ -type perovskite oxides that have simple three-dimensional structure. The tolerance factor, namely, lattice effects, has been known to be a crucial element in determining magneto transport properties in $AMnO_3$ oxides [23]. In view of the sensitivity of MR properties to the structure, our present study on $(La_{2-x}Nd_x)(Ba_{1-y}Ca_y)Mn_2O_7$ might provide an idea to elucidate fundamental understanding of the CMR property because it has a two-dimensionally layered structure. The structure of the above sample is considered as the $n=2$ member of the Ruddlesden-Popper series $A_{n+1}B_nO_{3n+1}$ in which two perovskite blocks composed by two-dimensional layers of BO_6 corner-sharing octahedra are separated by rock salt AO layers.

1.2 Summary of the thesis

In this thesis we shall describe the preparation, microstructure characterization and magnetoresistive properties of the samples $(La_{2-x}Nd_x)(Ba_{1-y}Ca_y)Mn_2O_7$.

The format of the thesis is as follows:

Chapter 2 gives the brief description of the basic issues of CMR in manganites. The phase diagrams of various divalent doped manganite, the various models of low-temperature, low-field MR are discussed.

Chapter 3 gives the details of the sample preparation and experimental techniques used in this research work.

Chapter 4 describes the results of polycrystalline $(La_{2-x}Nd_x)(Ba_{1-y}Ca_y)Mn_2O_7$

samples for various values of x and y .

Chapter 5 summarizes the findings of this dissertation.

References

- [1] G.H Jonker & J.H Van Santen, *Physica* **16**, 337 (1950)
- [2] R. von Helmolt, J. Wecker, B. Holzapfel, L. Schultz, and K. Samwer, *Phys. Rev. Lett.* **71**, 2331 (1993)
- [3] Jun Zhang, *J. Appl. Phys.* **90** (12), 6275 (2001)
- [4] C. Zener, *Phys. Rev.* **81**, 440 (1951)
- [5] P.G. de Gennes, *Phys. Rev.* **118**, 141 (1960)
- [6] P. W. Anderson, H. Hasegawa, *Phys. Rev.* **100**, 675 (1955)
- [7] J.B. Goodenough, *Prog. Solid State Chem*, **5**, 149 (1971)
- [8] J.B. Goodenough, *Phys. Rev.* **100**, 564 (1955)
- [9] A. J. Millis, P. B. Littlewood, and B. I. Shraiman, *Phys. Rev. Lett.* **74**, 5144(1995)
- [10] H. Röder, Jun Zang, and A. R. Bishop, *Phys. Rev. Lett.* **76**, 1356(1996)
- [11] A. J. Millis, Boris I. Shraiman, and R. Mueller, *Phys. Rev. Lett.* **77**, 175(1996)
- [12] Guo-meng Zhao, K. Conder, H. Keller, K. A. Müller, *Nature* **381**, 676(1996)
- [13] Chatchai Sritiwirawong and Michael Ziese, *App. Phys. Lett.* **73**(8), 1140 (1998)
- [14] P. G. Radaelli, D. E. Cox, M. Marezio, S.W. Cheong, P. E. Schiffer, and A. P. Ramirez, *Phys. Rev. Lett.* **75**, 4488(1995)
- [15] A. Radaelli. *Phy. Rev. Lett.* **B54**, 8992-5 (1996)
- [16] K. H. Kim, J. Y. Gu, H. S. Choi, G. W. Park, and T. W. Noh, *Phys. Rev. Lett.* **77**, 1877(1996)
- [17] A. Billinge, *Phy. Rev. Lett.* **77**, 515 (1996)
- [18] Y. Lyanda-Geller, S. H. Chun, M. B. Salamon, P. M. Goldbart, P. D. Han, Y. Tomioka, A. Asamitsu, and Y. Tokura, *Phys. Rev.* **B 63**, 184426 (2001)
- [19] P. H. Wagner, I. Gordon, L. Trappeniers, J. Vanacken, F. Herlach, V. V. Moshchalkov, and Y. Bruynseraede, *Phys. Rev. Lett.* **81**, 3980 (1998)
- [20] J.R. Schrieffer, The Evolution of Condensed Matter Physics (Foreword), National high magnetic field Lab and Physics Department, Florida State University, USA
- [21] R. von Helmolt, J. Wecker, B. Holzapfel, L. Schultz, and K. Samwer, *Phys. Rev. Lett.* **71**, 2331 (1993); Y. Tokura, A. Urushibara, Y. Moritomo, T. Arima, A. Asamitsu, G. Kido and N. Furukawa, *J. Phys. Soc. Jpn.* **63**, 3931 (1994).
- [22] C. Zener, *Phys. Rev.* **82**, 403 (1951); J. B. Goodenough, *ibid.* **100**, 564 (1955); P. W. Anderson and H. Hasegawa, **100**, 675 (1955).
- [23] H. Y. Hwang, S. W. Cheong, P. G. Radeli, M. Marezio, and B. Batlogg, *Phys. Rev. Lett.* **75**, 914 (1995); H. Y. Hwang, T. T. M. Palstra, S. W. Cheong, and B. Batlogg, *Phys. Rev.* **B 52**, 15 046 (1995), Y. U. Kwon, E. O. Chi, J. K. Kang, N. H. Hur, *J. Appl. Phys.* **82**, 3072 (1997).

Chapter 2

Literature Review

In this chapter various issues of colossal magnetoresistive materials were briefly described. Various phase diagrams are presented in this chapter. Theoretical explanations of colossal magnetoresistive materials are described. Various Models of low temperature magnetoresistance and grain boundary magnetoresistance are discussed.

2.1. Introduction

During the last decade, interest has grown in heterogeneous ferromagnetic materials, such as thin-film multilayers and cluster-alloy compounds which display so-called giant magnetoresistance (GMR). The interest in these systems stems from the prospect of their use in magnetic recording. Indeed, prototype disk drives employing GMR read heads present a challenge to traditional MR read-head technology [1]. More recently, it has become recognized that some materials, specifically 3d transition-metal oxides, possess large room-temperature magnetoresistivity associated with a paramagnetic ferromagnetic phase transition. The growth of interest in their properties stems in large part from the prospect of creating metal oxide devices whose performance exceeds GMR devices. In addition, it is now recognized that the large magnetoresistivity in these oxides is the result of a unique type of metal insulator transition, the understanding of which complements the drive for applications.

The compounds which have been the focus of the majority of studies are the manganite perovskites $T_{1-x}D_xMnO_3$ where T is a trivalent lanthanide cation (e.g. La, Y etc) and D is a divalent alkaline earth (e.g. Ca, Sr, Ba etc), cation. For the end members of the dilution series, $LaMnO_3$ and $CaMnO_3$, the ground state is antiferromagnetic (AF), as expected for spins interacting via the superexchange interaction when the metal– oxygen– metal bond angle is close to 180° [2]. In a certain range of doping, $x \approx 0.2-0.4$, the ground state is ferromagnetic (FM), and the

paramagnetic-to-ferromagnetic transition is accompanied by a sharp drop in resistivity $\rho(T)$. This phenomenon has been known to exist since 1950 [3, 4].

Recently, interest in these materials has been renewed by the realization that (i) the magnetoresistance (MR) associated with this correlation between magnetization (M) and resistivity (ρ) can be very large, and (ii) the basic interaction responsible for the ρ - M correlation, the double-exchange (DE) interaction [5-7] between heterovalent (Mn^{3+} , Mn^{4+}) neighbors, is by itself not sufficient to explain this MR [8]. Both the large resistance and the associated MR are now thought to be related to the formation of small lattice polarons in the paramagnetic state. The large MR resulting from the transition has been called colossal magnetoresistance [9], mainly to distinguish it as a phenomenon distinct from GMR. In addition to the renewed interest in the FM state, much attention has been given to another type of collective state, charge order (CO), typically observed for $x > 0.3$. At these doping levels CO can compete with the FM ground state, leading to complex electronic phase behaviour as chemical formula is varied [10-12]. Perhaps the biggest intellectual advance in understanding these disparate effects is the realization of the importance of electron-phonon (e-ph) coupling. Several theories have elucidated the role of e-ph coupling in producing CMR [13,14]. It is also widely held that this e-ph coupling is necessary to explain not only CMR, but also (i) the polaron signatures in transport studies, (ii) the large isotope effect on the FM Curie temperature [15], (iii) the large Debye-Waller factors [16] and (iv) the CO (charge ordering) state and its large sound velocity anomalies [12]. The microscopic origin of strong e-ph coupling is the large Jahn-Teller effect, which occurs for d^4 ions in an octahedral ligand environment [17]. For the undoped material ($x=0$) this results in a large static structural distortion [18]. The question of how this e-ph coupling manifests itself in the CMR range ($x \approx 0.2-0.4$) is one of the central questions to be addressed by theory.

2.2. Materials

2.2.1. Structure and electronic spectrum

Jonker and van Santen synthesized and characterized [3] a series of compounds with the general formula $T_{1-x}D_xMnO_3$ where T is a trivalent ion and D is a divalent ion. These compounds form in the structure of perovskite, $CaTiO_3$. In this

structure, the T, D and M ions from interpenetrating simple cubic sub lattices with O at the cube faces and edges, as shown schematically to the right in figure 2.1.

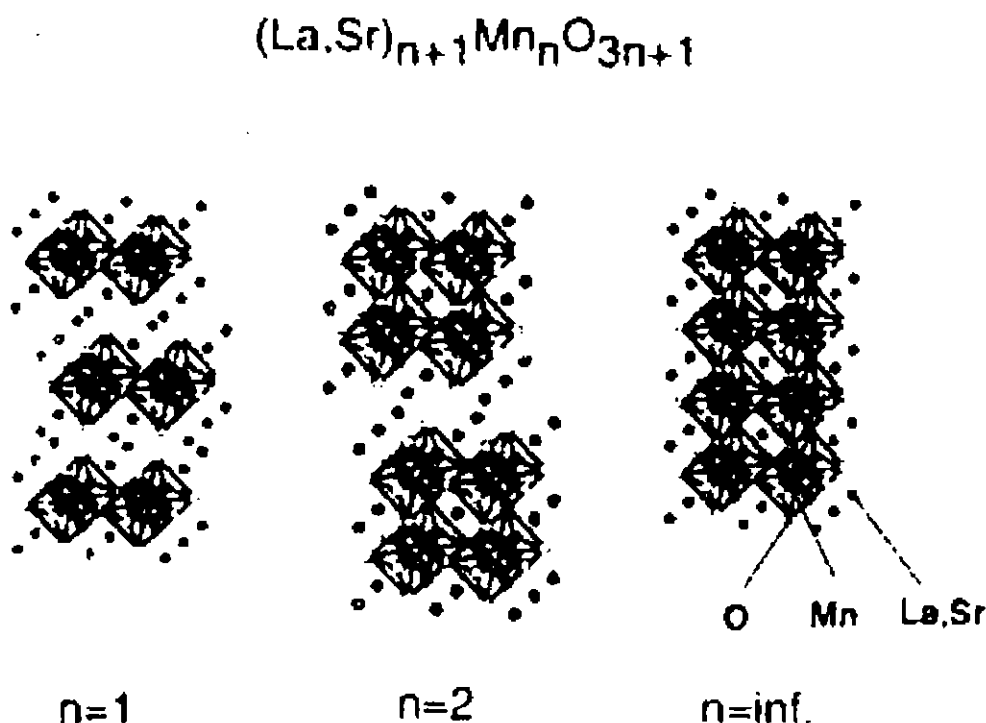


Figure 2. 1: Schematic structures of the Ruddlesden-Popper series of layered compounds. Here n is the number of connected layers of vertex-sharing MnO_6 octahedra. For $n=1$ the structure is that of K_2NiF_4 and $n=2$ is the bilayer structure and $n=\infty$ the distorted perovskite. The room-temperature lattice parameters are $a=b=3.86 \text{ \AA}$ and $c=12.48 \text{ \AA}$ for $n=1$ $a=b=3.87 \text{ \AA}$ and $c=20.14 \text{ \AA}$ for $n=2$, $a=5.45 \text{ \AA}$ for $n=\infty$ [26].

The crystal structure and lattice parameters obtained by neutron powder diffraction are given by Elemans *et al* for a series of solid solution $\text{La}_{1-x}\text{Ba}_x\text{Mn}_{1-y}\text{Ti}_y\text{O}_3$ [18]. All the compounds studied, which include the end member LaMnO_3 are isostructural, crystallizing in the orthorhombic $Pnma$ structure at room temperature. The end member LaMnO_3 is very distorted; the octahedra are elongated and tilted. Though tilting distortions are not unusual for perovskites simply on the basis of steric conditions, its magnitude in LaMnO_3 and the presence of elongation are thought to be the result of a Jahn-Teller local distortion [18,21]. Jirak *et al* has shown that for $\text{Pr}_{1-x}\text{Ca}_x\text{MnO}_3$, there exists a phase transition between a high-temperature pseudocubic phase and an orthorhombic phase [22]. This structural transition temperature exceeds 900 K for $x=0$ and decreases to room temperature at around $x=0.3$, the doping level

where the FM state appears, suggesting a strong magneto-elastic coupling. The structure of compounds exhibiting CMR is usually orthorhombic.

The early work of Jonker and van Santen established the range of possible solid solutions allowed by the Goldschmidt tolerance factor

$$t = (r_D + r_O) / \sqrt{2}(r_T + r_O) \approx 1,$$

where r_D , r_T and r_O are the radii of the divalent, trivalent, and oxygen ions, respectively [3]. The tolerance factor measures the deviation from perfect cubic structure ($t=1$). By using mixtures of $T = \text{La, Pr, and Nd}$ and $D = \text{Ca, Sr, Ba, and Pb}$, t can be varied, with the result that the perovskite structure is stable for $0.85 < t < 0.91$. At finite doping, charge balance is maintained by a fraction, x , of Mn ions assuming a tetravalent, $\text{Mn}^{4+} (d^3)$, configuration in a random fashion throughout the crystal, with the remainder in the $\text{Mn}^{3+} (d^4)$ state. Presumably, D substitution is equivalent to hole doping, but thermopower and Hall effect disagree on the carrier sign in the paramagnetic state, suggesting that a simple band picture is not valid. Mixed valence can also be modified by varying the oxygen content. For $x=0$ and 1, magnetization M ($T < 100\text{K}$) was found to be small, indicating an antiferromagnetic (AF) ground state.

At intermediate values of x , M rises and peaks with its Hund's-rule value at $x=0.3$. In subsequent work [4] van Santen and Jonker showed that at temperatures above the ferromagnetic Curie point, T_c , the resistivity behaves like a semiconductor, $d\rho/dT < 0$, but that below T_c , not only is there a sharp reduction in resistivity, but also a transition to metallic behaviour, $d\rho/dT > 0$. This behaviour is shown for $\text{La}_{1-x}\text{Sr}_x\text{MnO}_3$ and $\text{La}_{1-x}\text{Ca}_x\text{MnO}_3$ in Figures 2.2 and 2.3. Zener proposed a mechanism he called double exchange (DE) to explain the simultaneous occurrence of ferromagnetism and metallicity, both as a function of x and T found by Jonker and van Santen [5]. The FM state is observed only for finite D concentration where electronic transport is via holes arising from charge exchange between Ca^{2+} for example, and Mn. For $x < 0.5$ the majority of Mn ions are in the d^4 configuration which, for octahedral coordination, means a half-filled t_{2g} triplet and a quarter-filled e_g doublet. The minorities of sites are d^3 , which corresponds to a half-filled t_{2g} orbital triplet. Hund's rule dictates that as the hole hops from site to site, it is accompanied by a reduction in S from 2 to $3/2$ (Hund's energy $J_H \gg t$, the transfer

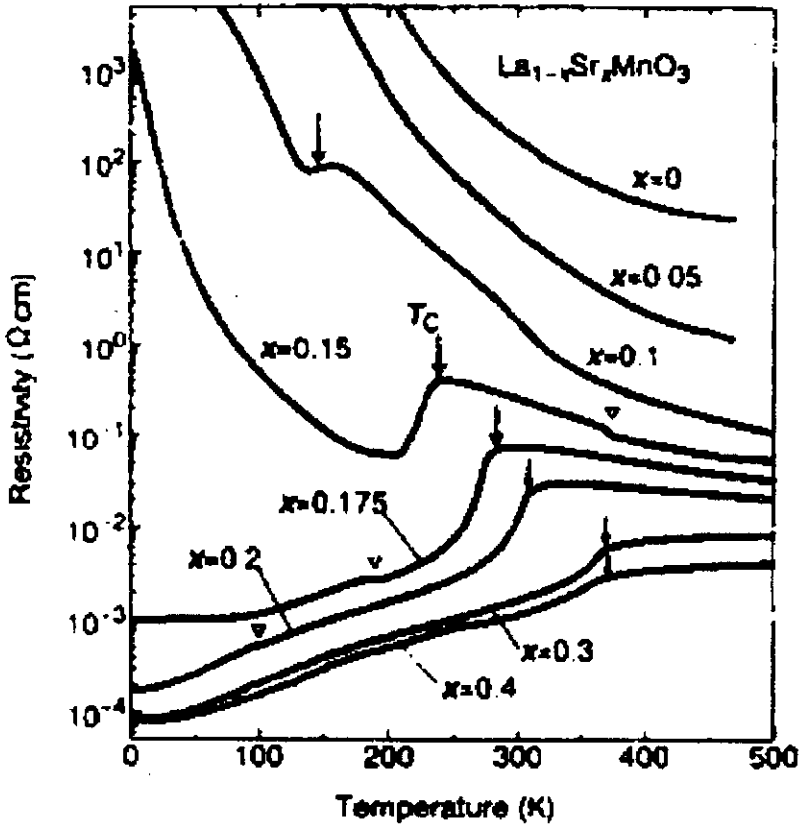


Figure 2.2: Resistivity against Temperature for $\text{La}_{1-x}\text{Sr}_x\text{MnO}_3$ for various x values. The arrows denote the transition as determined by magnetization measurement [27].

integral). This hopping is impeded if neighboring sites are orthogonal, i.e. spins not parallel. Anderson and Hasegawa showed that the transfer integral varies as the cosine of the angle between neighboring spins [6]. As temperature is lowered and spin fluctuations decrease, the combined itinerant local-moment system lowers its total energy by aligning the spins ferromagnetically and allowed the itinerant electrons to gain kinetic energy. Recently, Millis *et al* have shown that a Hamiltonian incorporating only the DE interaction cannot explain the most obvious feature of the manganites, namely the magnitude of the change in resistivity at the FM transition [8]. They, as well as Roder *et al*, proposed, in addition to DE, an electron-phonon coupling term [13,14]. Such an interaction is not unexpected in a picture

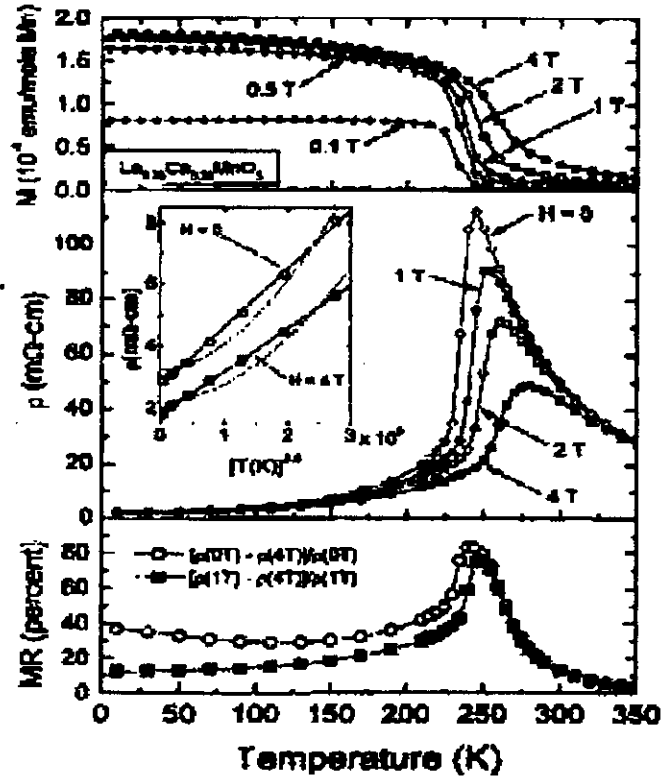


Figure 2.3: Top frame- magnetization against temperature for $\text{La}_{0.75}\text{Ca}_{0.25}\text{MnO}_3$ for varies field values. Middle frame resistivity against temperature The inset shows the low temperature resistivity compared to $T^{2.5}$ (solid line) and $T^{4.5}$ (dashed line) behaviour. Bottom frame- magnetoresistance against temperature. Open symbols reflect low-field behaviour and solid symbols reflect the high field behaviour [29].

where transition is via hopping among Mn^{3+} and Mn^{4+} ions. Here, the hole, corresponding to a $\text{Mn}^{4+}(\text{d}^3)$ ion must displace a $\text{Mn}^{3+}(\text{d}^4)$ ion, which, in the dilute limit, can be associated with a large Jahn-Teller (J-T) coupling. An analysis of acoustic resonance experiments for dilute Cr^{2+} in MgO shows that the O^{2-} ions are displaced by roughly 1.5 \AA from their undistorted position [17]. Here, Cr^{2+} is, like Mn^{3+} in LaMnO_3 , a d^4 ion in an octahedral oxygen environment. This distortion is of similar magnitude as that in LaMnO_3 and, most likely arises from that manifestation of the strong electron-phonon coupling implied by the J-T theorem in the dilute case. Even though the J-T theorem applies strictly only for single ions, the large distortion found in the acoustic resonance experiments suggests an e-ph coupling of a size which must also play a significant role for interacting ions. Using a different

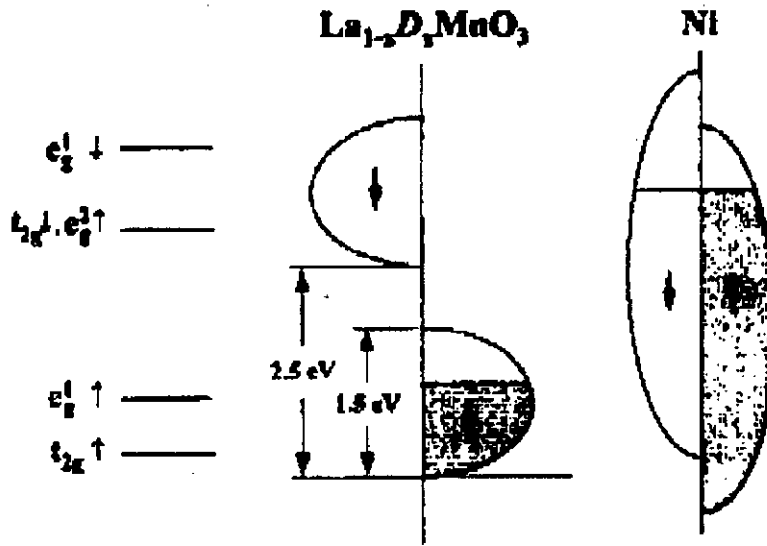


Figure 2.4: Schematic $T=0$ density of states for doped LaMnO_3 . The level diagram to the left shows the approximate positions of the 3d bands in undoped LaMnO_3 from [24]. The energy scale for $\text{La}_{2/3}\text{Sr}_{1/3}\text{MnO}_3$ is extracted from photoemission data [25]. Comparison is made to Ni metal which possesses a much smaller degree of spin polarization [60].

approach, Varma has attributed the main CMR effect to reduction of localization by spin fluctuation scattering with the application of a magnetic field [23].

The picture just outlined, of electronic hopping within narrow and fully spin-polarized bands is supported by a band structure calculation made for the end members of one dilution series, LaMnO_3 and CaMnO_3 [24]. For LaMnO_3 this calculation shows a typical separation between up and down polarized bands of about 1.5 eV and bandwidths of order 1-1.5 eV. Photoemission experiments on $\text{La}_{1-x}\text{D}_x\text{MnO}_3$ ($D = \text{Ca, Pb}$) confirm these basic features [25]. The density of states for such a system is shown schematically in Figure 2.4. Also shown for comparison is the density of states for Ni metal. Since the up and down spin bands are well separated, the magnetic polarization (saturation moment) is 100%, compared to 11% in Ni. This will lead to reversal of carrier spin direction across FM domains.

2.2.2 Layered compounds

The perovskite structure is one in a Ruddlesden-Popper series $(T_{1-x}D_x)_{n+1}Mn_nO_{3n+1}$ of layered compounds. Here, n indexes the number of connected layers of vertex sharing MnO_6 octahedra. The endpoints in this series have $n=1$ and ∞ which correspond to the single-layered K_2NiF_4 structure $La_{1-x}Sr_{1+x}MnO_4$ has been well studied [30, 31]. These compounds exhibits insulating behaviour for all x , and in the region $x \approx 0.5$, a CO state appears below about $T=250$ K [30-32]. At lower temperature ($T \approx 20$ K), a spin-glass state appears for $0.2 < x < 0.6$. Spin-glass behaviour common among manganites with low T_c and presumably reflects the competition between the DE FM interaction and AF superexchange of the present compound $LaMnO_3$. The $x < 0.1$ compounds are AF below $T \approx 100$ K. For $n=2$, one has the so-called double-layer system. In these compounds large MR has also been observed for $La_{2-2x}Sr_{1+2x}Mn_2O_7$ and $La_{2-2x}Ca_{1+2x}Mn_2O_7$ [33] (with this notation, x serves the same role as in the perovskites, denoting the nominal hole concentration). For Ca ($x = 0.25$) a FM T_c of 215 K was identified but the MR peak occurs at a much lower temperature ~ 100 K. The discrepancy between these two temperatures was ascribed by the authors to the quasi- 2D nature of the Mn-O layers. For Sr substitution, there are two transitions for $x = 0.4$, one at $T \approx 300$ K which can be attributed to 2D short-range order and a FM transition at $T=126$ K, below which both c-axis and ab-plane resistivity change from semiconducting ($d\rho/dT < 0$) to metallic ($d\rho/dT > 0$). The MR for this compound is much larger than for the 3D ($n=\infty$) system which illustrates the general trend of increasing MR with decreasing T_c . At a slightly lower concentration $x=0.3$, the $n=2$ system exhibits striking anisotropy in its transport properties; $d\rho_{ab}/dT > 0$ between the FM T_c and the 2D SRO T_c while $d\rho_c/dT < 0$ in the same temperature region (figure 2.9) [34]. That is not only does the magnitude of $\rho(T)$ differ between the two principal crystallographic directions, but the form of the temperature dependence also differs. This decoupling of in-plane and out-of-plane transport behaviour is reminiscent of the highly anisotropic superconductors Sr_2RuO_4 and high- T_c cuprites. At low temperatures, large low-field MR is interpreted as interlayer tunneling. The effect of different lanthanide-ion substitution has also been

studied for the double layer system for $\text{LnSr}_2\text{Mn}_2\text{O}_7$ [35, 36] which for $\text{Ln}=\text{Tb}$ exhibits a low-temperature magnetization much reduced from that of $\text{Ln} = \text{La}$; for Ln

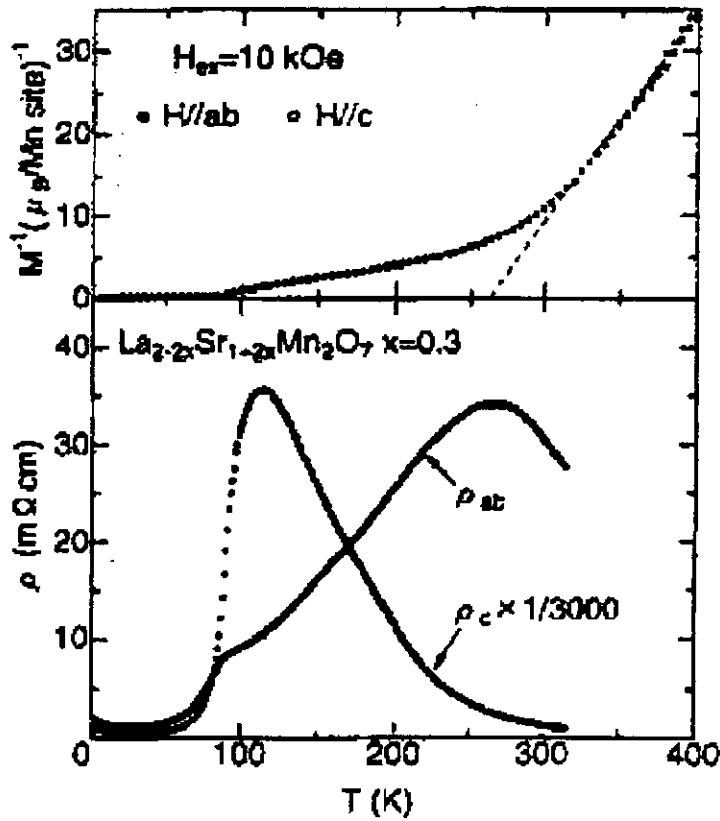


Figure 2.5: Top temperature dependence of the inverse magnetization at $H=1\text{T}$. Bottom: in-plane and inter plane resistivity at zero field for the bilayer material $\text{La}_{2-2x}\text{Sr}_{1+2x}\text{Mn}_2\text{O}_7$ ($x=0.3$) single crystal [34].

$= \text{Nd}$, the magnetization is also much smaller than for $\text{Ln} = \text{La}$, and hysteresis reminiscent of spin-glass ordering is seen near 150K [37, 38]. A structural study for $0.5 \geq x \geq 0.75$ with $\text{Ln} = \text{La, Pr, Nd, Sm, Eu, Gd, Tb, Dy, Ho, Y}$ and Er showed the existence of cation ordering between the two available cation sites with the smaller lanthanides preferring the site in between the double-layer block [39].

2.3 Properties of CMR Materials

2.3.1 Intrinsic Properties

In magnetism, it is customary to distinguish intrinsic properties, which depends only on the bulk chemical composition and crystal structure, from extrinsic properties which are govern by sample size and microstructure. For example hysteresis is generally an extrinsic property on the other hand spontaneous magnetization is an intrinsic property. Intrinsic properties are best measured on single crystal and epitaxial film.

2.3.2 The paramagnetic phase

The paramagnetic insulating phase shows thermally activated conduction. The transport mechanism above T_c is still a matter of controversy as number of groups have reported different behavior. Data on compound with $x \approx 0.3$ were first fitted to

$$\rho = \rho_0 \exp(E_0/k_B T) \quad (2.1)$$

where E_0 is the activation energy, K_B is the Boltzman constant. It is also suggested that Mott's variable range hopping (VRH) expression is given by

$$\rho = \rho_0 \exp(T_0/T)^\nu \quad (2.2)$$

with $\nu = 1/4 - 1/2$ is appropriate. There is also evidence for a

$$\rho \propto T \exp(E_0/kT) \quad (2.3)$$

behaviour over an extended temperature range.

Intrinsic variation in the Coulomb potential due to the presence of A^{3+} and A^{2+} ions in a lattice, together with the presence of magnetic disorder above T_c will lead to the formation of a mobility edge [40] E_μ giving an activated conductivity. Band transport, where E_0 is interpreted as a real gap in the density of states implausible, because it is difficult to justify a gap over a range of Mn^{4+} concentrations from $x=0.2$ to 0.4 in the absence of any change in structure. But there is also a problem with interpreting E_0 as $E_\mu - E_F$. The Hall resistivity in manganites is very small and difficult to measure, but seems that the mobility is no more than $10^{-5} m^2 v^{-1} s^{-1}$, which corresponds to a mean free path less than 0.1nm. This is consistent with band transport [41]. Figure 2.6 shows data on a series of manganites with $x=0.3$, which have different resistivity and transition temperature [42, 43]. Assuming $\nu=1/4$ in (eq. 2.2)

the VRH parameter T_0 is shown for a wide range of substituted manganites with $x=0.3$. The samples were as deposited films or bulk ceramics.

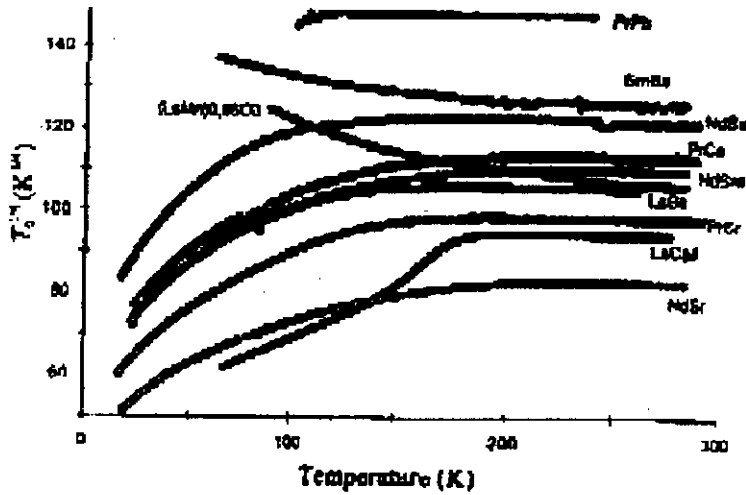


Figure 2.6: Plot of parameter T_0 variable-range hopping model for $(R_{0.7}A_{0.3})MnO_3$ compounds with different R and A combinations.

Originally, the VRH theory [44] was developed to explain electron transport in doped semiconductors, where electrons occupying hydrogenic orbitals with the wave functions $\psi = \psi_0 \exp(-\alpha r)$ are localized by potential fluctuations associated with the dopant. Here $1/\alpha$ is the localization length. There is a competition between the potential energy difference and the difference electron can hop. This is reflected in the expression of the hopping rate $\gamma = \gamma_0 \exp(-2\alpha R - \Delta E/kT)$ to a site at a distance R , where the energy of the carrier is ΔE higher than at the origin. Here γ_0 is a constant. Because of the exponential, the hopping rate will be dominated by the maximum value of the bracket. A sphere of radius R contains $(4/3)\pi R^3/v$ site, where v is the lattice volume per manganese ion $5.7 \times 10^{-29} \text{ m}^3$. The smallest value of ΔE is therefore $[4/3 \pi R^3 N(E)]^{1/2}$, where $N(E)$ is the density of the states. Maximizing the bracket, we find $R = [9/8 \pi \alpha N(E) kT]^{1/4}$, hence the expression for resistivity ($\rho \approx 1/\gamma$) is

$$\rho = \rho_0 \exp(1.9[\alpha^3/N(E)kT]^{1/4}) \quad (2.4)$$

which is the Mott expression with

$$kT_0 = 18\alpha^3/N(E) \quad (2.5)$$

Other derivations yield different prefactors. Electron hopping is always of variable range- type at low temperature where the thermal energy is not great enough to allow

electrons to hop to their nearest neighbors. In that case it is more favorable for the electrons to hop further to find a site with a smaller potential difference. At higher temperatures nearest neighbor hopping ($\ln\rho\sim T^{-1}$) can contribute significantly to the transport.

To apply the model to the data in Figure 2.6, we take electronic density of states $N(E)$ from low-temperature heat capacity measurements [45] as $4\times 10^{28} \text{ m}^{-3} \text{ eV}^{-1}$. Values of kT_0 range from 220 eV for $(\text{La}_{0.7}\text{Sr}_{0.3})\text{MnO}_3$ to 43600 eV for $(\text{Pr}_{0.7}\text{Pb}_{0.3})\text{MnO}_3$; the corresponding localization length l/α deduced from equation 2.5 are 0.18 nm and 0.03 nm, respectively. The values of the average hopping distance at room temperature are 0.67 nm and 0.43 nm, respectively. Since the Mn-Mn distance is 0.38 nm, these numbers are incompatible with variable-range hopping associated with Anderson localization; the localization length due to random localization fluctuations must exceed the interatomic distance, and the hopping distance has to be several times greater. The discrepancy is too great to be explained by any plausible change in the density of states at T_c . It is likely that the carriers in manganites form dielectric polarons. There is some direct evidence of this in the distribution of Mn-O bond lengths contained in a pair distribution function of $(\text{La}_{1-x}\text{Ca}_x)\text{MnO}_3$ with $x=0.12$ [46]. The hopping motion of polarons leads to the resistivity of the form of (eq. 2.3) with constant proportionality (k/ne^2D), where n is the carrier density and D is the polaron diffusion constant. There may be contributions to the hopping energy E_0 of magnetic elastic or Coulombic region [47]. Thermo power data also support polaron hopping in the paramagnetic state.

The nearest-neighbor hopping process with high activation energy may transform into uncorrelated variable range hopping ($\ln\rho\sim T^{1/4}$) when the available phonon energy is so small as to make the longer-range hop necessary to find a site sufficiently close in energy for hopping to occur. This is not incompatible with small polarons also leading to $\ln\rho\sim T^{1/4}$ [48]. For highly correlated electron systems, a small gap appears at E_F and the hopping law is then $\ln\rho\sim T^{1/4}$ at temperatures below the correlation gap [49].

A key question regarding the manganites concerns the relative importance of the magnetic and Coulomb random potentials in establishing the mobility edge.

Manganites with $x=0.3$ show little structural change at T_c , so that any change in band structure and density of states should be associated with the onset of ferromagnetic order. Virect et al. [42, 43] have suggested that a random potential of mainly magnetic origin is responsible for carrier localization above T_c . This potential is due to Hund rule coupling $-J_{Hs}$ between localized Mn t_{2g} ions cores ($S=3/2$) and the spins S of the e_g electrons in the conduction band. They write this energy in the form of $E_m = J_H(1 - \cos\theta_{ik})$, where θ_{ik} is the angle between the spins of two well separated Mn ions cores between which the e_g electron is hopping and $2J_H$ is the splitting of the ions cores uncorrelated in the paramagnetic state, the probability of finding an angle θ_{ik} between the two ion cores $P(\theta_{ik}) = 1/2 \sin\theta_{ik}$. The probability of a barrier E is therefore

$$P(E_m) = P(\theta) \frac{d\theta_{ik}}{dE_m} = \frac{1}{2U_m} \quad 2.6$$

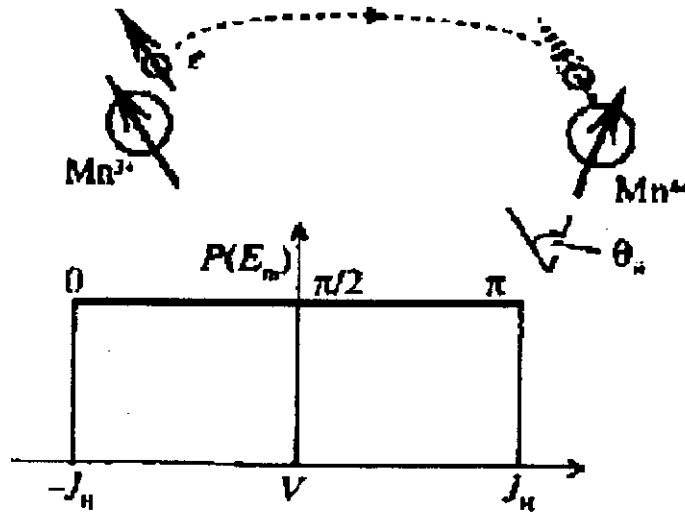


Figure 2.7: Variable-range electron hopping with spin memory, showing the random potential distribution of magnetic origin in the paramagnetic state. $P(E_m)$ is the probability of a hopping electron encountering an energy barrier E ; J_H is the on-site Hund rule interaction for Mn^{3+} [50].

Such a magnetic random potential is significant here because J_H is close to 1 eV. In estimating the density of states to include in equation (2.5), the probability of equation (2.6) must be multiplied by the number of available states per m^3 . Hence,

$$N(E_m) = P(E_m)(1-x)fg/v \quad (2.7)$$

where $(1-x) = 0.3$ is the probability that the e_g orbital at the manganese site receiving the hopping electron is unoccupied, f is the geometric factor of order 0.5 which accounts for the fact the hopping electron has a d_{z^2} rather than an S -state wave function, and g is the probability than an unoccupied manganese orbital can actually accept an electron.

2.4 Transport properties

2.4.1 High-temperature transport in perovskites-evidence for polarons

A discussion of the phenomenology of electronic transport in the manganite perovskites can be conveniently separated into three regimes, high-temperature, low-temperature, and critical region. Critical behaviour is best described by thermodynamic measurements, which couple directly to the magnetic correlation length. There does not yet exist a full complement of data to address the critical behaviour. We therefore restrict the discussion to behaviour at low and high temperatures.

2.4.2 High-temperature resistivity, thermopower

At high temperature, $T > T_c$, in the concentration region where *CMR* is strongest, $0.2 < x < 0.4$, transport is characterized by an activated resistivity $\rho(T) \propto \exp(\Delta_p/T)$ [3] where $\Delta_p \approx 1000-2000$ K (other reported values are $1100+60$ K for $\text{Nd}_{0.5}\text{Pb}_{0.5}\text{MnO}_3$, 1300 K on $\text{La}_{0.67}\text{Ca}_{0.33}\text{MnO}_3$ thin film [51], $2500-1000$ K for $\text{La}_{1-x}\text{Ca}_x\text{MnO}_3$ ($0.1 < x < 0.6$) [52], depending on x). The thermopower, $S(T)$, also behaves as expected for a semiconductor, $S(T) \propto \Delta_S/T$, where $\Delta_S \approx 120$ K [51], $500-20$ K [52-58] (Figure 2.8). In the simplest of models, namely that of an intrinsic semiconductor with a single carrier type, $\Delta_p = \Delta_S$. The experimental work indicates an order-of-magnitude discrepancy between Δ_p and Δ_S , which strongly suggests an additional excitation. It has been suggested, based on the size of the lattice distortion associated with the Jahn-Teller effect for d^4 ions with octahedral coordination, that charge conduction is via small polarons. In the extreme case of noninteracting polarons, there is no entropy transport accompanying charge transport since the polaron energy term in the chemical potential cancels the polaron energy term in the high-temperature expansion

of the Kubo formula [59]. In the presence of polaron-polaron interactions however this cancellation does not occur and an extra contribution, of the order of the interaction strength, appears.

Thus in this scenario, Δ_p measures the polaron binding energy while Δ_S measures the polaron-polaron interaction energy. Additional terms will include a spin entropy term, $S_s = (k_B/e)\ln(4/5) \approx 20 \mu\text{VK}^{-1}$ and a configuration (Heikes) entropy term, $S_C = (k_B/e)\ln(1-c_h)/c_h$, where c_h is the fractional hole concentration. It is observed that at high temperatures, $S(T)$ extrapolates to a value consistent with S , independent of x , presenting a puzzle which is perhaps related to the difference between Δ_p and Δ_S . The thermopower of $\text{La}_{0.67}\text{Ca}_{0.33}\text{MnO}_3$ films in an applied field undergoes the behaviour expected from the known T_c shift and in the critical region displays decreases greater than a factor of 10 for H up to $8T$. An alternative, chemistry-based, interpretation of

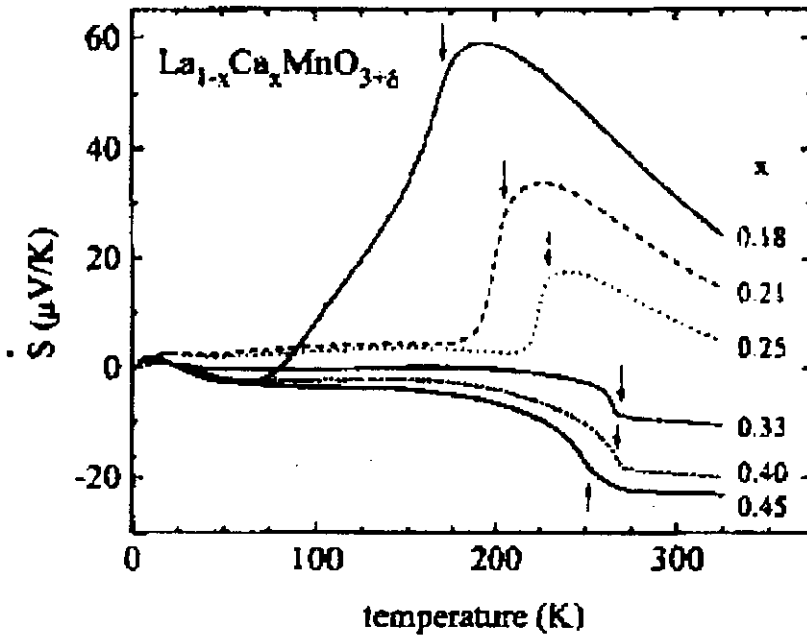


Figure 2.8 : The Seebeck coefficient for $\text{La}_{1-x}\text{Ca}_x\text{MnO}_3$ with varying Ca^{2+} concentration. The arrows indicate the magnetic ordering temperature. (Reproduced from [58])

thermopower which seeks to explain the anomalous x -independence at high temperatures is offered by Hundley and Neumeier [58]. The implication that the configurational term, S_C , is nearly x independent is contrary to the expectation that substitution of one Ca ion leads to one mobile hole. They point out that usually

$Mn^{3+}(3d^4)$ is less stable than its neighbours, $Mn^{2+}(3d^5)$ and $Mn^{4+}(3d^3)$, and this can lead to disproportionation of Mn^{3+} - Mn^{3+} pairs into Mn^{2+} - Mn^{4+} pairs, a phenomenon not uncommon in transition metal oxides. If one then postulates that only one of the several different Mn valence species is conducive to polaron hopping, then as x is varied, not only is the number of carriers varied, but also the number of possible sites for transport. The configurational contribution, S_c , would therefore depend on the disproportionation probability of Mn^{3+} and after correcting for this using existing thermal-gravimetric (TGA) data, good agreement is found with the Heikes formula. This provides an important alternative view of conduction in the manganites.

2.4.3 Low-temperature transport-low-field magnetoresistance

The low-temperature transport can be divided into two distinct phenomena, the behaviour of the intrinsic, metallic or semiconducting state, which characterizes high-field MR, and that of the intergrain process which characterizes the low-field behaviour.

2.4.4 Low-temperature resistivity intergrain transport, noise

Ju *et al* noticed large low-field magnetoresistance ($MR_{0.3}=25\%$) in ceramic samples of $La_{0.67}Ba_{0.33}MnO_z$ ($z = 2.99-2.90$) and ascribed this to transport across magnetic domain boundaries. Schiffer *et al* observed the same effect in ceramic $La_{0.75}Ca_{0.25}MnO_3$, ($MR_{0.2}=45\%$ at 0.2T) [29]. In this experiment, however, the size of the residual resistivity, $\rho_0=10^{-3}\Omega$ cm implied a mean free path of $\sim 10\text{\AA}$, much smaller than a typical domain size, leading the authors to suggest an additional source of scattering in the grain boundaries. Hwang *et al* demonstrated that this effect was in fact due to scattering by grain boundaries by comparing the low-field MR of polycrystalline $La_{0.67}Sr_{0.33}MnO_3$ and single crystals of the same composition, for which the low-field effect is absent [60] (Figure 2.9). They showed that the magnitude of the initial drop in $\rho(H)$ varies with temperature as $[(a+b)/(T+c)]$ which is, characteristic of spin-polarized tunneling in granular ferromagnets [28,61] Gupta *et al* correlated the low-field MR in films of $La_{0.67}D_{0.33}MnO_{3-\delta}$ ($D=Ca, Sr$ or vacancies)

with grain size as measured using transmission electron microscopy (TEM) [62]. They observed no low field MR for epitaxial films and a $MR_{0.5}=25\%$ at 25K for films with 3 μm grain size. Trilayer devices with junction structure, $\text{La}_{0.67}\text{Sr}_{0.33}\text{MnO}_3/\text{SrTiO}_3/\text{La}_{0.67}\text{Sr}_{0.33}\text{MnO}_3$ show $R_{0.01}\approx 83\%$ at 4.2K[63]. Tunneling has been directly observed in these devices as a nonlinear I-V characteristic [64]. Mathur *et al* has fabricated a device that probes the effect of transport across a single grain boundary [65]. They use a bicrystal SrTiO_3 substrate on which is grown a 200nm epitaxial (002) $\text{La}_{0.7}\text{Ca}_{0.3}\text{MnO}_3$ film. A meander line is then patterned from the film across the grain boundary formed at the bicrystal junction. The section of material spanning the grain boundary is one arm of an in situ Whetstone bridge to further isolate the behaviour of the defect. A peak in the effective resistance of the defect is seen just below T_c and associated with this is an effective $MR_{0.18}$, which decreases to zero at T_c in a nearly linear fashion. This magnitude of the low-field MR at temperatures close to 300K is larger than that reported by Hwang *et al* [60] in polycrystalline material and demonstrates the feasibility of room-temperature devices made from CMR material. Finally Hwang *et al* have achieved large MR at low field using a heterostructure made of $\text{La}_{0.67}\text{Ca}_{0.33}\text{MnO}_3$ sandwiched between two pole pieces of a soft ferromagnet $(\text{Mn}, \text{Zn})\text{Fe}_2\text{O}_4$ [66]. Here the applied field is enhanced by the internal field of the pole pieces so the demagnetization field is expected to play an important role in application of this concept to devices. Central to any discussion of usefulness of CMR materials is whether the MR signal is large compared to the intrinsic noise. Issues of concern are both the high $\rho(T_c)$ values and the $1/f$ noise related to magnetic domain fluctuations. Alers *et al* have addressed these issues with noise measurements in $\text{La}_{0.67}\text{Y}_{0.07}\text{Ca}_{0.33}\text{MnO}_3$ thin films [67]. These films had a $MR_6 > 10^3$ at $T_c=180\text{K}$. The noise was typically $1/f$ in character and when averaged over the frequency band $1=25$ Hz, had a broad maximum as a function of temperature, peaking below T_c . Due to the $1/f$ character, low-frequency applications near T_c are constrained the equivalent magnetic field noise for a volume of 10^{-12} cm is roughly 10^3 Oe Hz^{-1} . However, at high frequencies, e.g 10 MHz, the signal to noise ratio for a Oe signal is roughly 20dB. Thus, while domain-related noise might inhibit incorporation of CMR material for low frequency applications such as magnetic storage, these problems are reduced significantly for applications such as reading.

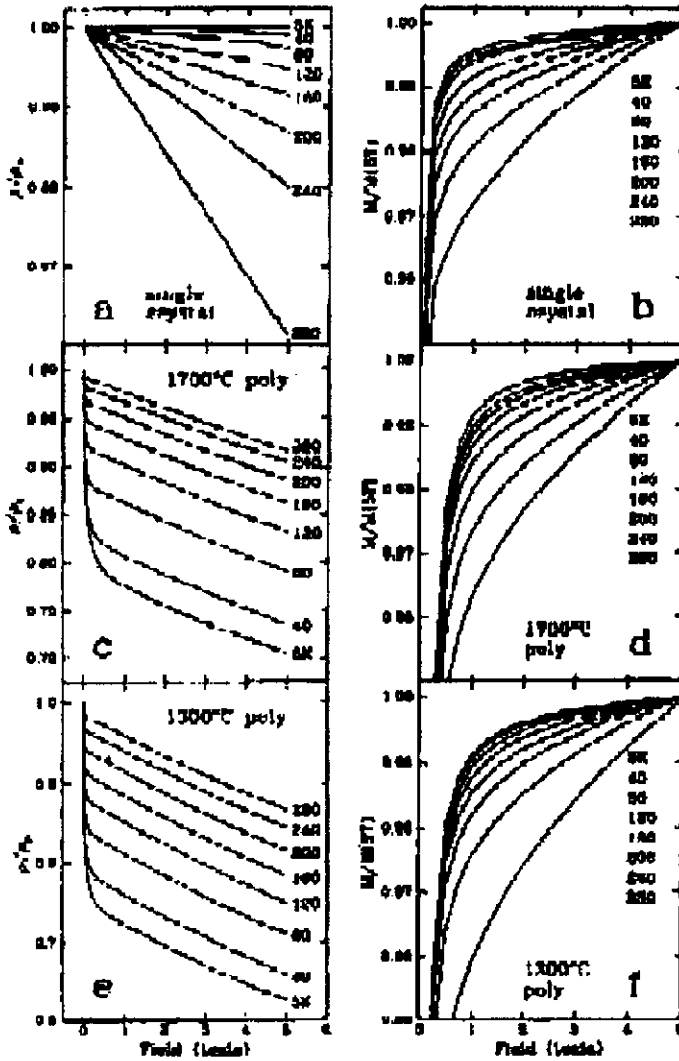


Figure 2.9: Panels a, c and e: The magnetic field dependence of the normalized resistance at various temperatures from 5 to 280 K. Panels b, d and f: The magnetic field dependence of the magnetization (normalized to the 5 T value) at various temperatures from 5 to 280 K. (From Hwang et al. [60])

2.4.5 Low-temperature resistivity-intrinsic

The inherent cation disorder in the solid solution manganites can lead to electronic scattering which results in large values of $\rho_0 = \rho(T=0)$. Nevertheless, several groups have addressed the intrinsic scattering mechanisms. Of relevance here is the prediction of $\rho(T) \propto T^{4.5}$ for electron-magnon scattering in a double -exchange system [68]. Schiffer *et al* found in $\text{La}_{1+x}\text{Ca}_x\text{MnO}_3$ for $x=0.23, 0.33, 0.45$, that the resistivity for $T < 0.5T_c$ is well fitted by the expression $\rho(T) = \rho_0 + \rho_1 T^p$, where $p = 2.5$, whereas $p =$

4.5 provides a poor fit [29]. However the data can be fitted by the above expression using $\rho = 4.5$ and an additional T^2 term representing electron-electron scattering. A similar conclusion was reached by Snyder *et al* based on measurements of $\rho(T)$ in high-quality films of $\text{La}_{0.67}\text{D}_{0.33}\text{MnO}_3$ (D= Ca, Sr) where ρ_0 values as small as $100\Omega\text{cm}$ were achieved [69]. Urushibara *et al* plot $\rho(T)-\rho_0$ versus T^2 for $T < 200\text{K}$ for $\text{La}_{1-x}\text{Sr}_x\text{MnO}_3$ ($x=0.3, 0.4$) crystals possessing $\rho_0 < 100\mu\Omega\text{cm}$ [33]. They find upward curvature on such a plot, consistent with Schiffer *et al*. These characteristic temperature dependences should not be automatically assumed to indicate only electron-electron and electron-magnon scattering since at the temperatures over which the fits are made (10-150K), electron-phonon scattering can be significant since $\theta_D \approx 400\text{-}500\text{K}$. Finally, small ρ_0 values with intrinsic $\rho(T)$ behaviour are also seen in single crystals of $\text{Pr}_{0.5}\text{Sr}_{0.5}\text{MnO}_3$ which on cooling in zero field exhibit semiconducting like $d\rho/dT < 0$ [10]. On application of fields of order 7T, $\rho(T)$ is converted to that of a metal, $d\rho/dT > 0$ and ρ_0 can be as low as $150\mu\Omega\text{cm}$. The studies which concentrate on the intrinsic $\rho(T)$ behaviour at low temperatures support the view that there are several contributions and that further work is needed; especially at temperatures below 1K in grain-boundary-free material, to determine the relative strengths of different scattering mechanisms.

2.5 Theory of Manganites Systems

2.5.1 Double Exchange Model

The itinerant charge carriers (holes) in the substituted $\text{La}_{1-x}\text{A}_x\text{MnO}_3$ (A is a divalent cation) provide the mechanism of ferromagnetic interaction between Mn^{3+} and Mn^{4+} ions. The addition of divalent material in undoped LaMnO_3 changes the valence state of some Mn^{3+} to Mn^{4+} . The Mn^{3+} ions in LaMnO_3 have three electrons in the t_{2g} state and one electron in the e_g state due to the crystal field splitting. Because of the strong Hund coupling and on-site Coulomb repulsion between e_g electrons, LaMnO_3 is an antiferromagnetic insulator. When trivalent La^{3+} ions are replaced with any divalent cations (e.g., Ca, Sr, Ba etc.), some Mn ions change to the Mn^{4+} state without e_g electrons. The vacant e_g state of Mn^{4+} makes it possible for e_g electrons in

surrounding Mn^{3+} ions to hop into the e_g state of Mn^{4+} as long as the localized t_{2g} spins of neighbouring Mn^{3+} and Mn^{4+} ions are parallel.

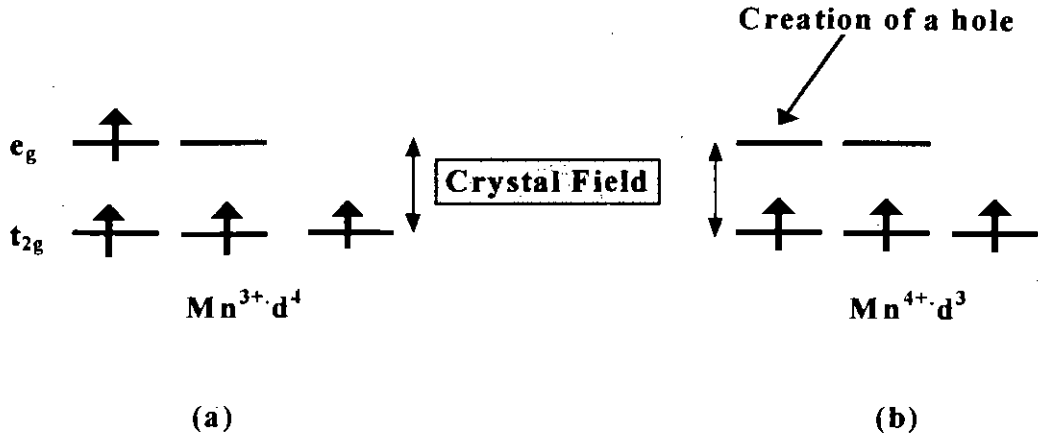
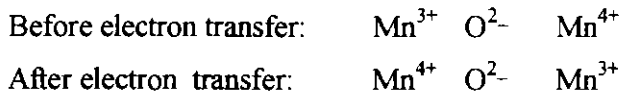


Figure 2.10 : The splitting of the t_{2g} and e_g band in $La_{1-x}A_xMnO_3$.

In the perovskite structure the Mn ions are separated by O^{2-} ions and the conduction process occurs via oxygen as follows:



Jonker and van Santen [3], and Wollan and Koehler [70], concluded that the exchange coupling in general is (a) ferromagnetic between Mn^{3+} and Mn^{4+} ions (b) antiferromagnetic between Mn^{4+} ions (c) either ferromagnetic or antiferromagnetic between Mn^{3+} .

The T_c is related to the strength of the transfer integral between Mn^{3+} and Mn^{4+} ions. It can be expected that this coupling is strongly dependent on the angle subtended by the $Mn^{3+}-O-Mn^{4+}$ bond [71]. It is found that the T_c is reduced by bending the $Mn^{3+}-O-Mn^{4+}$ bond [72-75]. Although the ferromagnetism in these materials is attributed to the double exchange mechanism mediated by $Mn^{3+}-O-Mn^{4+}$, the origin of $M-I$ transition in these materials remains a subject of considerable debate. Millis et al. [76-78], have argued that the double exchange mechanism alone is not sufficient to account for a disorder driven $M-I$ transition in this system and conclude that lattice distortion plays a necessary and crucial role in the $M-I$ transitions and the resulting CMR effect. In spite of the intensive research effort, which is currently ongoing, the coupling between crystallographic structure and the electrical

and magnetic properties is not completely understood and control of the CMR in this system is still challenging.

2.5.2 Orbital Ordering from Superexchange

LaMnO₃ materials finds all the manganese ions as Mn³⁺ and hence each atom has a singly occupied e_g orbital. The experimental conclusion is that a typical antiferromagnet is stabilized, with ferromagnetic planes alternating in orientation as we move parallel to the z -axis. The standard explanation is that the occupied d -orbitals couple ferromagnetically and reside in the x - y plane, while essentially 'empty' orbital couple antiferromagnetically by superexchange up to z -axis.

The model previously developed is

$$H = \frac{t^2}{U} \sum_{\alpha} \sum_{\langle j' \rangle_{\alpha}} [s_j^{\alpha} s_{j'}^{\alpha} - \frac{1}{4}]. \quad (2.8)$$

in terms of bonding components of the pseudo-spins:

$$s_j^{\alpha} = s_j^x \cos \phi_{\alpha} + s_j^y \sin \phi_{\alpha}. \quad (2.9)$$

There appears little point in orienting pseudo-spins out of the x - y plane, and so we make the assumption that each classical spin may be described by an angle ϕ_i . The classical energy then becomes

$$H_0 = \frac{t^2}{U} \sum_{\alpha} \sum_{\langle j' \rangle_{\alpha}} \left[\cos(\phi_j - \phi_{\alpha}) \cos(\phi_{j'} - \phi_{\alpha}) - \frac{1}{4} \right]. \quad (2.10)$$

The problem is solvable using the periodicity with

$$e^{i\phi_j} = \sum_{\vec{k}} e^{i\vec{k} \cdot \vec{R}_j} S_{\vec{k}} \quad (2.11)$$

in terms of couples numbers $S_{\vec{k}}$. Only particular combinations appear in the Hamiltonian, which reduces to

$$H_0 = N \frac{t^2}{4U} \sum_{\vec{k}\alpha} [\gamma_{\vec{k}\alpha} - \gamma_{0\alpha}]^2 \quad (2.12)$$

in terms of the combinations

$$T_{\vec{k}\alpha} = e^{-i\phi_\alpha} s_{\vec{k}} + e^{i\phi_\alpha} s_{-\vec{k}}^* \quad (2.13)$$

and the structure factors,

$$\gamma_{\vec{k}\alpha} = \frac{1}{N} \sum_{\langle jj'\rangle\alpha} e^{i\vec{k}(\vec{R}_j - \vec{R}_{j'})} \quad (2.14)$$

where N is the number of atoms involved. The fact that the ϕ_j are phases is then controlled by the constraints.

$$\sum_{\vec{k}\alpha} T_{\vec{k}+\vec{q}\alpha}^* T_{\vec{k}\alpha} = 2N^b \sum_G \delta_{\vec{q},G} \quad (2.15)$$

where N^b is the number band orientation and G denotes the reciprocal lattice. This result relies heavily on the presence of the orbital frustration, which appears with

$$\sum_{\alpha} e^{2i\phi_\alpha} = 0 \quad (2.16)$$

and is employed in showing that the $T_{\vec{k}\alpha}$ may be used for parameterize the constraints.

2.5.3 Orbital Ordering

The double-exchange is a second-order hopping process, and so ought to be much stronger than the weaker fourth order super exchange and hence more able to compete with the omitted structural interactions. The phase diagrams involve a cubic phase in the ferromagnetic metallic regions, which suggests that no static Jahn-Teller distortion is present and that the motion of the electrons is dominating the structural effects.

M. W. Long [79] chosen double-exchange representation

$$H_1 = -\frac{t}{2} \sum_{\alpha} \sum_{\langle ii'\rangle\alpha} [e^{-i\phi_\alpha/2} u_i + e^{i\phi_\alpha/2} d_i] [e^{i\phi_\alpha/2} u_{i'} + e^{-i\phi_\alpha/2} d_{i'}] \quad (2.17)$$

and attempt to solve it at low temperature using the experience with the Hubbard model as a guide. The first elementary theory is that of mean field theory in the

coupling limit. As the on site energy, U , is permitted to become large, charge fluctuations are eradicated. In a non-interacting state of mean field theory, these forces each site to orientate its permitted pseudo-spins along a fixed quantization axis. The pseudo-spin representation,

$$H_1 = -t \sum_{\alpha} \sum_{\langle i i' \rangle_{\alpha}} |i, \pi/2, \phi_{\alpha} \rangle \langle i', \pi/2, \phi_{\alpha}|, \quad (2.18)$$

is very convenient for this limit providing

$$\begin{aligned} H_1 &= -t \sum_{\alpha} \sum_{\langle i i' \rangle_{\alpha}} \langle \pi/2, \phi_i | \pi/2, \phi_{\alpha} \rangle \langle \pi/2, \phi_{\alpha} | \pi/2, \phi_{i'} \rangle c_i^{\dagger} c_{i'} \\ &= -t \sum_{\alpha} \sum_{\langle i i' \rangle_{\alpha}} \cos \frac{1}{2}(\phi_i - \phi_{\alpha}) \cos \frac{1}{2}(\phi_{i'} - \phi_{\alpha}) c_i^{\dagger} c_{i'} \end{aligned} \quad 2.19$$

where c_i^{\dagger} creates an electron with the chosen orientation on site i , we have used the usual spin half representation to evaluate the matrix elements. This is more complicated than the usual Hubbard model result, which can be seen from 2.20

$$\cos \frac{1}{2}(\phi_i - \phi_{\alpha}) \cos(\phi_{i'} - \phi_{\alpha}) = \frac{1}{2} \left[\cos \left(\frac{1}{2}(\phi_i + \phi_{i'}) - \phi_{\alpha} \right) + \cos \left(\frac{1}{2}(\phi_i - \phi_{i'}) \right) \right] \quad 2.20$$

where the second term occurs in the isotropic Hubbard model and prefers all the orientation to parallel. The first term involves the band orientations might be expected to average out to zero. M. W. Long simply assume that the orbital all align and simply calculate the preferred orbital for the motion. In this orbital models the particles find it much more difficult to exchange around loops and result might be expected to the relevant.

The calculation reduces to a comparison of different dispersions. For each choice of orbital he found dispersion in terms of ϕ the orientation of the orbital.

$$\epsilon_k = -\frac{3}{2} \sum_{\alpha} \cos^2 \frac{1}{2}(\phi - \phi_{\alpha}) \cos k_{\alpha} \quad 2.21$$

For each band-filling, one can evaluate the energies for different values of ϕ and compare.

2.6 Orbital State Study of Mn in CMR Material by Magnetic Compton Profile Measurement

Perovskite Mn oxides have been studied in relation to the colossal magneto resistance (CMR), which is a huge decrease in electric resistance under a magnetic field. Recently, the double layered manganite $\text{La}_{2-2x}\text{Sr}_{1+2x}\text{Mn}_2\text{O}_7$ has become of special interest, because it shows much larger CMR than the base compound $\text{La}_{1-x}\text{Sr}_x\text{MnO}_3$. As shown in Fig.2.11, the crystal structure has a common feature in perovskite manganites that the Mn ion is octahedrally surrounded by O ions. In this crystal field, the energy levels of Mn $3d$ orbitals (which is 5-fold degenerated in a free atomic state) split into a triply degenerate t_{2g} and a doubly degenerate e_g state. When a hole is doped in this system, which is introduced by Sr^{2+} ion doping, it goes into the e_g orbital. That makes e_g electrons hop around the Mn sites. The hopping also causes ferromagnetic alignment of the Mn spins through the strong Hund's coupling with localized t_{2g} spins. This is what we call the double exchange (DE) mechanism. It can explain both the coexistence of metallic conduct ion and ferromagnetism in manganites [80]. However, recent experimental results have revealed that the magnitude of CMR and complicated magnetic phase diagrams cannot be explained only by the simple DE mechanism [26, 81, 82]. The importance of the orbital degree of freedom is pointed out as well as the charge and spin ones. This means that the populations of $x^2 - y^2$ and $3z^2 - r^2$ orbitals in the e_g state play a key role in understanding the transport and magnetic properties of this system. We have investigated the orbital state in $\text{La}_{2-2x}\text{Sr}_{1+2x}\text{Mn}_2\text{O}_7$ by magnetic Compton profile (MCP) measurement [83]. The MCP measurement has been used as a unique method to determine the electron-spin momentum density in ferromagnetic materials. In addition, it has the following advantages to define the orbital occupation; that is, MCP changes its shape depending on the orbital state occupied by magnetic electrons, and it also depends on the direction of the scattering vector of X-rays with respect to the crystalline axis. These features enable us to differentiate the electron population in $x^2 - y^2$ and $3z^2 - r^2$ orbitals together with t_{2g} state through the measurement of MCP by using a single crystalline sample.

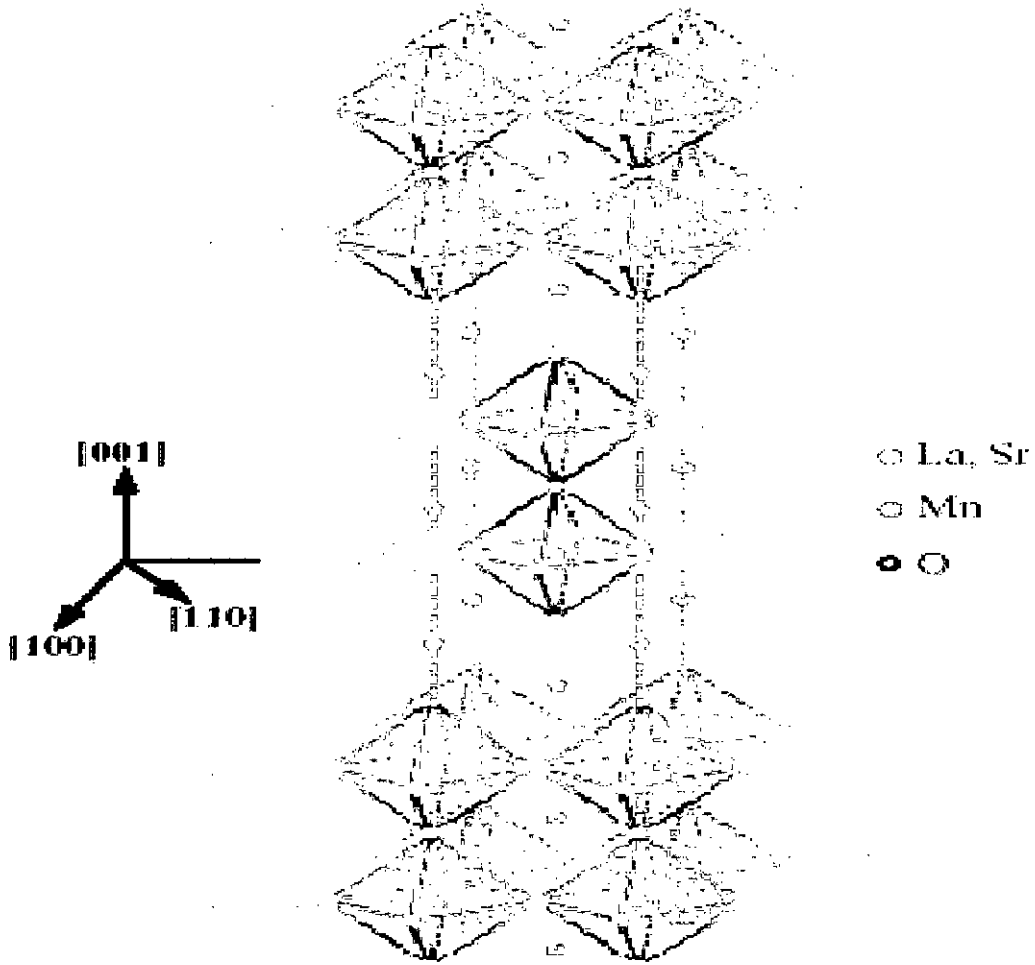


Figure 2.11: The crystal structure of $\text{La}_{2-2x}\text{Sr}_{1+2x}\text{Mn}_2\text{O}_7$.

Experiments have been made at beam line BL08W using circularly polarized X-rays of 270 keV. The MCP's were measured along $[100]$, $[110]$ and $[001]$ directions for $\text{La}_{2-2x}\text{Sr}_{1+2x}\text{Mn}_2\text{O}_7$ with $x = 0.35$ and 0.42 . Figures 2.12 and 2.13 show respectively the MCP's of $x = 0.35$ and 0.42 samples obtained at 10 K. The clear anisotropy of MCP reflects the orbital state of magnetic electrons on Mn site. These MCP's were explained by theoretical Compton profiles obtained from an *ab initio* molecular orbital calculation for the $(\text{MnO}_6)^{8-}$ cluster which takes the hybridization effect between Mn $3d$ and O $2p$ orbitals into account. The theoretical analysis of the orbital state was made using these following conditions: Each MCP is normalized by the magnetic electron numbers per site estimated from the hole concentration x .

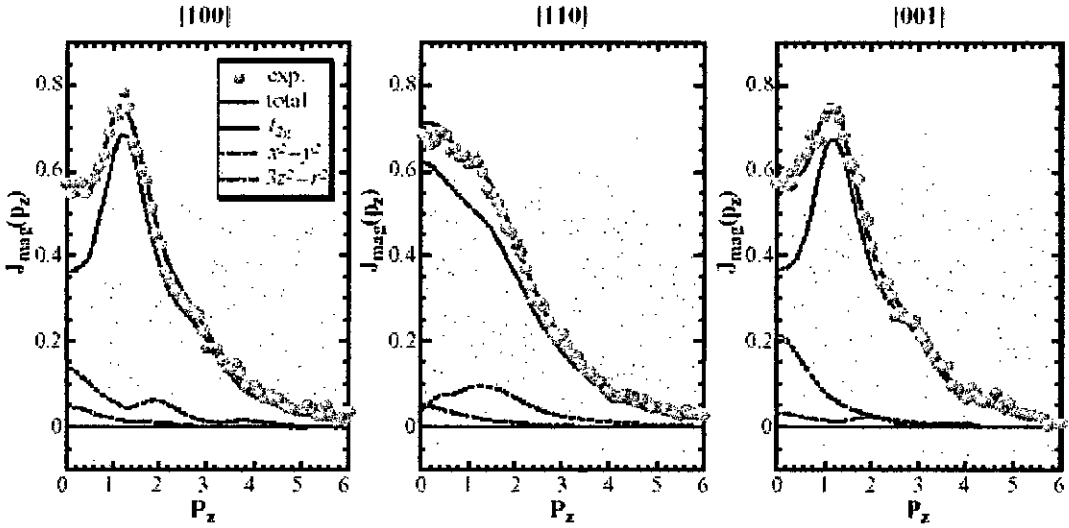
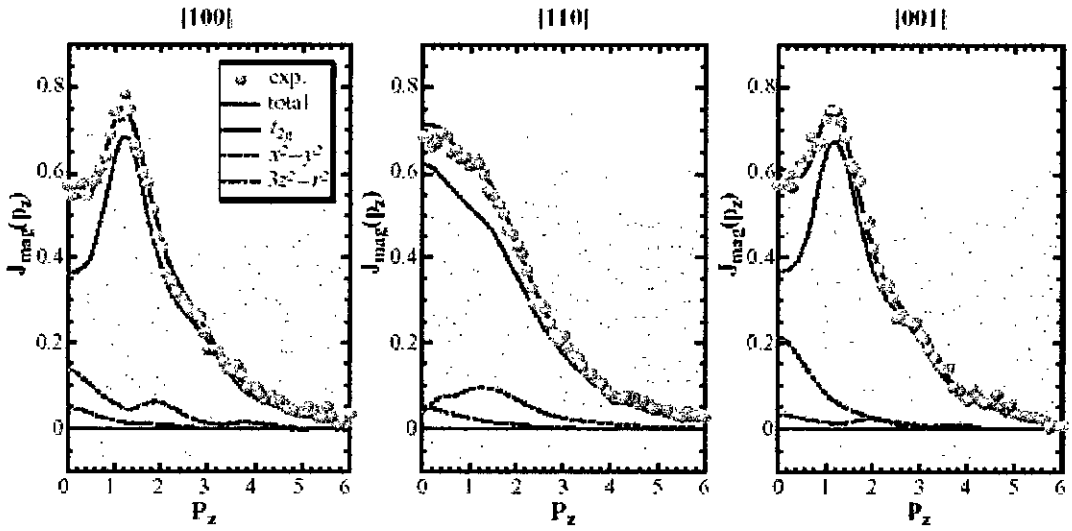


Figure 2.12: The magnetic Compton profiles along the [100], [110] and [001] directions in $\text{La}_{2-2x}\text{Sr}_{1+2x}\text{Mn}_2\text{O}_7$ with $x = 0.35$. Experimental data (solid circles) are shown with fit (solid gray line) using the MnO_6 cluster orbitals. Also shown are the t_{2g} orbital (dotted green line), x^2-y^2 orbital (dashed red line) and $3z^2-r^2$ orbital (dash-dotted blue line) contributions.

The t_{2g} occupation number is fixed to three per site because it is fully occupied. The remainder is fitted by the profiles of $x^2 - y^2$ and $3z^2 - r^2$ orbitals so that the area of fitted profile coincides with that of experimental one. The results are also shown in Fig 2.12 and Fig 2.13 with the dashed red line and dash dotted blue line. Since the area of a profile is proportional to the number of electron spins in a state, the occupation numbers of $x^2 - y^2$ and $3z^2 - r^2$ orbitals can be thus obtained as 0.47 and 0.18 for $x = 0.35$ respectively, while they are 0.46 and 0.12 for $x = 0.42$. These results show that the e_g orbital state is dominated by the $x^2 - y^2$ -type orbital with almost constant occupation, while the occupation in $3z^2 - r^2$ -type orbital decreases with the increase in the hole concentration x . This conclusion would explain the continuous change of magnetic structure from ferromagnetism via canted antiferromagnetism to A-type antiferromagnetism with an increase of x . The decrease of population in $3z^2 - r^2$ orbital weakens the ferromagnetic coupling between MnO_2 layers through e_g electron hopping. The super exchange coupling between t_{2g} spins gradually overcomes the ferromagnetic coupling resulting in the antiferromagnetic structure at high x values.

Figure 2.13: Same as Fig 2.12 but for $x = 0.42$.

2.7 Effect of doping Ca on polaron hopping in $\text{LaSr}_2\text{Mn}_2\text{O}_7$

Two mechanisms have been proposed for the charge transport in systems where the carriers are localized. The first proposed by Mott and Davis [84] involves hopping by the carriers called polarons to states of nearly equal energy. Such states are placed at random distances in the lattice due to the randomness in the potential. In the second process also, the conduction takes place by hopping by small polarons, but they hop only to the nearest neighbors and are assisted by the thermal energy. The resistivity, ρ , in this model is expected to follow the equation

$$\rho = \rho_0 T \exp(E_p/k_B T) \quad (2.22)$$

where E_p is the activation energy of the polarons and ρ_0 is a constant. In manganites the resistivity in the paramagnetic state shows the carriers to be localized. Both these models predict the temperature dependence of ρ equally satisfactorily. It is difficult to choose between the two models based on the data of resistivity alone. Also from the studies of mono layer manganites AMnO_3 , it has been observed that the magnetic properties of these compounds can be controlled by varying the size of the A-site ion. When Ca^{2+} is replaced by the larger Sr^{2+} ion, the Curie temperature T_C increases to

~ 370 K in $\text{La}_{0.67}\text{Sr}_{0.33}\text{MnO}_3$ [85]. The structurally distorted manganite $\text{La}_{0.5}\text{Ca}_{0.5}\text{MnO}_3$ (and also $\text{Nd}_{0.5}\text{Ca}_{0.5}\text{MnO}_3$ and $\text{Pr}_{0.5}\text{Ca}_{0.5}\text{MnO}_3$) does not show either a metallic conductivity or a ferromagnetic ordering at any temperature, due to the A-site ion being small, while $\text{La}_{0.5}\text{Sr}_{0.5}\text{MnO}_3$ becomes a ferromagnetic metal at 340 K [30]. We have also varied the magnetic state of the bilayer manganite $\text{LaSr}_2\text{Mn}_2\text{O}_7$ by substituting Sr with Ca. We have measured the resistivity and thermoelectric power (TEP) of these manganites and have found the hopping to be thermally assisted. The TEP data further suggests these polarons to be magnetic in character. Though Mott's model predicts correctly the temperature dependence of ρ , it has been found to be inadequate for these materials as it requires a very large randomness in the potential to predict the strong localization that is observed here. The potential is reduced considerably in the magnetic localization model proposed by Viret *et al* [86] according to which a magnetic random potential (MRP) arising due to the Hund's rule coupling $J\mathbf{H}_s \cdot \mathbf{S}(=Um)$ between the localized t_{2g} electrons (with spin S) and the spin (s) of the e_g electrons forming the conduction band is responsible for this localization of the carriers. The temperature dependence of resistivity is predicted to be

$$\rho = \rho_0 \exp(T_0/T)^{1/3} \quad (2.23)$$

(which is also characteristic of the variable range hopping in two-dimensional systems) both in the paramagnetic as well as the ferromagnetic regions. However, the characteristic temperature (T_0) is different, T_{op} and T_{of} , in the two regions and is given by

$$kT_{\text{op}} = 18\alpha^{-1} U_m v / (1-x) \phi f \quad (T > T_C) \quad (2.24)$$

$$kT_{\text{of}} = kT_{\text{op}} [1 - \{M/MS\}^{-1}] \quad (T < T_C) \quad (2.25)$$

where α^{-1} is the localization length of the carriers and the other symbols have their usual meanings [87]. In the paramagnetic state, the localized spins of the 3d orbital are randomly oriented in the absence of magnetic field. T_{op} therefore is predicted to have a (large) temperature independent value. Below T_C , the internal molecular field reduces these fluctuations, reducing thereby the value of T_0 to T_{of} . T_0 is thus expected

to decrease at the onset of ferromagnetism. A similar decrease is expected with the external field. Here we measured ρ and TEP of $\text{LaSr}_{2-x}\text{Ca}_x\text{Mn}_2\text{O}_7$ with $0 \leq x \leq 0.9$. Above ~ 220 K, ρ shows a semi conducting behavior for all concentrations of Ca. It does not exhibit any discontinuity at the Curie temperature ~ 300 K. TEP is negative in the entire temperature range 220–600 K and decreases in magnitude with increase in x . We plotted $\ln \rho$ vs. $T^{-1/3}$. These plots were linear both above and below T_C . However at the Curie temperature there was no indication of any change in the value of T_0 as expected from eq. (2.25). For the magnetic random potential, TEP has not been formulated, but it is not expected to depend on the nature/type of disorder. It has been calculated for a random lattice potential (within the variable range hopping regime) for which it is proposed to vary with temperature as T^ν where $\nu=(3-m)/(3+m)$, when the density of states of the carriers varies as $(E - E_F)^m$ [88]. Plots of TEP vs. T^ν were not found to be linear for any value of m at all temperatures above T_C . On the other hand, following eq. (2.24), plots of $\ln \rho/T$ vs. $1/T$ were linear over the entire temperature interval 220–600 K with a decrease in the activation energy (E_ρ) at the magnetic ordering temperature as seen in Figure 2.14. Further it is seen from the figure that E_ρ decrease with increase in Ca concentration. The TEP for such a hopping process is expected to vary as $1/T$. The present data showed a $A/T + B/T^2$ dependence for all concentrations of Ca (A and B are arbitrary constants). The presence of T^{-2} term together with the decrease in E_ρ at T_C observed here point towards a magnetic character of the polarons. Liu and Emin [89] have shown the TEP to vary as T^{-2} when the polarons hop amongst the magnetic clusters. Such clusters appear to be present in these samples as their susceptibility at high temperatures gives a large value for the Curie constant amounting to more than ten spins grouped together.

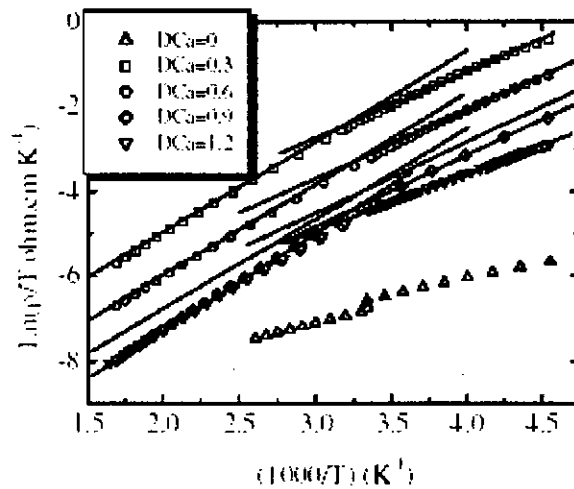


Figure 2.14: Activation energy change of the polarons at the Curie temperature for all concentrations of Ca.

2.8 O(Mn) vibrational bands in double-layered manganites

The colossal magnetoresistance (CMR) manganites have gained prominence recently for their application potential as well as their unusual magnetic and conducting behavior; [90,91] indeed they are a prototype for the complex behavior of the whole range of transition metal oxides[92]. Their magnetic and conducting properties are found to depend sensitively on the electronic correlations within the MnO_2 layers, as modulated by their crystallographic structure and the Mn valance. Raman spectroscopy is particularly well suited to studies of the structure and electronic contributions to bonding in these weakly conducting materials and here we report detailed Raman measurements on several crystals of the CMR and related manganites. The most frequently studied CMR manganites are the pseudocubic versions, doped perovskites $(\text{La}_x\text{A})\text{MnO}_3$, with $A=\text{Sr}, \text{Ca}$. On first glance one would expect at most a very weak Raman signal from these manganites, for without their relatively weak noncubic distortions there would be no Raman active vibrational modes at all. That expectation is nearly true, for the strong lines in the spectra in doped materials are very broad; the only narrow phonon peaks are indeed weak [93–102].

In contrast, stoichiometric LaMnO_3 (LMO) shows Raman lines, which though still weak, are all narrow at and below ambient temperature [102–105]. Those lines in the

stoichiometric material have been confidently assigned on the basis of experimental symmetry determinations and lattice dynamics. In the doped versions of the materials, on the contrary, there is less agreement among authors as to either the detailed spectra or their interpretation. The situation is not aided by the fact that much of the experimental work has been performed on polycrystalline ceramics or thin films, and in both cases there is the potential that the spectra are confused by rogue phases.

In line with general trends in the field most Raman studies on the manganites have concentrated on doped pseudocubic materials $\text{La}_{1-x}\text{Sr}_x\text{MnO}_3$ and $\text{La}_{1-x}\text{Ca}_x\text{MnO}_3$ (LCMO). From the point of view of Raman spectroscopy the double layer manganites of the Ruddlesden-Popper series $R_{2-2x}\text{Sr}_{1+2x}\text{Mn}_2\text{O}_7$, (R -327, R =rare earth) [90] appear to be a more attractive proposition than the pseudocubic form. Not only do they have Raman active modes [106–108] even in the absence of distortions from their ideal tetragonal structure, but in addition they have been prepared with a range of phase diagrams, displaying ferromagnetic, antiferromagnetic, charge-ordering and metal-insulator transitions [109–113].

Here we report spectra of bilayered R -327 for $R = (\text{La}, \text{Pr}, \text{Nd}, \text{Dy})$ and $x < 0.5$, and relate them to published reports on the pseudocubic materials of similar doping. Although the spectra from all these systems differ in the details of their weak, narrow, zone-center phonon lines, there is a remarkable similarity among the materials in the behavior of the two broad features across the $400\text{--}800\text{ cm}^{-1}$ region. We suggest below that these features are from the entire $\text{O}(\text{Mn})$ vibrational band, rendered Raman active by orientational disorder in the Jahn-Teller (JT) displacements of the $\text{O}(\text{Mn})$ ions.

Single crystals of the layered manganites were grown by the floating zone method using an infrared image furnace as described elsewhere [114] Raman experiments were conducted on cleaved surfaces using Jobin-Yvon T64000 and U1000 monochromators with the 514.5, 488, 647.1, and 676.4 nm lines from Ar^+ and Kr^+ lasers. The samples were mounted in vacuum in a closed cycle helium refrigerator.

2.8.1. First-order Raman scattering

In Fig. 2.15 we display low-temperature spectra of a selection of the samples, at $T \sim 30\text{ K}$ in $z(x'x')z^-$ polarization (using the Porto notation) with both incident and scattered

light polarized along the Mn-O bonds. Note that these double-layered crystal data are all on basal-plane surfaces; *c*-axis spectra are substantially different and will be published separately. Equivalent data on the pseudocubic crystals are presented elsewhere. These and all subsequent data curves have been divided by the Bose-Einstein correction factor $[n(\omega, T) + 1] = [1 - \exp(-h\omega/k_B T)]^{-1}$ to account for the sample's temperature, though in our data this correction has only a small effect above 400 cm^{-1} . There are differences in detail between the spectra from the various samples and polarizations, but what is most striking is the similarity as regards the presence of broad bands between 400 and 800 cm^{-1} . The similarity persists through the series despite the widely differing structural, magnetic and conducting states displayed at these temperatures. A similar pattern is found in previously published spectra from the doped manganites [93-102, 106-108].

There is controversy concerning the assignment in earlier reports of the broad features in the 400-800 cm^{-1} range. Their commonality among the nonlayered pseudocubic materials has been noted [95] and based in part on their frequent appearance it has been suggested they are zone-center modes rendered Raman active by disorder in the Jahn-Teller distortions within the MnO_2 planes [94]. However it has not been explicitly recognized that their appearance does not depend on the long-range crystallographic order; to the contrary their absence in stoichiometric LMO in its uniform collective *JT* ground state, suggests that they rely on the randomly oriented *JT* distortions expected in any of the materials with mixed Mn valance. On the other hand, even stoichiometric LMO spectra show broad lines across 400-800 cm^{-1} at temperatures approaching the 800 K collective *JT* transition on the Mn^{+3} sites [97, 105]. Clearly the presence of the disorder introduced either by elevated temperatures or by doping is required to observe the features. It is important to note that in either case the reorientation is local, and can be expected to provide coupling to the entire vibrational band related to the *JT* displacements, rather than to simply the zone-center modes. Thus we assign the broad modes between 400-800 cm^{-1} to scattering from a full phonon branch involving the vibrations of oxygen ions in the MnO_2 planes.

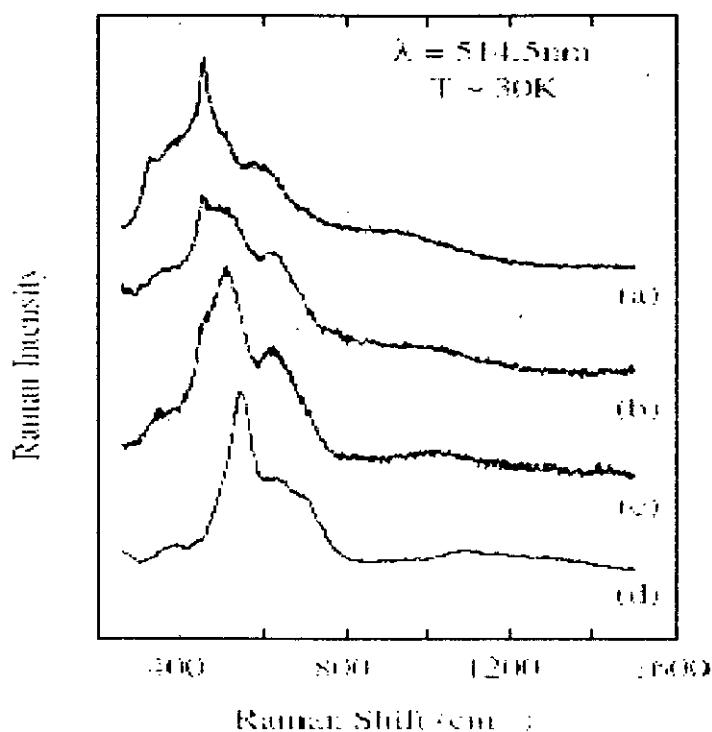


Figure 2.15: Low-temperature Raman spectra of R -327. (a) $R=\text{Pr}$, $x=0.5$, (b) $R=\text{La}$, $x=0.4$, (c) $R=\text{Dy}$, $x=0.4$, and (d) $R=\text{Nd}$, $x=0.4$; taken in the $z(xx)z^-$ polarization, normalized and offset for clarity. Data in all other basal-plane polarization configurations also show the broad features in the $400\text{-}800\text{ cm}^{-1}$ spectral region.

2.8.2. Second-order Raman scattering

Recently [118] it has been suggested that a 2 eV excitation in stoichiometric LMO involves a local atomic rearrangement that rotates the JT displacements about one Mn site in the cooperative JT ground state. Based on that picture a strong second-order Raman signal is predicted. The argument is that the reorientation of the JT O-ion displacements forms a self-trapped exciton, which is described by a superposition of coupled electron multiphonon states. Strong Raman activity to second and higher order is then predicted to occur via Frank-Condon scattering.

The first-order results described in the previous paragraphs are not in disagreement with the model proposed by Allen and Perebeinos. We turn now to higher frequencies, where all of the crystals show second-order scattering seen clearly in Fig. 2.15. The predictions concerning the strength of that second-order scattering are quite different for Frank-Condon as opposed to conventional Raman scattering, so that these spectra provide a test for the Allen and Perebeinos model.

In common with LCMO $\text{Nd}_{1.2}\text{Sr}_{1.8}\text{Mn}_2\text{O}_7$ has a strong second-order signal, which was measurable over the whole temperature range; most of the others had a signal that rose clearly above the background only below 200 K. That higher-order signal is a simple doubling and tripling of the original frequency of the entire broad feature between 400 -800 cm^{-1} , as shown in Fig. 2.16. Also, it is only the broad non-zone-center O(Mn) modes that are repeated in higher order. For instance, we find no evidence of the sharp polarization-dependent mode at 450 cm^{-1} in $\text{PrSr}_2\text{Mn}_2\text{O}_7$ and $\text{La}_{1.2}\text{Sr}_{1.8}\text{Mn}_2\text{O}_7$ (previously assigned to an in-phase O_{xy} bending mode [106]) being represented at higher order. Since it is only the O(Mn) modes that appear in second order, we seek evidence as to whether Frank-Condon scattering is responsible for that second-order signal.

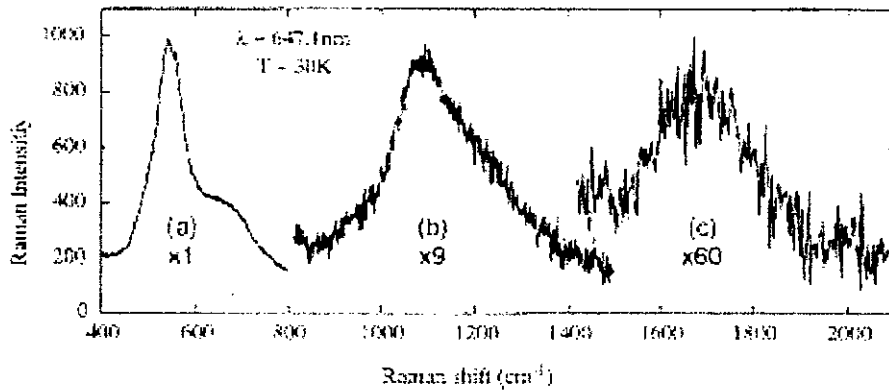


Figure 2.16: Multiple-order scattering in $\text{Nd}_{1.2}\text{Sr}_{1.8}\text{Mn}_2\text{O}_7$ ($x=0.4$). (a) First-order signal unmodified, (b) and (c) second- and third-order scattering with a sloped linear offset subtracted, magnified as shown for clarity.

As a quantitative characterization of the first- and second order Raman signals, we have compared the ratio of their corresponding spectral integrated signal strengths.

For first order this is $I^{(1)} = \int d\omega S^{(1)}(\omega)$, integrated above a sloping linear background and across the broad first-order bands in the region 400-800 cm^{-1} . Similarly, we have calculated $I^{(2)} = \int d\omega S^{(2)}(\omega)$ across matching doubled-frequency limits where we find the second-order signal. In Fig.2.17 we plot the ratio $I^{(2)}/I^{(1)}$ between these two integrated signal strengths, where it can be seen that the ratio clearly falls with increasing temperature. Also, the weakening of $I^{(2)}$ does not appear to be correlated in any way with specific phase transitions, nor does it appear to be strongly dependent on the low temperature phase. Furthermore, it does not show the temperature-independent behavior expected from the Frank-Condon mechanism [118,119] To the

contrary, the increasing second-order signal at low temperatures could be understood on the basis of conventional resonant Raman scattering. Within this picture it arises from an increase at low temperatures of the lifetime of the resonant excitation, the trapped exciton in the Allen and Perebeinos picture.

The amplitude of the resonance is a stronger function of that lifetime in $I^{(2)}$ than in $I^{(1)}$ due to an extra energy term in the denominator of the Raman susceptibility [119] and exactly on resonance the Raman intensity ratio ($I^{(2)}/I^{(1)}$) is then proportional to the square of the lifetime of the excited state. It is important to recognize that all of our crystals are expected to have disordered JT states, with the excitation energy varying among the various Mn^{+3} sites. In the resulting inhomogeneously broadened resonance the lifetime dependence will persist over the entire resonant profile. Thus the temperature dependence of Fig. 2.17 can be understood as reflecting only the temperature dependence of the square of the exciton lifetime.

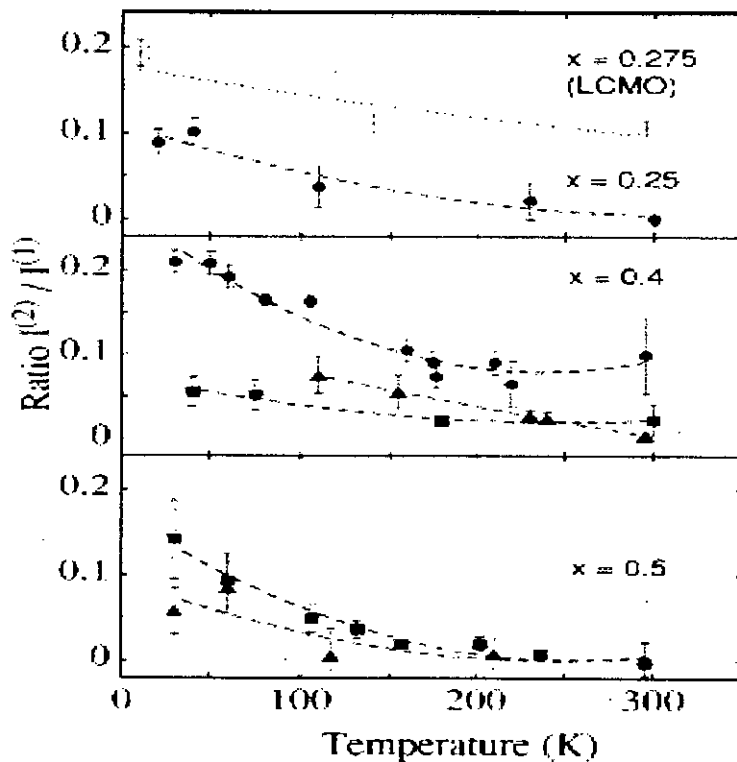


Figure 2.17: Temperature dependence of the second- to first-order spectral integrated intensity ratio with $\lambda=514$ nm from crystals with differing Mn^{2+} fractions x , as labeled. *Solid symbols*: R-327 for Nd (circles), Dy (triangles), and Pr (squares). *Crosses*: an estimate of the integrated intensity ratio for LCMO with $x=0.275$. The lines are guides to the eye.

We have conducted a search for resonance effects in $\text{Nd}_{1.2}\text{Sr}_{1.8}\text{Mn}_2\text{O}_7$ across the 488–647 nm (1.92–2.54 eV) range, which has revealed no significant changes to the spectrum or its temperature dependence. In particular, contrary to an earlier report, [100] we find no new features appearing between 514.5 and 488 nm, so that the both first- and second order signals of the $400\text{--}800\text{ cm}^{-1}$ band can easily be identified in all low-temperature spectra from our crystals. At $T \sim 30\text{ K}$ the ratio $I^{(2)}/I^{(1)}$ increases by about 30% in going from 1.92 to 2.54 eV, approximately as predicted by Perebeinos *et al.* However, the magnitude of the ratio is an order of magnitude smaller than expectations following from the Frank-Condon process. This observation lends further evidence for conventional, rather than Frank-Condon exciton-mediated resonant Raman scattering. We have reported first- and second-order Raman signals in a wide range of manganite crystals. The spectra show a similarity that suggests that the intense broad lines on which we have focused cannot depend on the detailed magnetic, metallic, or charge-ordered state. We assign the features to vibrations in the common element, Mn-O octahedral. The broad nature of the features is consistent with scattering from a full vibrational branch, suggesting in turn that the photon-phonon coupling mechanism involves a local interaction. The presence of a second-order signal is in agreement with a mechanism associated with a local exciton as suggested by Allen and Perebeinos [118], but its magnitude and temperature dependence establishes that it involves conventional resonant Raman scattering rather than the Frank-Condon effect.

2.9 Local Structure of the CMR Oxides from Polarized EXAFS

The observation of "colossal" magnetoresistance [120] (the CMR effect) in the doped manganese-oxide ceramics (manganites) has sparked a great amount of effort aimed at understanding the unusual electronic and magnetic properties of these materials. Its generic behavior of ferromagnetic metal to paramagnetic insulator transition with CMR near the T_c is understood to first order within the framework of double exchange theory, which says that the effective bandwidth (and hence conductivity) changes with the spin ordering in the crystal [6,7,80]. Recently there has been a realization that although double exchange is clearly important for understanding the behavior of the manganites, it is not enough [8,14]. The model alone can not explain

it's high resistivity, fast doping dependency, and incorrect behavior in resistivity for $T < T_c$. Perhaps the most discussed mechanism to supplement double exchange is polaron formation due to a very large electron-phonon coupling originating from strong Jahn-Teller (J-T) coupling [8]. It has been argued that a delicate balance exists between the electron phonon coupling energy and the electron itinerancy energy, such that small polarons form above but not below T_c [121]. Our earlier work under this proposal as well as our work under proposal 2393B has focused on the electronic structure of the manganites using x-ray absorption spectroscopy (XAS) and angle-resolved photoemission (ARPES). These studies [122,123] as well as work by other groups have indicated the large role of the lattice in the physics of these compounds. To better understand this physics and to complement our electronic structure studies, we have undertaken a study of the local structure of these compounds using EXAFS. The measurements have been performed on high quality single crystals of the formula unit $\text{La}_{1.2}\text{Sr}_{1.8}\text{Mn}_2\text{O}_7$. These are 2-dimensional (layered) samples, with the main structural elements being a bilayer of square MnO_2 planes which are isostructural to the CuO_2 planes found in the high T_c superconductors. In between the MnO_2 planes are (La,Sr)-O layers which are typically believed to be mostly ionic and help hold the MnO_2 planes together as well as doping carriers to the MnO_2 planes. The details of the samples and growth procedures may be found in reference [26]. Since we wished to take advantage of the polarization of the synchrotron radiation to monitor the bond lengths in different directions, we performed the measurements in fluorescence mode off of single crystal samples. The experiments were performed at the beam line 4 wiggler lines using a 13-channel Ge detector to monitor the fluorescence. Figure 2.18 shows a compilation of data extracted from the measurements obtained on a $T_c=126\text{K}$ sample. The Debye-Waller factor σ_2 is plotted vs. temperature for each of three Mn-O bonds extracted from the data. As shown in the inset to the figure, O_3 corresponds to the in-plane oxygen atoms, The O_1 are the out-of-plane oxygens in between the double MnO_2 planes, and the O_2 are the out-of plane oxygen atoms directed away from the bi-planes. The in-plane polarized data sensitive to the Mn- O_3 bonds does not show much anomalous temperature dependences. The out-of plane Mn- O_2 bonds are very active across the transition temperature, signaling a large coupling of the

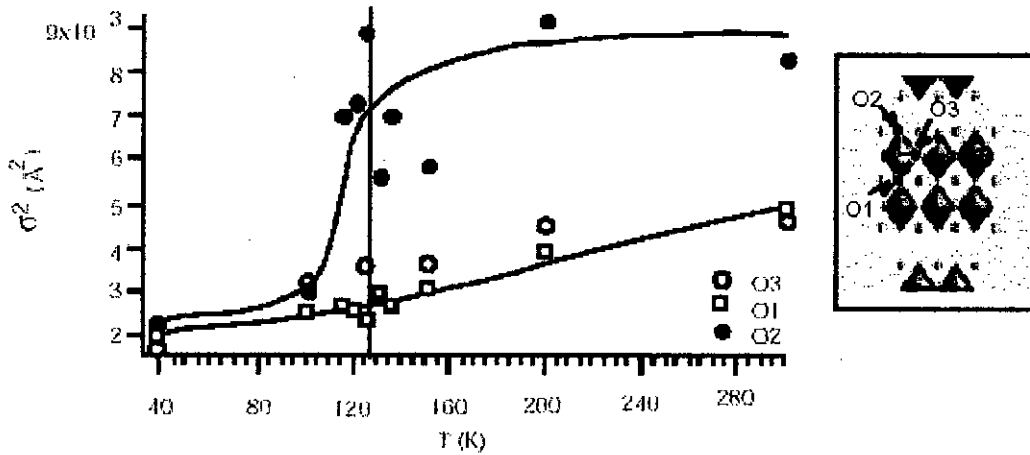


Figure 2.18: σ^2 as a function of temperature for the different Mn-O bonds in the layered colossal magnetoresistive oxide $\text{La}_{1.2}\text{Sr}_{1.8}\text{Mn}_2\text{O}_7$ ($T_c = 126\text{K}$). The data was extracted from EXAFS measurements performed at the beam line 4 branch lines at SSRL. The different oxygen atoms are indicated in the inset (the Mn atoms are at the center of the octahedra). The lines are guides to the eye for the O1 and O2 data.

electronic and magnetic properties (which also change across the transition temperature) to the lattice degrees of freedom in this direction. While the coupling of the electronic, magnetic, and lattice degrees of freedom in these materials was expected, it is surprising that it is the out-of-plane bonds that are the most active, since the electronic and magnetic structure had been believed to be dominated by the in-plane states.

2.10 Manganite-Based Device

Based on the properties discussed above, a number of device approaches are being explored, and we will discuss them sequentially as below:

(i) **Magnetic field sensors** (a) using the CMR effect in a film (b) using a spin valve structure, and (c) as a microwave CMR sensors. The industrial requirements for a magnetic sensor are operation at room temperature and up to 400K, at least a 20% MR at a field 10 mT applied field, temperature independent CMR values over 350 ± 50 K and acceptable noise values. The current thinking is that oxide-based CMR sensors will have maximum impact only on memory systems approaching densities of 100 Gb cm^{-2} .

(ii) **Electrical field effect devices** (a) using a SrTiO_3 gate and (b) using a ferroelectric gate. Field Effect Transistors (FET) based on CMR channels show some interesting characteristic depending on the dielectric layer on top as to whether it is a paraelectric layer, such as STO, or a ferroelectric layer, such as PZT. The advantage of these devices unlike conventional NVRAM would be that the reading of the state of memory would be direct since the resistances are considerably different in the two states thus will not require to rewrite of the memory.

(iii) Room Temperature Bolometric Infrared (IR) sensors

Due to the advances in thermoelectric cooling, materials with high thermal nonlinearities in the temperature range of 250-300 K, are potential candidates for bolometric sensors. The commercial bolometers based on VO_x used now a days use temperature coefficient of resistance (TCR) values around 2.5% to 4%. In comparison TCR values ranging from 8% to 18 % are possible in the LCMO manganites over the same temperature range (figure 2.19).

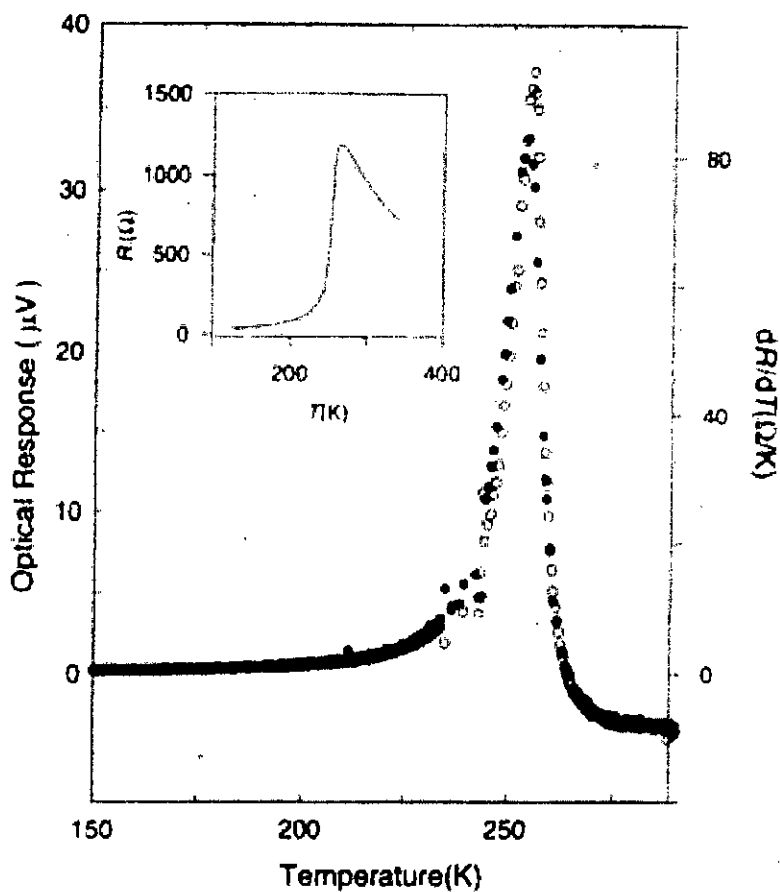


Figure 2.19: Optical response of a film of LCMO (closed circles) in comparison with the TCR (open circles). The R-T curve is shown in the inset [124].

(iv) Low temperature hybrid HTS-CMR devices

As the properties of CMR materials are quite spectacular at reduced temperatures, i.e., below 100K, there may be some advantages to integrating them with HTS devices.

References

- [1] S.P.P. Parkin, *Annu. Rev. Mater. Sci.* **25** 357 (1995)
- [2] J.B. Goodenough *Magnetism and the Chemical Bond* (Huntington: Krieger) (1976)
- [3] G.H. Jonker and J.H. Van Santen, *Physica* **16** 337 (1950)
- [4] J.H. Van Santen and G.H. Jonker, *Physica* **16** 599 (1950)
- [5] C. Zener, *Phys. Rev.* **81** 440 (1951)
- [6] P.W. Anderson and H. Hasegawa, *Phys. Rev.* **100** 675 (1955)
- [7] P.G. De Gennes, *Phys. Rev.* **118** 141 (1960)
- [8] A.J. Millis, P.B. Littlewood and B.I. Shraiman, *Phys. Rev. Lett.* **74** 5144 (1995)
- [9] S. Jin, T.H. Tiefel, M. McCormack, R.A. Fastnacht, R. Ramesh and J.H. Chen, *Science* **264** 413 (1994)
- [10] Y. Tomioka, A. Asamitsu, Y. Moritomo, H. Kuwahara and Y. Tokura, *Phys. Rev. Lett.* **74** 5108 (1995)
- [11] E.O. Wollan and W.C. Koehler, *Phys. Rev.* **100** 545 (1955)
- [12] A.P. Ramirez, P. Schiffer, S.W. Cheong, W. Bao, T.T.M. Palstra, P.L. Gammel, D.J. Bishop and B. Zegarski, *Phys. Rev. Lett.* **76** 3188 (1996)
- [13] A.J. Millis, B.I. Shraiman and R. Mueller, *Phys. Rev. Lett.* **77** 175 (1996)
- [14] H. Rode, J. Zhang and A.R. Bishop, *Phys. Rev. Lett.* **76** 1356 (1996)
- [15] G. Zhao, K. Conder, H. Keller and K.A. Muller, *Nature* **381** 676 (1996)
- [16] P. Dai, J. Zhang, H.A. Mook, S.H. Liou, P.A. Dowben and E.W. Plummer, *Phys. Rev. B* **54** R3694 (1996)
- [17] J.R. Fletcher and K.W.H. Stephens, *J. Phys. C: Solid State Phys.* **2** 444 (1969)
- [18] J.B.A.A. Elemans, B. VanLaar, K.R. Van Der Veen and B.O. Loopstra, *J. Solid State Chem.* **3** 238 (1971)
- [19] Y. Shimakawa, Y. Kubo and T. Manako, *Nature* **379** 53 (1996)
- [20] A.P. Ramirez, R.J. Cava and J. Krajewski, *Nature* **387** 268 (1997)
- [21] J.B. Goodenough, *Phys. Rev.* **100** 564 (1955)
- [22] Z. Jirak, S. Krupicka, Z. Simsa, M. Dlouha and S. Vratilav, *J. Magn. Magn. Mater.* **53** 153 (1985)
- [23] C.M. Varma, *Phys. Rev. B* **54** 7328 (1996)
- [24] S. Satpathy, Z.S. Popovic and F.R. Vukajlovic, *Phys. Rev. Lett.* **76** 960 (1996)
- [25] J.H. Park, C.T. Chen, S.W. Cheong, W. Bao, G. Meigs, V. Chakarian and Y.U. Idzerda, *Phys. Rev. Lett.* **76** 4215 (1996)
- [26] Y. Moritomo, A. Asamitsu, H. Kuwahara and Y. Tokura, *Nature* **380** 141 (1996)
- [27] A. Urushibara, Y. Moritomo, T. Arima, A. Asamitsu, G. Kido and Y. Tokura, *Phys. Rev. B* **51** 14 103 (1995)
- [28] J.S. Helman and B. Abeles, *Phys. Rev. Lett.* **37** 1429 (1976)
- [29] P. Schiffer, A.P. Ramirez, W. Bao and S.W. Cheong, *Phys. Rev. Lett.* **75** 3336 (1995)
- [30] Y. Moritomo, Y. Tomioka, A. Asamitsu, Y. Tokura and Y. Matsui, *Phys. Rev. B* **51** 3297 (1995)
- [31] W. Bao, C.H. Chen, S.A. Carter and S.W. Cheong, *Solid State Commun.* **98** 55 (1996)
- [32] B.J. Sternlieb, J.P. Hill, U.C. Wildgruber, G.M. Luke, B. Nachumi, Y. Moritomo and Y. Tokura, *Phys. Rev. Lett.* **76** 2169 (1996)
- [33] H. Asano, J. Hayakawa and M. Matsui, *Appl. Phys. Lett.* **68** 3638 (1996)
- [34] T. Kimura, Y. Tomioka, H. Kuwahara, A. Asamitsu, M. Tamura and Y. Tokura, *Science* **274** 1698 (1996)
- [35] P.D. Battle, M.A. Green, N.S. Laskey, J.E. Millburn, M.J. Rosseinsky, S.P. Sullivan and J.F. Vente, *Chem. Commun.* **1996** 767 (1996)
- [36] R. Seshadri, C. Martin, A. Maignan, M. Hervieu, C. Raveau and C.N. Rao, *J. Mater. Chem.* **6** 1585 (1996)
- [37] P.D. Battle *et al.* *J. Phys.: Condens. Matter* **8** L427 (1996)

- [38] P.D. Battle, M.A. Green, N.S. Laskey, J.E. Milburn, P.G. Radaelli, M.J. Rosseinsky, S.P. Sullivan and J.F. Vente, *Phys. Rev. B* **54** 15967 (1996)
- [39] P.D. Battle, M.A. Green, N.S. Laskey, J.E. Millburn, L. Murphy, M.J. Rosseinsky, S.P. Sullivan and J.F. Vente, *Chem. Mater.* **9** 552 (1997)
- [40] N.F. Mott *metal-insulator transitions*, 2nd edn. London: Taylor and Francis (1995)
- [41] M. F. Hundley, M. Hawley, R. H. Heffner, Q. X. Jia, J. J. Neumeier, J. Tesmer, J. D. Thomson, & X.D.Wu, *Appl. Phys. Lett.* **67**, 860(1995)
- [42] M. Virect, L. Ranno & J.M.D.Coe, *Phys. Rev. B* **55**,8067 (1997)
- [43] M. Virect, M. Drouet, J.P. Contour, J. Nassar, C. Fermon, & A. Fert, *Europhys. Lett.* **39**,545 (1997).
- [44] N. F. Mott & E. Davis, *Electronic processes in noncrystalline materials*. Oxford University Press (1971)
- [45] D.M.J. Coey, M. Virect, L. Ranno, & K. Ounadjela, *Phys. Rev. Lett* **75**, 3910 (1995).
- [46] S.J.L. Billinge, R.G. Di Francesco, G.W. Kwei, J.J. Neumeier, J.D. Thomson, *Phys. Rev. Lett* **77**, 715 (1996)
- [47] G. Snyder, R. Hiskes, S. DiCarolis, M. Beasley & T. Geballe, *Phys. Rev. B* **53**, 1434 (1996)
- [48] G.P. Triberis, L.R. Friedman, *J. Phys. C* **18**, 2281 (1985)
- [49] B.I. Efros & A.L. Shklovskii, *Electronic properties of doped semiconductors*. Berlin: Springer. (1984)
- [50] J.M.D. Coey, *Phil. Trans. R. soc. Lond. A* **356**, 1519 (1998)
- [51] M. Jaime, M.B. Salamon, M. Rubinstein, R.E. Treece, J.S. Horwitz and D.B. Chrisey, *Phys. Rev. B* **54** 11 914 (1996)
- [52] T.T.M. Palstra, A.P. Ramirez, S.W. Cheong, B.R. Zegarski, P. Schiffer and J. Zaanen, unpublished, 1996
- [53] R.C. Miller, R.R. Heikes and R. Mazelsky, *J. Appl. Phys.* **32** (Supplement 2202) (1961)
- [54] J. Fontcuberta, A. Seffar, X. Granados, J.L. Garcia-Munoz, X. Obradors and S. Pinol, *Appl. Phys. Lett.* **68** 2288 (1996)
- [55] A. Asamitsu, Y. Moritomo and Y. Tokura, *Phys. Rev. B* **53** R2952 (1996)
- [56] T. Hashimoto, N. Ishizawa, N. Mizutani and M. Kato, *J. Mater. Res.* **23** 1102 (1988)
- [57] M. Jaime, M.B. Salamon, K. Pettit, M. Rubinstein, R.E. Treece, J.S. Horwitz and D.B. Chrisey, *Appl. Phys. Lett.* **68** 1576 (1996)
- [58] M.F. Hundley and J.J. Neumeier, *Phys. Rev. B* **55** 11 511 (1997)
- [59] S.M. Girvin, *J. Solid State Chem.* **25** 65 (1978)
- [60] H.Y. Hwang, S.W. Cheong, N.P. Ong and B. Batlogg, *Phys. Rev. Lett.* **77** 2041 (1996)
- [61] A.E. Berkowitz, J.R. Mitchell, M.J. Carey, A.P. Young, S. Zhang, F.E. Spada, F.T. Parker, A. Hutten and G. Thomas, *Phys. Rev. Lett.* **68** 3745 (1992)
- [62] A. Gupta, G.Q. Gong, G. Xiao, P.R. Duncombe, P. Lecoeur, P. Trouilloud, Y.Y. Wang, V.P. Dravid and J.Z. Sun, *Phys. Rev. B* **54** R15629 (1996)
- [63] J.Z. Sun, W.J. Gallagher, P.R. Duncombe, L. Krusin-Elbaum, R.A. Altman, A. Gupta, Y. Lu, G.Q. Gong and G. Xiao, *Appl. Phys. Lett.* **69** 3266 (1996)
- [64] Y. Lu, X.W. Li, G.Q. Gong, G. Xiao, A. Gupta, P. Lecoeur, J.Z. Sun, Y.Y. Wang and V.P. Dravid, *Phys. Rev. B* **54** R8357 (1996)
- [65] N.D. Mathur, G. Burnell, S.P. Isaac, T.J. Jackson, B.S. Teo, J.L. MacManus-Driscoll, L.F. Cohen, J.E. Evetts and M.G. Blamire, *Nature* **387** 266 (1997)
- [66] H.Y. Hwang, S.W. Cheong and B. Batlogg, *Appl. Phys. Lett.* **68** 3494 (1996)
- [67] G.B. Alers, A.P. Ramirez and S. Jin, *Appl. Phys. Lett.* **68** 3644 (1996)
- [68] K. Kubo and N. Ohata, *J. Phys. Soc. Japan* **33** 21 (1972)
- [69] G.J. Snyder, R. Hiskes, S. DiCarolis, M.R. Beasley and T.H. Geballe, *Phys. Rev. B* **53** 14 434 (1996)
- [70] E. O. Wollan and W. C. Koehler, *Phys. Rev.* **100**, 545 (1955)

- [71] H. Y. Hwang, S.-W. Cheong, P. G. Radaelli, M. Marezio & B. Batlogg, *Phys. Rev. Lett.* **75** (2), 914 (1995).
- [72] J. L. Garcia-Munoz, J. Fontcuberta, M. Suaaidi, & X. Obradors, *J. of Phys. Cond. Matt.* **8**, L787 (1996a).
- [73] P. S. I. P. N. de Silva, F. M. Richards, L. F. Cohen, J.A. Alonso, M. J. Martinez-Lope, M.T. Casais, T. Kodenkandath & J. L. MacManus-Driscoll, *J. App. Phys.* **83** (1), 394 (1998).
- [74] J. L. Garcia-Munoz, J. Fontcuberta, B. Martinez, A. Seffar, S. Pinol & X. Obradors, *Phys. Rev. B* **55** (2), R-668 (1997).
- [75] M. Lide, J. Rodriguez-Martinez and J. Paul Attfield, *Phys. Rev. B* **58** (5), 2426 (1998).
- [76] A. J. Millis, P. B. Littlewood, & B. I. Shraiman, *Phys. Rev. Lett.* **74**, 5144 (1995)
- [77] A. J. Millis, R. Mueller, and B. I. Shraiman., *Phys. Rev. B* **54** (8), 5405 (1996).
- [78] A. J. Millis, *Phil. Trans. R. soc. Lond. A* **356**, 1473 (1998).
- [79] M. W. Long, *Phil. Trans. R. soc. Lond. A* **356**, 1493 (1998)
- [80] C. Zener, *Phys. Rev.* **82** 403 (1951).
- [81] K.Hirota, Y. Moritomo, H. Fujioka, M. Kubota, H. Yoshizawa and Y. Endoh, *J. Phys. Soc. Jpn.* **67**, 3380(1998)
- [82] M. Kubota, H. Fujioka, K. Hirota, K. Ohoyama, Y. Moritomo, H. Yoshizawa and Y. Endoh *J. Phys. Soc. Jpn.* **69**, 1606(2000)
- [83] A. Koizumi, S. Miyaki, Y. Kakutani, H. Koizumi, N. Hiraoka, K. Makoshi, N. Sakai, K. Hirota and Y. Murakami, *Phys. Rev. Lett.* **86** 5589 (2001).
- [84] N.F. Mott and E.A. Davis in *Electronic processes in non-crystalline materials* (Clarendon Press, Oxford, 1971)
- [85] J. Fontcuberta, *J. Appl. Phys.* **79**, 5181 (1996)
- [86] M. Viret, L. Ranno and J.M.D. Coey, *J. Appl. Phys.* **81**, 4964 (1996)
- [87] O.A. Yassin, Ph.D. thesis (Indian Institute of Physics, Bombay, 2000)
- [88] I.P. Zvyagin in *Hopping transport in solids* edited by M. Pollak and B. Shklovskii (North Holland, Amsterdam, 1991) p. 147
- [89] N.Liu and D. Emin, *Phys. Rev.* **B30**, 13550 (1984)
- [90] A.P. Ramirez, *J. Phys. Condens. Matter* **9**, 8171 (1997)
- [91] M. Imada, A. Fujimori, Y. Tokura, *Rev. Mod. Phys.* **70**, 1039(1998)
- [92] Y. Tokura and N. Nagaosa, *Science* **288**, 462 (2000)
- [93] E. Liarokapis, Th. Leventouri, D. Lampakis, D. Palles, J. J. Neumeier and D. H. Goodwin, *Phys. Rev.* **B 60**, 12758(1999)
- [94] M. V. Abrashev, A. P. Litvinchuk, M. N. Iliev, R. L. Meng, V. N. Popov, V. G. Ivanov, R. A. Chakalov & C. Thomsen, *Phys. Rev.* **B 59**, 4146(1999)
- [95] M. V. Abrashev, *Phys. Status Solidi B* **215**, 631 (1999).
- [96] S. Yoon, H. L. Liu, G. Schollerer, S.L. Cooper, P. D. Han, D. A. Payne, Z. Fisk, *Phys. Rev.* **B 58**, 2795(1998)
- [97] V. B. Podobedov, A. Weber, D. B. Romero, J. P. Rice & H. D. Drew, *Phys. Rev.* **B 58**, 43(1998)
- [98] V. B. Podobedov, D. B. Romero, R. Schreekala, M. Rajeswari, R. Ramesh, T. Venkatesan, and H. D. Drew, *Appl. Phys. Lett.* **73**, 3217(1999)
- [99] J. C. Irwin, J. Chrzanowski & J. P. Franck, *Phys. Rev.* **B 59**, 9362(1999)
- [100] V. Dediu, C. Ferdeghini, F. C. Maticotta, P. Nozar, and G. Ruani, *Phys. Rev. Lett.* **84**, 4489(2000)
- [101] P. Björnsson, M. Rübhausen, J. Bäckström, and M. Käll, *Phys. Rev. B* **61**, 1193(2000)

- [102] E. Granado, N. O. Moreno, A. García, J. A. Sanjurjo, C. Rettori, and I. Torriani, *Phys. Rev. B* **58**, 11435(1998)
- [103] M. N. Iliev, M. V. Abrashev, H.-G. Lee, V. N. Popov, Y. Y. Sun, R. L. Meng and C. W. Chu, *Phys. Rev. B* **57**, 2872(1998)
- [104] E. Granado, A. García, J. A. Sanjurjo, C. Rettori, I. Torriani, F. Prado, R. D. Sánchez, and A. Caneiro, *Phys. Rev. B* **60**, 11879(1999)
- [105] E. Granado, J. A. Sanjurjo, C. Rettori, J. J. Neumeier & S. B. Oseroff, *Phys. Rev. B* **62**, 11304(2000)
- [106] D. B. Romero, V. B. Podobedov, A. Weber, and J. P. Rice, *Phys. Rev. B* **58**, R14737(1998)
- [107] D. N. Argyriou, H. N. Bordallo, B. J. Campbell, A. K. Cheetham, *Phys. Rev. B* **61**, 15269(2000)
- [108] K. Yamamoto, T. Kimura, T. Ishikawa, T. Katsufuji & Y. Tokura, *Phys. Rev. B* **61**, 14706(2000)
- [109] R. I. Bewley, S. J. Blundell, B. W. Lovett, Th. Jestädt, F. L. Pratt, K. H. Chow and W. Hayes, *Phys. Rev. B* **60**, 12286(1999)
- [110] Y. Moritomo, *Aust. J. Phys.* **52**, 255 (1999).
- [111] N. H. Hur, Jin-Tae Kim, K. H. Yoo, Y. K. Park, and J.C. Park, *Phys. Rev. B* **57**, 10740(1998)
- [112] T. Kimura, Y. Tomioka, A. Asamitsu, and Y. Tokura, *Phys. Rev. Lett.* **81**, 5920(1998)
- [113] P.D. Battle, *J. Mater. Chem.* **7**, 977 (1997).
- [114] G. Balakrishnan, *J. Phys.: Condens. Matter* **9**, 471 (1997).
- [115] J. F. Mitchell, D. N. Argyriou, J. D. Jorgensen, D. G. Hinks, C. D. Potter, and S. D. Bader, *Phys. Rev. B* **55**, 63 (1997)
- [116] B. García-Landa, M. R. Ibarra, G. Balakrishnan, M. R. Lees and D. McK Paul, *Phys. Rev. B* **60**, 5440(1999)
- [117] B. García-Landa, C. Marquina, M. R. Ibarra, G. Balakrishnan, M. R. Lees, and D. McK. Paul *Phys. Rev. B* **60**, 5440(1999)
- [118] P.B. Allen and V. Perebeinos, *Phys. Rev. Lett.* **83**, 4828 (1999).
- [119] M. Cardona, in *Light Scattering in Solids II*, edited by M. Cardona and G. Guntherdot, Topics in *Applied Physics*, Vol. 50 (Springer-Verlag, Berlin, 1982).
- [120] R. M. Kusters et al., *Physica B* **155**, 362 (1989); Y. Tokura et al., *J. Phys. Soc. Jpn.* **63**, 3931 (1994); S. Jin et al., *Science* **264**, 413 (1994)
- [121] A. J. Millis et al., *Phys. Rev. B* **54**, 5389 (1996)
- [122] D.S. Dessau, C.H. Park, T. Saitoh, Z.X. Shen, P. Villella, N. Hamada, Y. Moritomo, Y. Tokura, *Phys. Rev. Lett.* (1998)
- [123] D.S. Dessau, T. Saitoh, C.H. Park, Z.X. Shen, Y. Moritomo and Y. Tokura, *Science and Technology of Magnetic Oxides, Materials Research Society Symposium Proceedings* **494**,181 (1998)
- [124] T. Venkatesan, M. Rajeswari, Z.W. Dong, S.B. Ogale & R.. Ramesh, *Phil. Trans. R. soc. Lond. A* **356**, 1661 (1998)

Chapter 3

Sample Preparation and Experimental Techniques

In this chapter basic techniques of sample preparation and experimental technique are given. We also described construction of a few locally fabricated apparatus. These apparatus were used for the magnetoresistance measurements.

3.1 Sample Preparation

Samples can be prepared mainly using any of the following four method

3.1.1 Solid state reaction method

In solid state reaction method appropriate amounts of the chemical constituents are carefully ground together and mixed thoroughly in a mortar and pestle or ball mills. Ground powders are then calcined in air or in oxygen at a temperature above 750 °C for several hours, then reground and reheated. This process is continued until the mixture is converted into the correct crystalline phase. This calcined material are then ground to fine powders, palletised in a hydraulic press followed by sintering at different temperatures (below the melting point of the materials) in air or any in controlled atmosphere.

3.1.2 Solution method

In this method appropriate amount of solid chemicals are at first dissolved in nitric acid or in any other solvent. This solution is then dried and then followed by calcination and sintering treatments. Some times water soluble materials such as nitrates are used for synthesizing superconducting ceramic materials. The nitrates are dissolved in water and then dried and calcined in a way similar to the solid state reaction method.

3.1.3 Melt-quenched or glass ceramic method

In this method appropriate amounts of mixed powder are taken in a oxides, carbonates etc crucible and are calcined for about two hours below the melting point of the materials. After calcination the powders are melted at a few hundred-degree

Celsius above the melting temperature and held there for a couple of hours. The melts are then poured into a cold iron or brass plate and pressed quickly by another plate to 1 to 2 mm thick sheets. The glasses thus obtained are then annealed at suitable temperatures for different periods of time in air or in any controlled atmosphere.

3.1.4 Thin film method

Thin film of superconducting materials have been very successfully fabricated using the procedure like, Evaporation, Sputtering, Ion Beam sputtering, Laser Evaporation etc. Evaporation is conceptually the simplest of all the deposition techniques. In practice, however, some of the most sophisticated apparatus are used to evaporate epitaxial films of materials under very controlled conditions and these systems are more accurately called molecular electron beam epitaxy system (MBE/EBE). The technique involved utilises a vacuum system to remove most of the contaminating gases from the deposition chamber. Typical pressures that are obtained in simple evaporations are in the 10^{-7} torr range until the MBE/EBE system requires pressures of less than 10^{-10} torr. The elements or compounds to be evaporated are heated in crucibles by either resistive heating elements or by electron beam heating. Typical evaporations have more than one evaporation source, and it is possible to obtain systems with as many as six independent sources. The high temperature produced in these sources cause the vapour pressure of the evaporation rise to a level at which a significant amount of these materials can be collected on a substrate that is located on a direct optical path from the evaporate. The substrate can typically be at a variety of temperatures, ranging from 77 K to approximately 1300 K depending on the required microstructure of the final film. The substrate materials are sapphires Al_2O_3 , MgO, silicon etc.

3.2 Preparation of the Present Samples

The $(\text{La}_{2-x}\text{Nd}_x)(\text{Ba}_{1-y}\text{Ca}_y)\text{Mn}_2\text{O}_7$ samples were synthesized using the solid state reaction method. Powders of La_2O_3 (99.99%), CaCO_3 (99.9%), Nd_2O_3 (99.9%), MnO_2 (99.9%) and BaCO_3 (99.9%) were used as raw materials. Appropriate amounts of required powders were weighed and mixed thoroughly in dry and acetone media for an about 8 hours. La_2O_3 , BaCO_3 , CaCO_3 , MnO_2 , Nd_2O_3 are white powders of molar weights 325.809, 197.349, 100.087, 86.94, 336.48g respectively. The amount of each ingredients required, we calculated. The chemicals were weighed using an

Electronic Digital analytical balance (measuring range 0.0001-210g), weights being shown by LED display. The chemicals were weighed out separately and then well mixed and ground in a ceramic mortar using a pestle for 4 to 6 hours in acetone. The greyish powder thus obtained in the mortar was scraped from its wall and poured into a alumina crucible. The crucible was previously washed with acetone then with distilled water. The crucibles with the powder were then placed in the furnace for calcination purpose.

Table 3.1: List of various polycrystalline $(La_{2-x}Nd_x)(Ba_{1-y}Ca_y)Mn_2O_7$ Samples.

Sample composition	Amount of Raw material	Calcination temperature	Sintering atmosphere
$(La_{1.8}Ba_{0.2})BaMn_2O_7$	$La_2O_3=11.729$, $BaCO_3=9.473$, $MnO_2=6.955$	1100 ^o C	Air
$(La_{1.7}Ba_{0.3})BaMn_2O_7$	$La_2O_3=10.549$, $BaCO_3=9.847$, $MnO_2=5.995$
$(La_{1.6}Ba_{0.4})BaMn_2O_7$	$La_2O_3=9.462$, $BaCO_3=10.623$ $MnO_2=4.576$
$(La_{1.5}Ba_{0.5})BaMn_2O_7$	$La_2O_3=8.826$, $BaCO_3=10.208$, $MnO_2=4.395$
$(La_{1.8}Nd_{0.2})BaMn_2O_7$	$La_2O_3=8.377$, $BaCO_3=5.639$, $MnO_2=4.968$, $Nd_2O_3=0.9613$
$(La_{1.7}Nd_{0.3})BaMn_2O_7$	$La_2O_3=9.825$, $BaCO_3=6.894$, $MnO_2=5.955$, $Nd_2O_3=1.991$
$(La_{1.6}Nd_{0.4})BaMn_2O_7$	$La_2O_3=8.425$, $BaCO_3=7.494$, $MnO_2=6.545$, $Nd_2O_3=2.691$
$(La_{1.5}Nd_{0.5})BaMn_2O_7$	$La_2O_3=8.122$, $BaCO_3=8.494$, $MnO_2=7.255$, $Nd_2O_3=4.037$
$(La_{1.8}Nd_{0.2})(Ba_{0.8}Ca_{0.2})Mn_2O_7$	$La_2O_3=8.377$, $BaCO_3=4.511$, $MnO_2=4.968$, $Nd_2O_3=0.9613$, $CaCO_3=0.571$
$(La_{1.8}Nd_{0.2})(Ba_{0.6}Ca_{0.4})Mn_2O_7$	$La_2O_3=11.749$, $BaCO_3=3.932$, $MnO_2=6.56$, $Nd_2O_3=1.262$, $CaCO_3=1.611$
$(La_{1.8}Nd_{0.2})(Ba_{0.4}Ca_{0.6})Mn_2O_7$	$La_2O_3=12.749$, $BaCO_3=3.432$, $MnO_2=7.56$, $Nd_2O_3=1.462$, $CaCO_3=2.611$
$(La_{1.8}Nd_{0.2})(Ba_{0.2}Ca_{0.8})Mn_2O_7$	$La_2O_3=13.328$, $BaCO_3=1.794$, $MnO_2=7.903$, $Nd_2O_3=1.529$, $CaCO_3=3.639$

3.3 Calcination Schedule

(a) First the powder was heated from room temperature to 1100°C in air. The temperature controller was set at 1100°C for 24 hours. After 24 hours, the furnace was turned off and was allowed to cool to room temperature (Furnace cooling). When room temperature was attained, the resulting chunk was taken out from the furnace and was ground until it became powder.

(b) The procedure (a) was repeated further for three times.

After 72 four hours of total calcination the chunk was ground again until it became fine powder. The product was usually a complete black powder. The resulting black powder is the required powder.

3.4 Preparation of Pellets

A good calcined powder is normally a shining black powder. The calcined powders were then pressed into pellets of 12mm diameter and 1-3 mm thick under a pressure of 12,000 P.S.I. for about 1 to 2 minutes using a hard pressure machine.

3.5 Sintering and Oxidation of the Pellets

The sample $(La_{2-x}Nd_x)(Ba_{1-y}Ca_y)Mn_2O_7$ (For $x=0, 0.1, 0.20$ and $y=0, 0.1, 0.2, 0.3$) pellets were sintered at various temperatures using another high temperature furnace (maximum operating temperature 1700°C) for a fixed time. Sintering was done at 1400°C and 1500°C in air for 5 hours. The temperature ramp was 10°C/minute for both cooling and heating. The pellets thus prepared were used for measurements.

3.6 Construction of a Liquid Nitrogen Cryostat

A liquid nitrogen cryostat is designed for the purpose of low temperature magneto-transport measurements. It is made up of nonmagnetic concentric stainless steel tubes. It consists of two parts (an upper part and a lower part) and each part consists of three concentric tubes of three different dimensions. The outer diameter of

the upper part of the cryostat is 7.6 cm and inner diameter is 3.2 cm. The outer diameter for lower part is 3.8 cm and inner diameter is 3.2 cm. It has three chambers as shown in Figure 3.1. Outer chamber is called vacuum chamber the middle one is cryogen chamber (liquid nitrogen) and the innermost chamber is sample space. Thickness of the wall of each chamber is about 0.2 cm. In the top of the second chamber there are two small pipes connected over the stainless steel plate of upper part of the cryostat, one for inlet of liquid nitrogen and the other for outlet of nitrogen gas. The lower part (20 cm long and 3.8 cm diameter) of the cryostat is shorter and narrower compared to the upper part (85 cm long and 7.6 cm diameter). It is made in such a way that the cryostat can easily move between the pole pieces of the electromagnet. A stainless steel plate connects the lower part and upper part. The top of the upper part is sealed by another stainless steel plate. In the innermost chamber (sample space) there is a sample rod which is made up of stainless steel tube and a flat copper bar. The diameter of the sample rod is chosen in such a manner that it can easily move through the sample space. The top of the sample rod and innermost tubes are air tight connected with a union socket. A carbon glass temperature sensor is used for the measurement of temperature of the sample. It was observed that if the cryostat is filled with liquid nitrogen it takes about 150 minutes to warm up to room temperature.

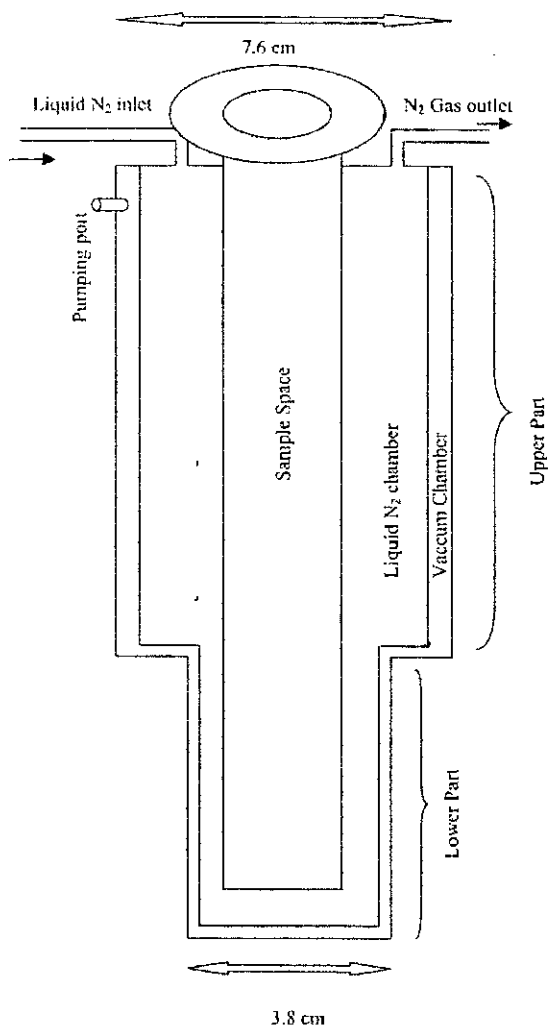


Figure 3.1: Schematic diagram of the liquid nitrogen cryostat.

3.7 Construction of Electromagnet

To study magneto-transport properties of manganese perovskites, we have constructed this electromagnet. Materials play an important role for designing an electromagnet. Normally soft iron with a very low coercive field and low hysteresis is used for the magnet pole pieces. We have used commercial mild steel bar for the body of the electromagnet and soft iron cylindrical rod for pole pieces, which are available in the local market (Dhaka, Bangladesh).

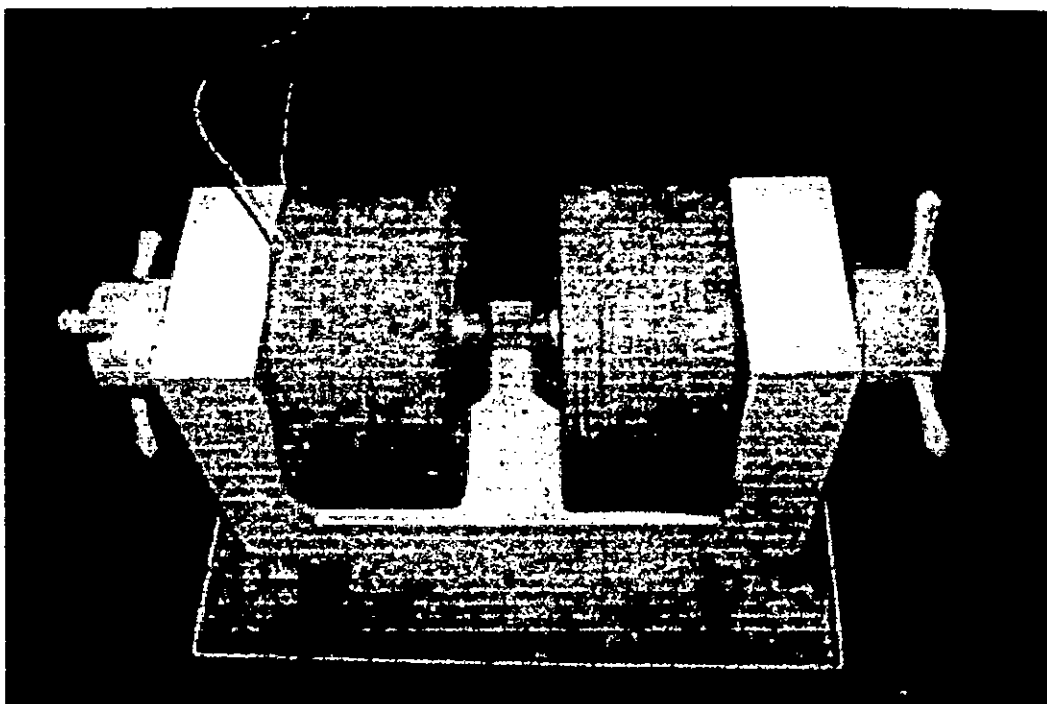


Figure 3.2: Schematic diagram of the Electromagnet.

The major parts of the electromagnets are base, pole piece holder, pole pieces and coils. Base of the electromagnet is made up of a parallelepiped shaped mild steel bar of dimension $36\text{ cm} \times 19\text{ cm} \times 8\text{ cm}$. Pole piece holder of the electromagnet is also made from commercial mild steel bar. Two pole piece holders are attached to both side of the base with L type bolt. Each pole piece holder is a parallelepiped of dimension $32\text{ cm} \times 19\text{ cm} \times 8\text{ cm}$. Pole pieces (cylindrical soft iron of final diameter 9.2 cm) are attached in these holders in such a way so that we can vary the pole gap. The Pole gap may vary from 0-10 cm. As the lower part of our cryostat has outer dimension 3.8 cm, pole gap of this size will be suitable for the magnet operation.

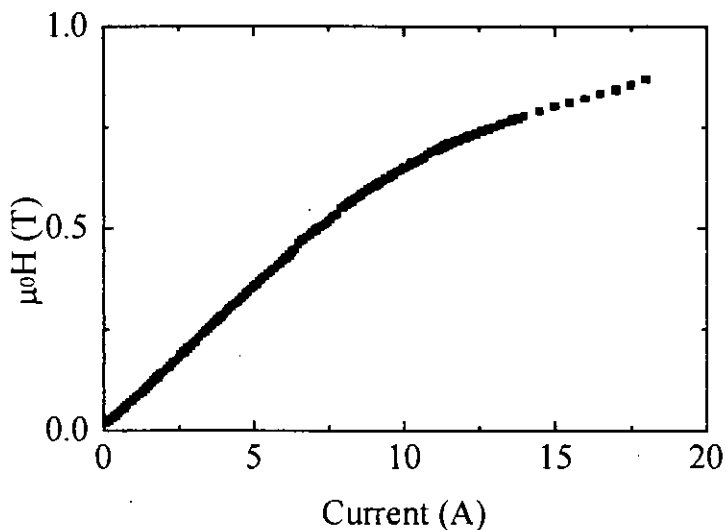


Figure 3.3: Calibration of the home made electromagnet (pole gap 3.8 cm).

Two induction coils for two pole-pieces have been made with insulated copper wire of S. W. G 14. The length of each of the coils is 12 cm. The number of turns in each layer of the coil is 58 and total number of layers is 44. So the total number of turns are 2552. The resistance of each coil is about 8Ω . The weight of each coil is about 40 Kg Two coils are set in the pole pieces of the electromagnet. They are connected in parallel combination with the dc power supply. The calibration of the electromagnet is given in Figure (3.3). A field of 0.86T was obtained for a current of 18A.

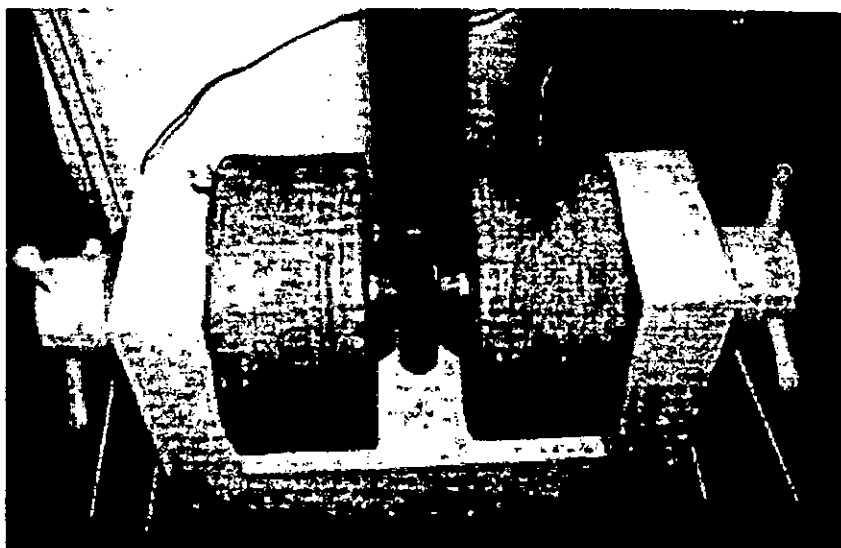


Figure 3.4: Schematic diagram of Magnet and Cryostat Assembly for Magnetoresistance Measurements.

3.8 Construction of the Sample Rod

A sample rod is constructed for four-point resistance measurement. This is a hollow stainless steel tube. The upper part is connected with multi-pin connectors and lower part has a copper sample holder as shown in figure. The sample rod is connected with the cryostat by a union socket. A schematic diagram of the sample rod is shown in figure 3.5.

The carbon glass resistor used as a temperature sensor is kept in close contact with the specimen. For the magnetoresistance measurements we have to apply magnetic field in the sample space. The carbon glass resistor has a very weak sensitivity in the magnetic field.

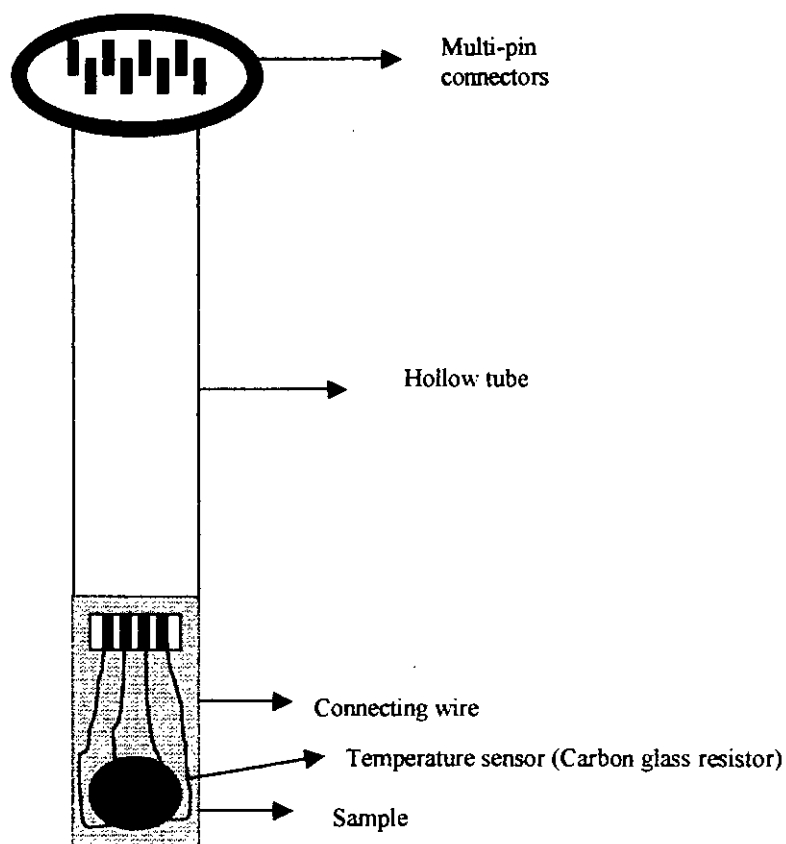


Figure 3.5: Schematic diagram of the sample holder.

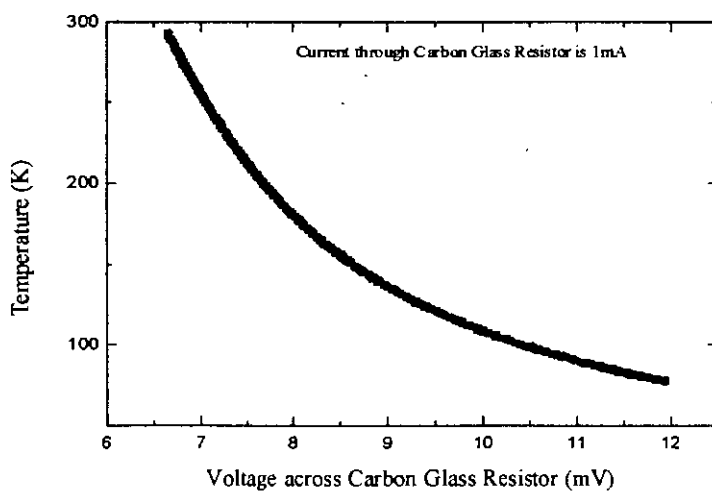


Figure 3.6: Calibration curve of the temperature sensor (Lakeshore Carbon Glass resistor)

3.9 Magnetoresistance Measurement Set-up

Figure 3.7 shows the full view of the cryostat used for magnetoresistance measurements. Figure 3.8 shows the schematic diagram of the Magnetoresistance measurement set up.

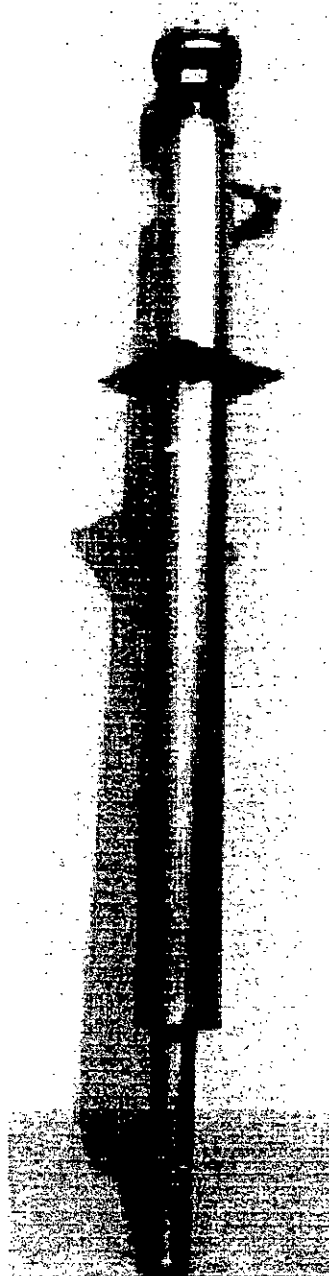


Figure 3.7: A snapshot of the constructed Cryostat

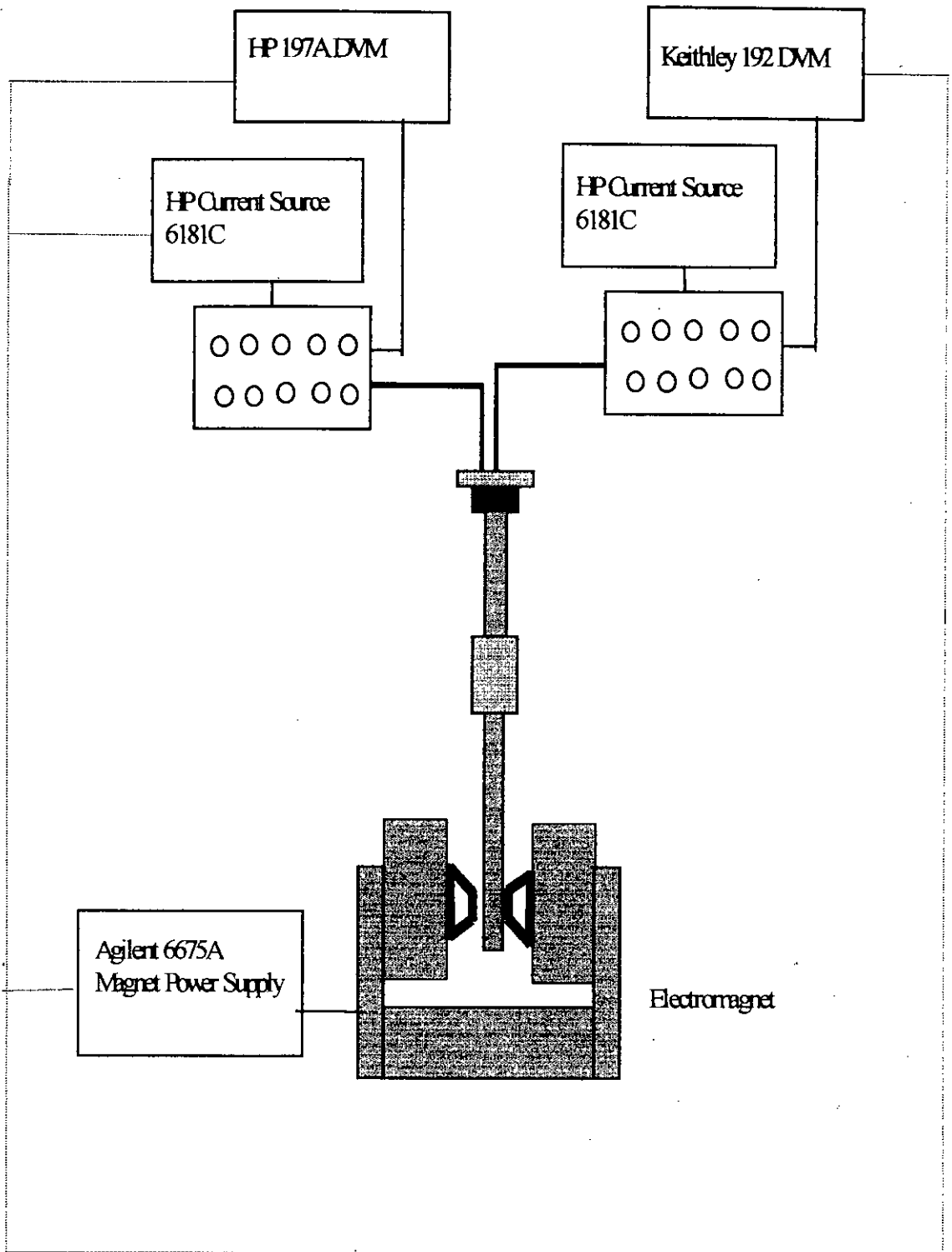


Figure 3.8: Experimental set-up for magnetoresistance measurements.

The standard four probe technique was used for resistance measurements.

All samples for test are mounted on the specimen holder and inserted in the sample well of the cryostat. The temperature of the sample is measured with a calibrated carbon-glass resistor placed close to the sample. The thermometer is powered (1 mA) by a HP 6181C constant current source and voltage is measured with Keithly 192 digital Voltmeter. The sample current is sourced with another 6181C constant current source and voltage drop is measure with HP 197A nanovolt meter.

For magnetoresistance measurements, the electromagnet is powered with Agilent 6675A Power Supply. The magnet is capable of creating a field up to 0.86 T for a current of ≈ 18 A.

3.10 The van der Pauw Technique

The resistivity of our disc shaped samples was calculated using the van der Pauw technique [1,2]. This technique is based on four point measurements providing the following conditions are fulfilled:

- (a) The contacts are on the circumference of the sample.
- (b) The contacts are sufficiently small.
- (c) The sample is homogeneous in thickness.
- (d) The surface of the sample is singly connected, i.e., the sample does not have isolated holes.

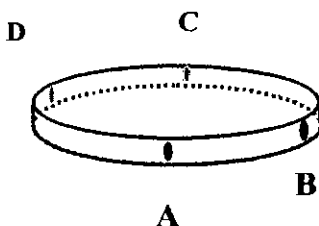


Figure 3.9: The four electrical contacts on the circumference of the disc shaped sample.

Figure 3.9 shows the four contacts on the circumference of the disc shaped sample. For a fixed temperature, we define the resistance $R_{AB,CD}$ as the potential difference

between V_D-V_C between the contacts D and C per unit current through the contacts A and B . The current enters the sample through the contact A and leaves it through the contact B . Similarly, we define $R_{BC,DA}$. Now if the uniform sample thickness is t then according to van der Pauw the $\rho(T)$ will be

$$\rho(T) = \frac{\pi}{\ln 2} \left(\frac{R_{AB,CD} + R_{BC,DA}}{2} \right) f \left(\frac{R_{AB,CD}}{R_{BC,DA}} \right) \quad (3.1)$$

where f is a function of the ratio $R_{AB,CD}/R_{BC,DA}$ only and satisfies the relation

$$\frac{R_{AB,CD} - R_{BC,DA}}{R_{AB,CD} + R_{BC,DA}} = f \operatorname{arccosh} \left\{ \frac{\exp(\ln 2 / f)}{2} \right\}. \quad (3.2)$$

If we assume $\frac{R_{AB,CD}}{R_{BC,DA}} = Q$, then eq. 3.2 becomes

$$\frac{Q-1}{Q+1} = f \operatorname{arccosh} \left\{ \frac{\exp(\ln 2 / f)}{2} \right\}. \quad (3.3)$$

A plot of this function is shown in figure 3.10.

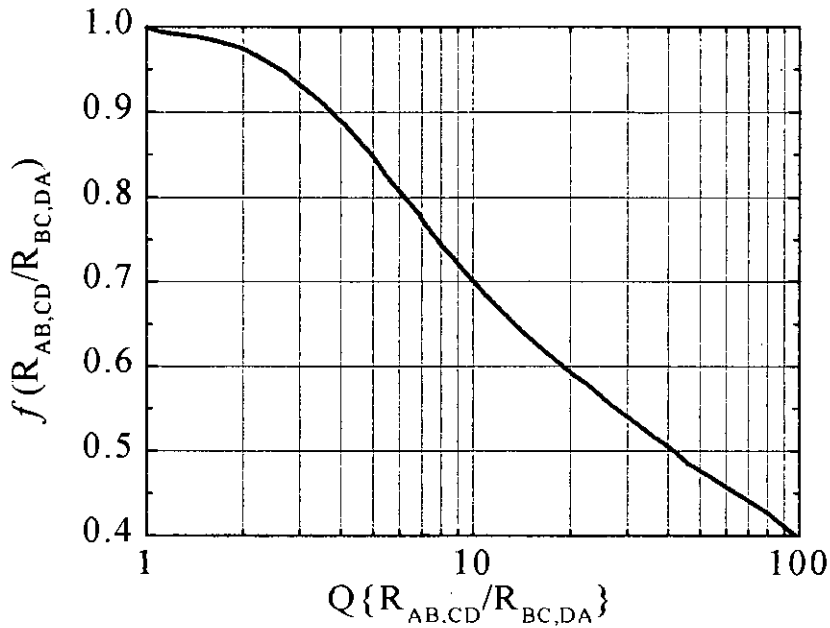


Figure 3.10: The function $f(Q)$ for determining the resistivity of the sample (From ref [3])

In practice the electrical contacts have finite dimensions. van der Pauw showed that if one of the contacts is of finite length l and is assumed that it lies along the circumference of the sample of diameter D then

$$\frac{\Delta\rho}{\rho} \approx \frac{-l^2}{16D^2 \ln 2} \quad (3.4)$$

Also, if all contacts have similar defects the errors introduced are additive. Our sintered disc shaped sample has a diameter $\sim 11\text{mm}$ and if we assume the maximum width dimensions of the contacts are 1 mm then the errors introduced into our measurement due to finite sized contacts will be 0.3%. In fact, we have used 50 μm silver wire and conductive silver paint for the contacts which are much smaller than 1mm.

3.11 Magnetoresistance

The $R(T)$ data was acquired both in zero field and in the presence of field. The $R(T)$ data was converted to $\rho(T)$ using the van der Pauw expression. The magnetoresistance (MR), which is a function of field and temperature, was calculated using the following expression:

$$MR(T, H)\% = -\frac{\rho(T, 0) - \rho(T, H)}{\rho(T, 0)} \times 100 \quad (3.5)$$

Note that according to this definition, the MR can not be more than 100%.

References

- [1] L. J. van der Pauw, "A method of measuring specific resistivity and Hall effects of discs of arbitrary shape," *Philips Research Reports* **13** (1), 1-9 (1958).
- [2] L. J. van der Pauw, "A method of measuring the resistivity and Hall coefficient on lamellae of arbitrary shape," *Philips Technical Review* **20** (8), 220-224 (1958/59).
- [3] Keithley, *Low Level Measurements*, 4th Edition ed. (Keithley Instruments, Inc., 1992).

16566
99591

Chapter 4

Results and Discussion

The polycrystalline $(La_{2-x}Nd_x)(Ba_{1-y}Ca_y)Mn_2O_7$ samples for various x and y values have been studied. All samples were sintered at 1400°C and 1500°C in air atmosphere. The electrical and magnetoresistive properties of various samples were studied.

4.1 Polycrystalline $(La_{2-x}Nd_x)(Ba_{1-y}Ca_y)Mn_2O_7$

The sets of the polycrystalline $(La_{2-x}Nd_x)(Ba_{1-y}Ca_y)Mn_2O_7$ samples were prepared by sintering at 1400°C and 1500°C in air. X-ray diffraction was carried out on the powder samples. Electrical transport and magnetoresistance properties were investigated in these samples. List of various $(La_{2-x}Nd_x)(Ba_{1-y}Ca_y)Mn_2O_7$ samples studied and their sintering conditions are given in Table-4.1.

Table-4.1: Sintering temperature and atmosphere for various $(La_{2-x}Nd_x)(Ba_{1-y}Ca_y)Mn_2O_7$ polycrystalline samples.

Sample composition	Sintering temperature	Sintering temperature	Sintering atmosphere	Sintering time
$(La_{1.8}Ba_{0.2})BaMn_2O_7$	1400°C	1500°C	Air	5 hours
$(La_{1.7}Ba_{0.3})BaMn_2O_7$	''	''	''	''
$(La_{1.6}Ba_{0.4})BaMn_2O_7$	''	''	''	''
$(La_{1.5}Ba_{0.5})BaMn_2O_7$	''	''	''	''
$(La_{1.8}Nd_{0.2})BaMn_2O_7$	''	''	''	''
$(La_{1.7}Nd_{0.3})BaMn_2O_7$	''	''	''	''
$(La_{1.6}Nd_{0.4})BaMn_2O_7$	''	''	''	''
$(La_{1.5}Nd_{0.5})BaMn_2O_7$	''	''	''	''
$(La_{1.8}Nd_{0.2})(Ba_{0.8}Ca_{0.2})Mn_2O_7$	''	''	''	''
$(La_{1.8}Nd_{0.2})(Ba_{0.6}Ca_{0.4})Mn_2O_7$	''	''	''	''
$(La_{1.8}Nd_{0.2})(Ba_{0.4}Ca_{0.6})Mn_2O_7$	''	''	''	''
$(La_{1.8}Nd_{0.2})(Ba_{0.2}Ca_{0.8})Mn_2O_7$	''	''	''	''

4.1.1 X-ray diffraction analysis

In the X-ray analysis the target used was Mo (Zr), target voltage 30KV, current 20mA with scanning speed 1° and chart speed 10mm. The X-ray patterns were taken between 10° - 70° . The X-ray patterns shown in Fig: 4.1, 4.2, & 4.3 show that all samples were single phase within the sensitivity of the X-ray diffraction ray measurement (5%).

Table 4.2 gives the comparative peak position observed for various polycrystalline samples. It is clear from the XRD pattern that all the samples are crystalline and of single phase as there are no detectable impurity peaks.

Table 4.2.1: X-ray peak positions for various $(La_{2-x}Ba_x)BaMn_2O_7$ polycrystalline samples.

Sample Composition	X-ray peak position 2θ (degree)							
	1 st	2 nd	3 rd	4 th	5 th	6 th	7 th	8 th
$(La_{1.8}Ba_{0.2})BaMn_2O_7$	13.5	16.5	18.5	20.3	23.5	27	30	35
$(La_{1.7}Ba_{0.3})BaMn_2O_7$	13.8	16.7	18.7	20.3	23.6	27.1	30.2	33
$(La_{1.6}Ba_{0.4})BaMn_2O_7$	13.5	16.3	18.5	20.3	23.5	27.3	30	33
$(La_{1.5}Ba_{0.5})BaMn_2O_7$	13.5	16.5	18.5	20.3	23.6	27.3	30	32.8

Table 4.2.2 : X-ray peak positions for various $(La_{2-x}Nd_x)BaMn_2O_7$ polycrystalline samples.

Sample Composition	X-ray peak position 2θ (degree)						
	1 st	2 nd	3 rd	4 th	5 th	6 th	7 th
$(La_{1.8}Nd_{0.2})BaMn_2O_7$	16.5	20	22.1	25	27.5	31.5	37
$(La_{1.7}Nd_{0.3})BaMn_2O_7$	16.5	20	22	24.8	26	31.5	35
$(La_{1.6}Nd_{0.4})BaMn_2O_7$	16.5	20	22	25	28	31.6	36
$(La_{1.5}Nd_{0.5})BaMn_2O_7$	16.5	20	22	25	27.5	31.5	37

Table 4.2.3: X-ray peak positions for various $(La_{1.8}Nd_{0.2})(Ba_{1-y}Ca_y)Mn_2O_7$ polycrystalline samples.

Sample Composition	X-ray peak position 2θ (degree)						
	1 st	2 nd	3 rd	4 th	5 th	6 th	7 th
$(La_{1.8}Nd_{0.2})(Ba_{0.8}Ca_{0.2})Mn_2O_7$	15	19.3	22	24.2	27.2	31.5	40
$(La_{1.8}Nd_{0.2})(Ba_{0.6}Ca_{0.4})Mn_2O_7$	15	19.3	22	24.2	27	31.4	39
$(La_{1.8}Nd_{0.2})(Ba_{0.4}Ca_{0.6})Mn_2O_7$	15	19.3	22	24.2	27	31.5	40
$(La_{1.8}Nd_{0.2})(Ba_{0.2}Ca_{0.8})Mn_2O_7$	15	19.3	22	24.2	27	31.5	40

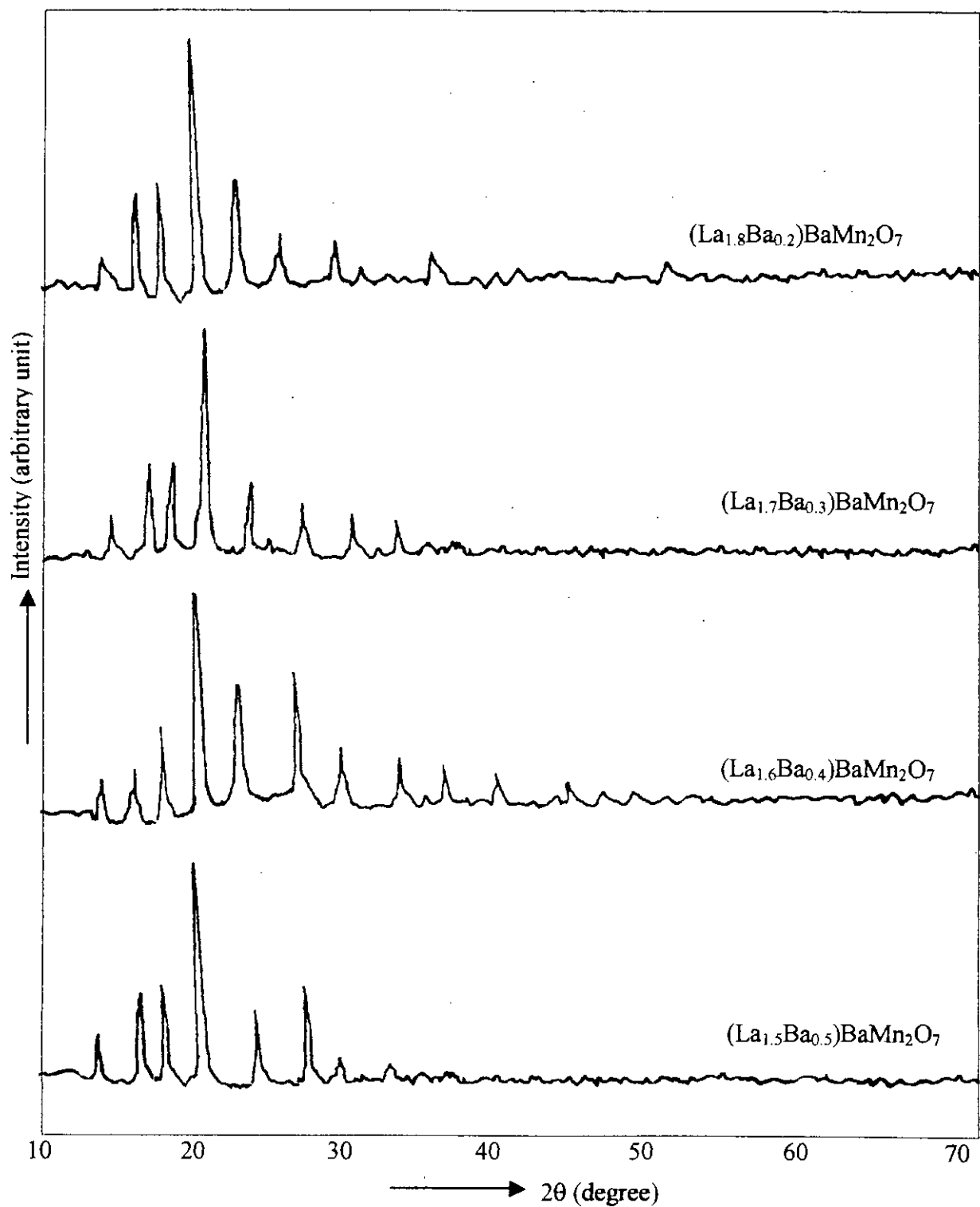


Figure 4.1: The X-ray diffraction pattern for $(La_{2-x}Ba_x)BaMn_2O_7$ polycrystalline samples.

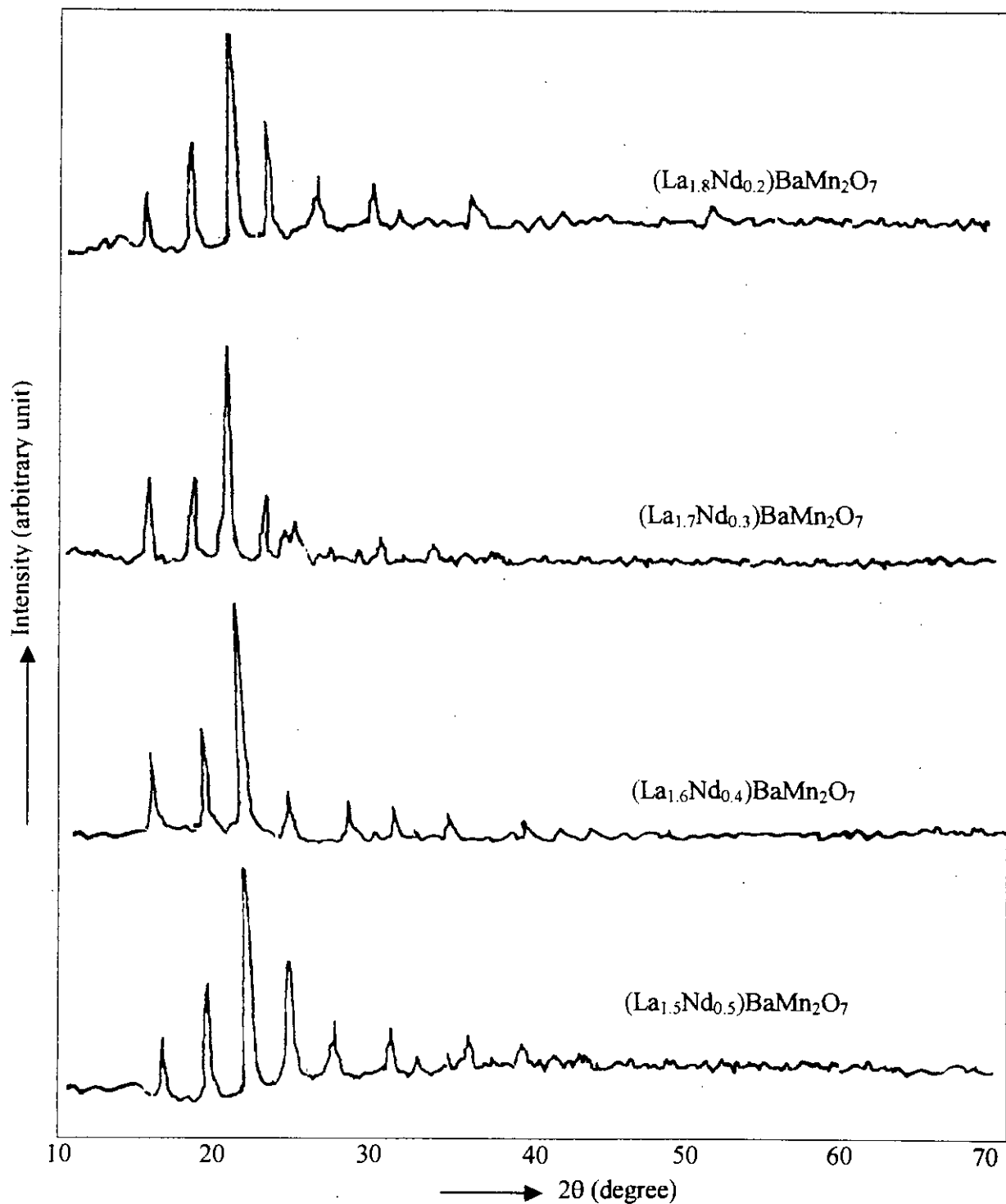


Figure 4.2: The X-ray diffraction pattern for $(La_{2-x}Nd_x)BaMn_2O_7$ polycrystalline samples.

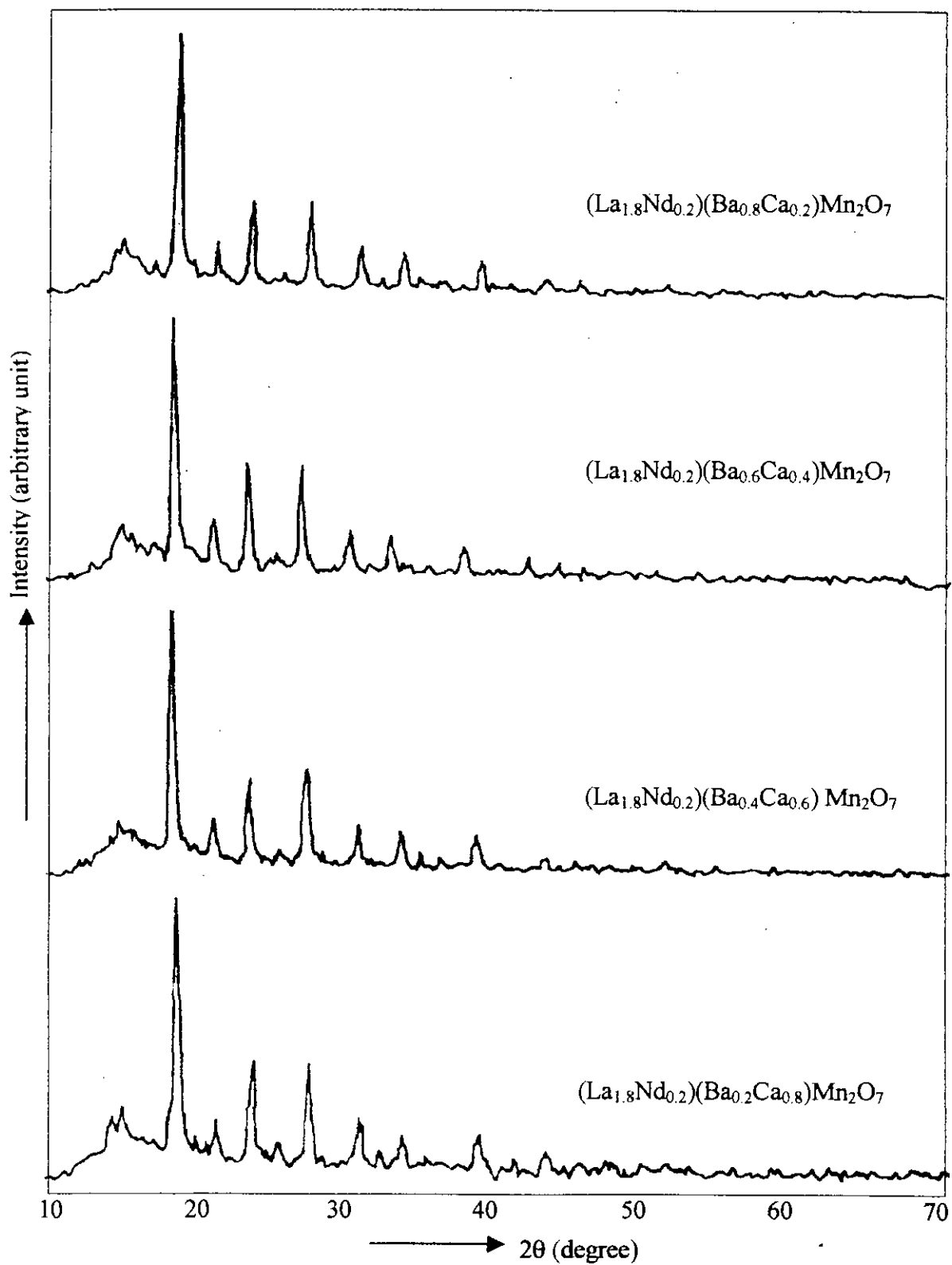


Figure 4.3: The X-ray diffraction pattern for $(\text{La}_{1.8}\text{Nd}_{0.2})(\text{Ba}_{1-y}\text{Ca}_y)\text{Mn}_2\text{O}_7$ polycrystalline samples.

4.2 Microstructures of $(La_{2-x}Nd_x)(Ba_{1-y}Ca_y)Mn_2O_7$

The scanning electron microscopy (SEM) microstructures of the samples of different compositions were examined by using SEM. Micrograph of the samples shows that the substitution of La by Ba (fig 4.4) or Nd (fig 4.5 and 4.6) does not disturb the homogeneity of the samples but the addition of Nd instead of Ba, the grain size of the samples get decreased. A drastic change is observed when the Ca is substituted in the Ba site (fig 4.7). The honey comb type surface observed does seem to have effect in the electrical properties of the samples.

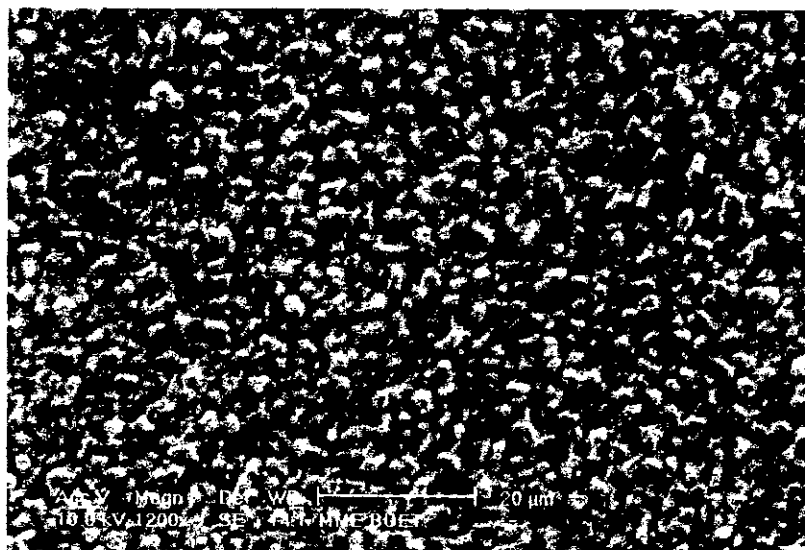


Figure 4.4: SEM micrograph of $(La_{1.8}Ba_{0.2})BaMn_2O_7$ polycrystalline sample sintered at $1400^{\circ}C$.

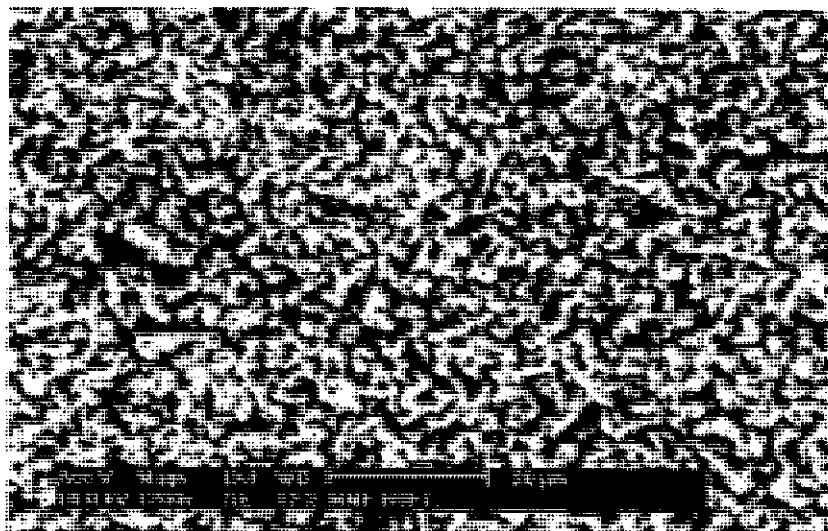


Figure 4.5: SEM micrograph of (La_{1.8}Nd_{0.2})BaMn₂O₇ polycrystalline sample sintered at 1400°C.

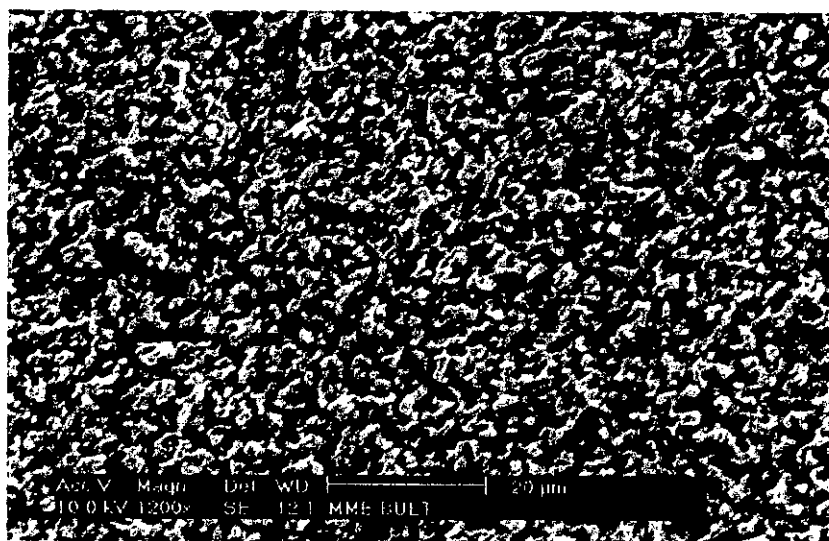


Figure 4.6: SEM micrograph of (La_{1.7}Nd_{0.3})BaMn₂O₇ polycrystalline sample sintered at 1400°C.

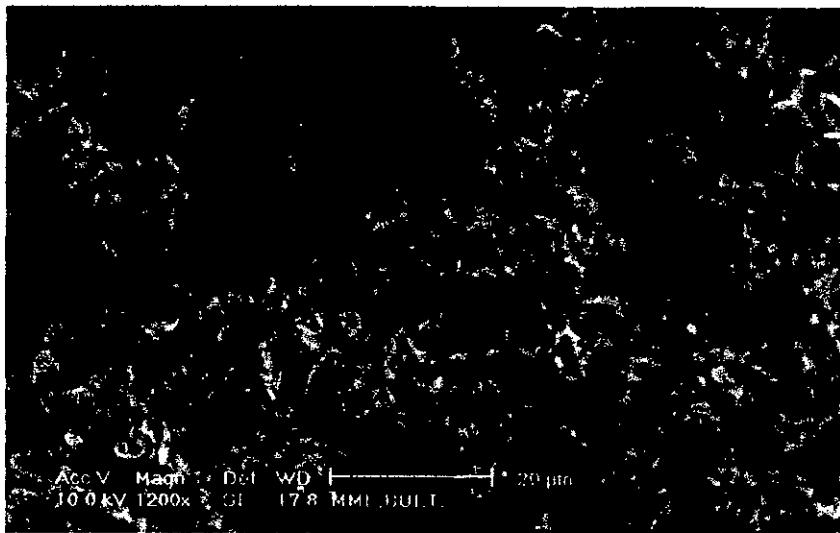


Figure 4.7: SEM micrograph of $(\text{La}_{1.8}\text{Nd}_{0.2})(\text{Ba}_{1-y}\text{Ca}_y)\text{Mn}_2\text{O}_7$ polycrystalline sample sintered at 1400°C .

4.3 DC Electrical Resistivity

The DC electrical resistivity for various $(La_{2-x}Nd_x)(Ba_{1-y}Ca_y)Mn_2O_7$ polycrystalline samples was measured by using standard four point probe method from room temperature (RT) down to liquid nitrogen temperature ($77K$). In magnetoresistance measurements, DC magnetic field was applied perpendicularly to the surface of the samples.

4.3.1 DC Electrical Resistivity of $(La_{2-x}Ba_x)BaMn_2O_7$

The temperature dependence of normalised resistivity, $\rho(T)/\rho(RT)$, where RT is room temperature, at zero applied magnetic field for various $(La_{2-x}Ba_x)BaMn_2O_7$ polycrystalline samples sintered at $1400^{\circ}C$ and $1500^{\circ}C$ in air are shown in Figures-4.8 and 4.9 respectively. Figures-4.10 and 4.11 show the corresponding behavior of the samples in presence of $0.65T$ applied magnetic field. As shown in Figures-4.8, 4.9, 4.10 and 4.11, it is evident that all the samples show a metal insulator ($M-I$) transition and this $M-I$ transition occur at temperature T_p . The $M-I$ transition temperature increases with the increase of Ba concentration up to $x=0.4$. Beyond $x=0.4$ of Ba concentration, the transition temperature decrease slightly. This may be due to the interaction mechanism between the manganese ions that occur via oxygen ions. Exchange coupling mechanism in the manganites are believed to be as follow, nature of the couplings [1,2] are i) ferromagnetic when the interaction is in between Mn^{3+} and Mn^{4+} ions, ii) anti-ferromagnetic behavior arises for interaction between Mn^{4+} ions iii) ferromagnetic or anti-ferromagnetic behavior for interactions between Mn^{3+} ions. The charge neutrality in $(La_{2-x}Ba_x)BaMn_2O_7$ is attained with the charge configuration of the constituent element as $La_2^{3+}Ba^{2+}Mn_2^{3+}O_7^{2-}$. When La is substituted by Ba, the valance state of some Mn^{3+} ions change to Mn^{4+} ions. So the increase of transition temperature with increase of Ba concentration up to $x=0.4$ is most probably due to the coupling between Mn^{3+} and Ba^{2+} favoring ferromagnetic. The decrease of transition temperature for beyond $x=0.4$ of Ba, is probably due to the anti-ferromagnetic coupling between Mn^{3+} and Ba^{2+} ions. Besides, the larger atomic diameter of Ba compared to La may be a added factor.

From the observation of $\rho(T)/\rho(RT)$ curves for $H=0$ and $H=0.65T$, it is observed that the transition temperature is higher for $H=0.65T$. This is believed to be due to the suppression of spin fluctuation with the applied magnetic field in the paramagnetic region and hence the applied magnetic field accelerate magnetic ordering [3,4] which causes the transition temperature enhance by few Kelvin. It is also observed that as the sintering temperature increase, resistivity of the samples decrease throughout the measured temperature range. This is probably due to the decrease of pores and the increase of grain size of the samples, which result in the decrease in the grain boundary and hence decrease in resistivity of the samples. The results of T_p 's are summarised in Table 4.3 and the T_p 's vary from 230.56 K to 249 K.

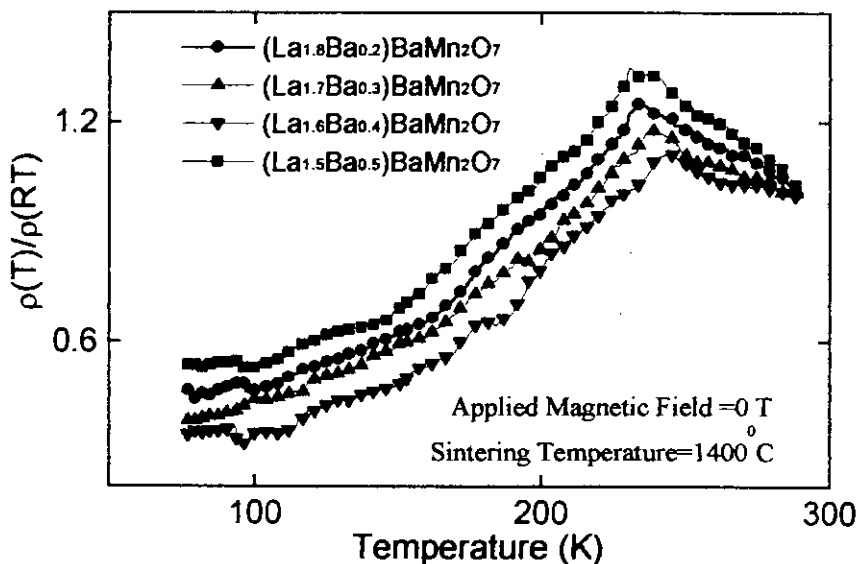


Figure 4.8: The zero field normalised resistivity as a function of temperature for various $(La_{2-x}Ba_x)BaMn_2O_7$ polycrystalline samples sintered at $1400^{\circ}C$ in air.

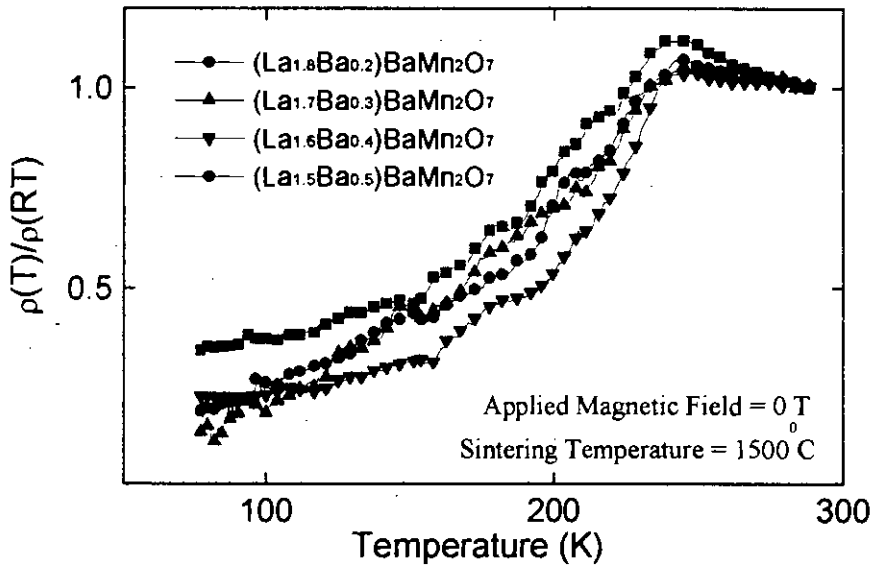


Figure 4.9: The zero field normalised resistivity as a function of temperature for various $(La_{2-x}Ba_x)BaMn_2O_7$ polycrystalline samples sintered at $1500^{\circ}C$ in air.

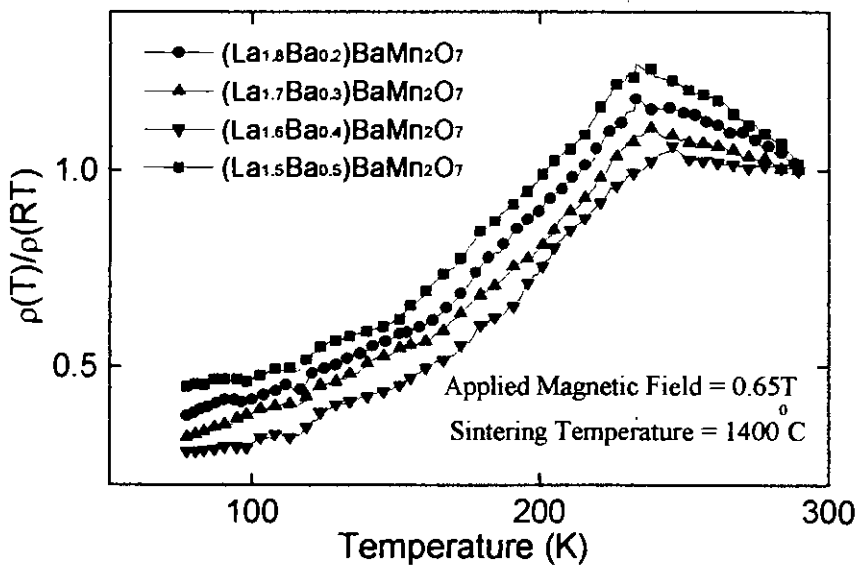


Figure 4.10 : The normalised resistivity with constant magnetic field 0.65T as a function of temperature for various $(La_{2-x}Ba_x)BaMn_2O_7$ polycrystalline samples sintered at $1400^{\circ}C$ in air.

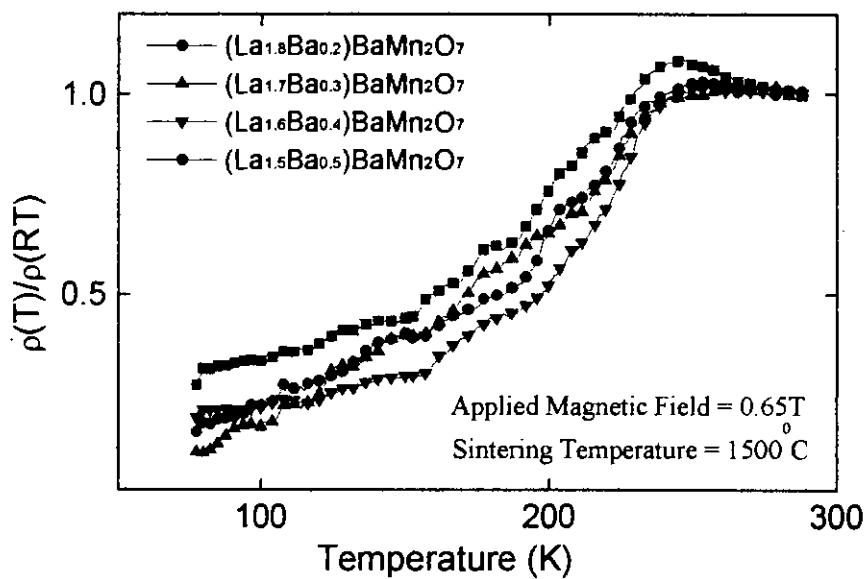


Figure 4.11 : The normalised resistivity with constant magnetic field 0.65T as a function of temperature for various $(La_{2-x}Ba_x)BaMn_2O_7$ polycrystalline samples sintered at $1500^{\circ}C$ in air.

Table 4.3 : The metal-insulator transition temperatures T_p for $H=0T$ and $H=0.65T$ for various $(La_{2-x}Ba_x)BaMn_2O_7$ polycrystalline samples.

Sample Composition	Sintering Condition	T_p (K)	T_p (K)
		$H=0$ T	$H=0.65$ T
$(La_{1.8}Ba_{0.2})BaMn_2O_7$	$1400^{\circ}C$	233.7	236.1
$(La_{1.7}Ba_{0.3})BaMn_2O_7$		238	240
$(La_{1.6}Ba_{0.4})BaMn_2O_7$		245	247.3
$(La_{1.5}Ba_{0.5})BaMn_2O_7$		230.56	238
$(La_{1.8}Ba_{0.2})BaMn_2O_7$	$1500^{\circ}C$	242.2	249
$(La_{1.7}Ba_{0.3})BaMn_2O_7$		243.9	246
$(La_{1.6}Ba_{0.4})BaMn_2O_7$		241	245
$(La_{1.5}Ba_{0.5})BaMn_2O_7$		240.7	243.2

4.3.2 DC Electrical Resistivity of $(La_{2-x}Nd_x)BaMn_2O_7$

The temperature dependence of normalised resistivity, $\rho(T)/\rho(RT)$, where RT is room temperature, at zero applied magnetic field for various $(La_{2-x}Nd_x)BaMn_2O_7$ polycrystalline samples sintered at 1400°C and 1500°C in air are shown in Figures-4.12 and 4.13 respectively. Figures-4.14 and 4.15 show the corresponding behavior of the samples in presence of 0.65T applied magnetic field. As shown in Figures- 4.12, 4.13, 4.14, and 4.15, it is evident that all the samples show a metal insulator ($M-I$) transition and this $M-I$ transition occur at temperature T_p . The $M-I$ transition temperature increase with the increase of Nd concentration. This may be due to the interaction mechanism between the manganese ions that occur via oxygen ions. Since the $M-I$ transition temperature is related to the Mn-O-Mn angle and the Mn-Mn transfer integral [7]. The $M-I$ transition temperature is changed by bending the Mn-O-Mn angle [8-11]. As the atomic diameter of Nd is smaller than that of La, so substitution of La by Nd favoring of changing the bond angle between Mn-O-Mn ions, there by the $M-I$ transition temperature is increased with the increase of Nd concentration.

From the observation of $\rho(T)/\rho(RT)$ curves for $H=0$ and $H=0.65\text{T}$, it is observed that the transition temperature is higher for $H=0.65\text{T}$. This is believed to be due to the suppression of spin fluctuation with the applied field in the paramagnetic region and hence the applied magnetic field accelerate magnetic ordering [3,4] which causes the transition temperature enhance by few Kelvin. It is also observed that as the sintering temperature increase, resistivity of the samples decrease throughout the measured temperature range. This is probably due to the decrease of pores and the increase of grain size of the samples, which result in the decrease in the grain boundary and hence decrease in resistivity of the samples. The results of T_p 's are summarised in Table 4.4 and the T_p 's vary from 245 K to 260.4 K .

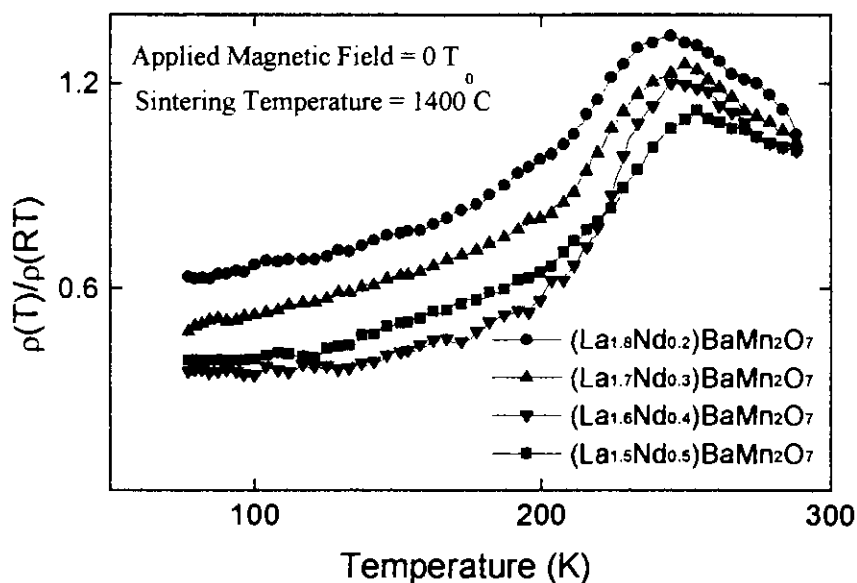


Figure 4.12 : The zero field normalised resistivity as a function of temperature for various $(La_{2-x}Nd_x)BaMn_2O_7$ polycrystalline samples sintered at 1400°C in air.

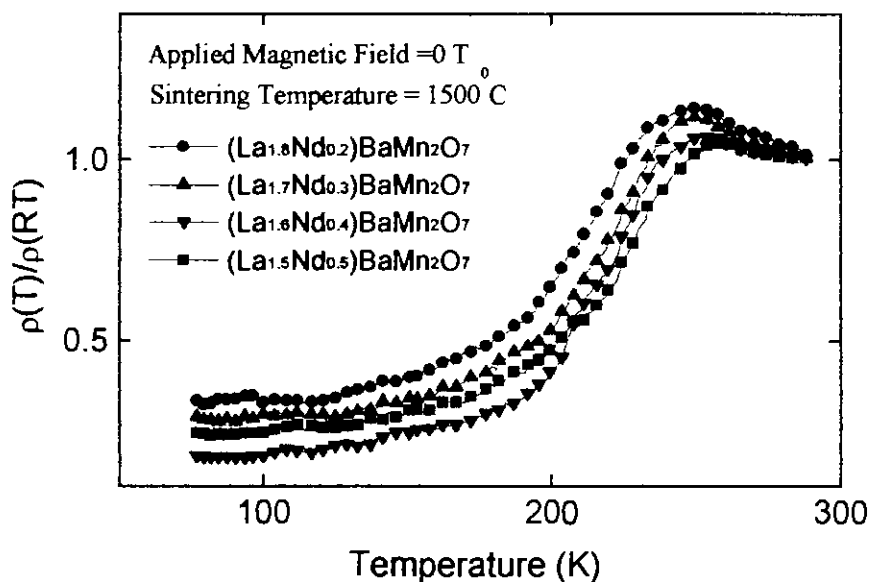


Figure 4.13 : The zero field normalised resistivity as a function of temperature for various $(La_{2-x}Nd_x)BaMn_2O_7$ polycrystalline samples sintered at 1500°C in air.

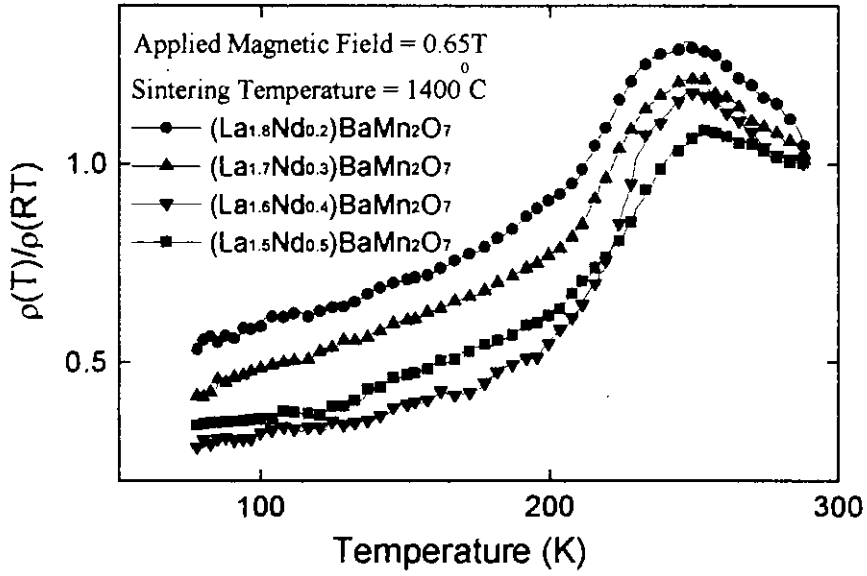


Figure 4.14 : The normalised resistivity with constant magnetic field 0.65T as a function of temperature for various $(\text{La}_{2-x}\text{Nd}_x)\text{BaMn}_2\text{O}_7$ polycrystalline samples sintered at 1400°C in air.

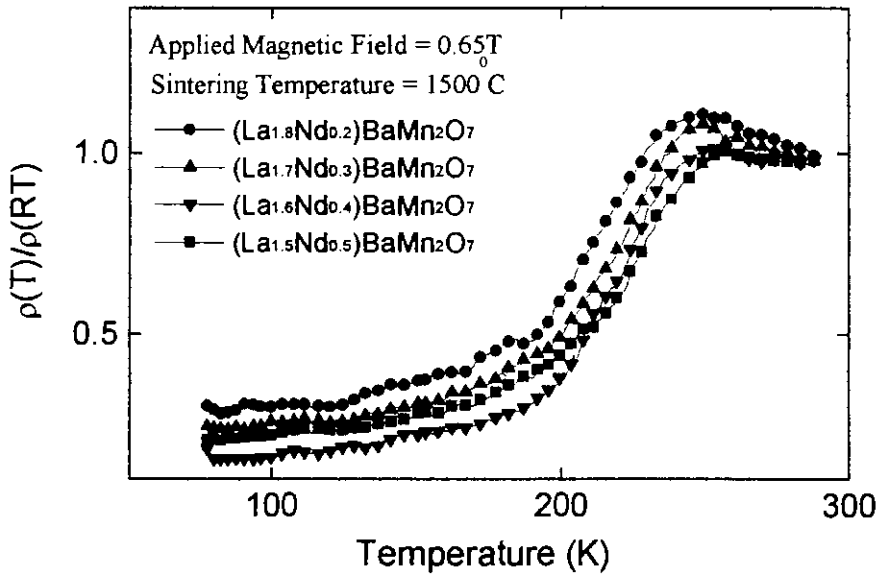


Figure 4.15 : The normalised resistivity with constant magnetic field 0.65T as a function of temperature for various $(\text{La}_{2-x}\text{Nd}_x)\text{BaMn}_2\text{O}_7$ polycrystalline samples sintered at 1500°C in air.

Table 4.4 : The metal-insulator transition temperatures T_p for $H=0T$ and $H=0.65T$ for various $(La_{2-x}Nd_x)BaMn_2O_7$ polycrystalline samples.

Sample Composition	Sintering Condition	T_p (K)	T_p (K)
		H=0 T	H=0.65 T
$(La_{1.8}Nd_{0.2})BaMn_2O_7$	1400 ⁰ C	246	248.2
$(La_{1.7}Nd_{0.3})BaMn_2O_7$		250	253
$(La_{1.6}Nd_{0.4})BaMn_2O_7$		245	250
$(La_{1.5}Nd_{0.5})BaMn_2O_7$		254	255
$(La_{1.8}Nd_{0.2})BaMn_2O_7$	1500 ⁰ C	249	251.3
$(La_{1.7}Nd_{0.3})BaMn_2O_7$		251	253.2
$(La_{1.6}Nd_{0.4})BaMn_2O_7$		252	254
$(La_{1.5}Nd_{0.5})BaMn_2O_7$		258	260.4

4.3.3 DC Electrical Resistivity of $(La_{1.8}Nd_{0.2})(Ba_{1-y}Ca_y)Mn_2O_7$

The temperature dependence of normalised resistivity, $\rho(T)/\rho(RT)$, where RT is room temperature, at zero applied magnetic field for various $(La_{1.8}Nd_{0.2})(Ba_{1-y}Ca_y)Mn_2O_7$ polycrystalline samples sintered at 1400⁰C and 1500⁰C in air are shown in Figures-4.16 and 4.17 respectively. Figures-4.18 and 4.19 show the corresponding behavior of the samples in presence of applied magnetic field of 0.65T. As shown in Figures-4.16, 4.17, 4.18, and 4.19, it is evident that for $y=0.2$ & 0.4, the samples exhibit a metal-insulator ($M-I$) transition but for $y=0.6$ & 0.8, the samples show an antiferromagnetic insulator behavior. This may be due to, when Ba is substituted by Ca seem to enhance the insulator phase. This means, the electron transfer between the manganese site via Oxygen is hampered.

From the observation of $\rho(T)/\rho(RT)$ curves for $H=0$ and $H=0.65T$, it is seen that the transition temperature is higher for $H=0.65T$. This is believed to be due to the suppression of spin fluctuation with the applied field in the paramagnetic region and hence the applied magnetic field accelerate magnetic ordering [3,4] which causes the transition temperature enhance by few Kelvin. It is also observed that as the sintering

temperature increase resistivity of the samples decreases throughout the measured temperature range. This is probably due to the decrease of pores and the increase of grain size of the samples, which result in the decrease in the grain boundary and hence decrease in resistivity of the samples. The results of T_p 's are summarised in Table 4.5.

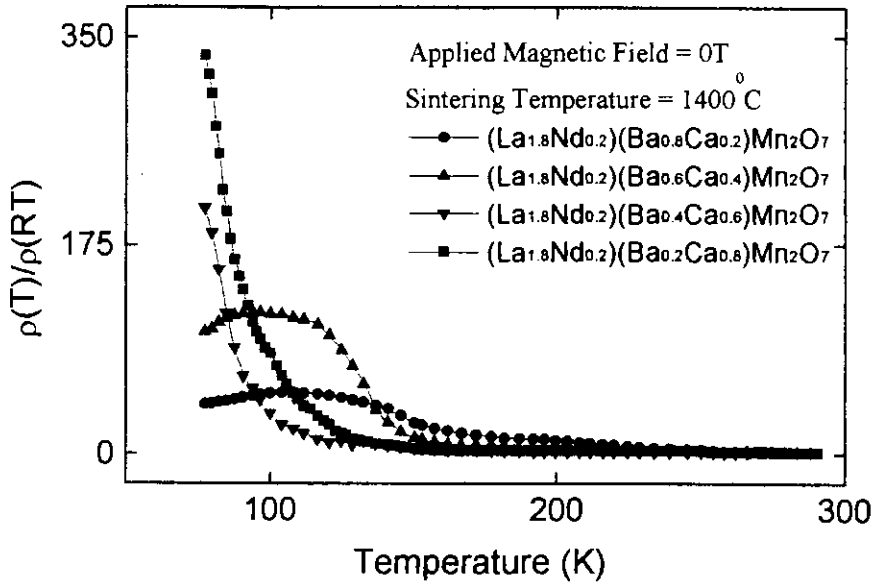


Figure 4.16 : The zero field normalised resistivity as a function of temperature for various $(La_{2-x}Nd_x)(Ba_{1-y}Ca_y)Mn_2O_7$ polycrystalline samples sintered at 1400°C in air.

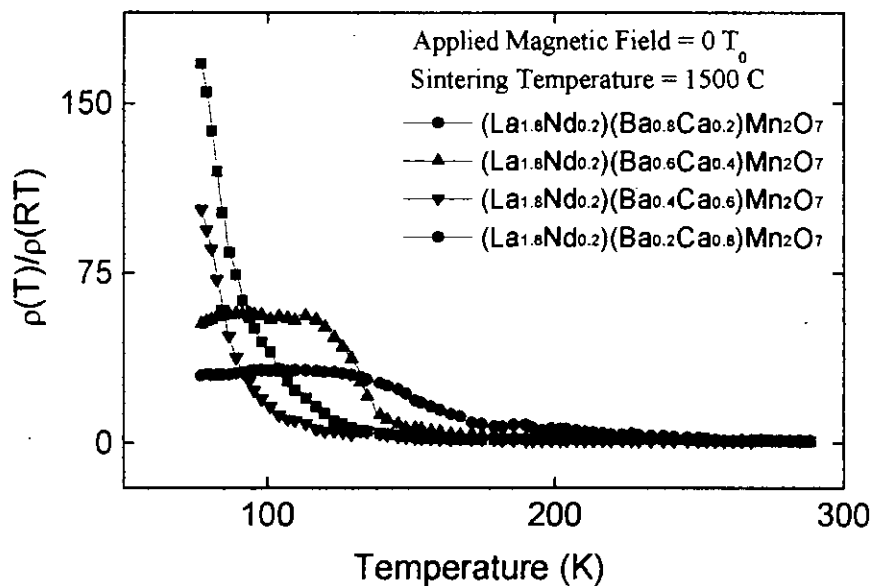


Figure 4.17 : The zero field normalised resistivity as a function of temperature for various (La_{2-x}Nd_x)(Ba_{1-y}Ca_y)Mn₂O₇ polycrystalline samples sintered at 1500^oC in air.

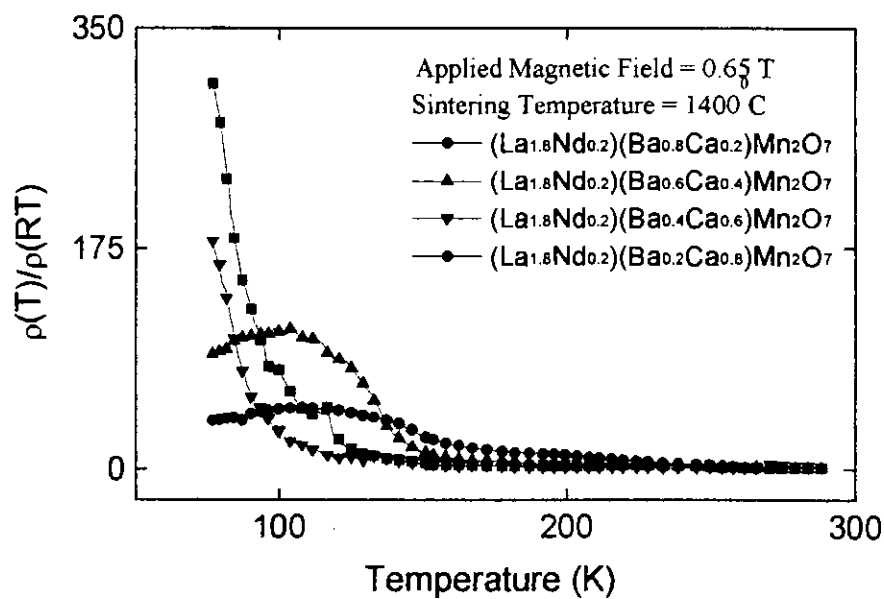


Figure 4.18: The normalised resistivity with constant magnetic field 0.65T as a function of temperature for various (La_{2-x}Nd_x)(Ba_{1-y}Ca_y)Mn₂O₇ polycrystalline samples sintered at 1400^oC in air.

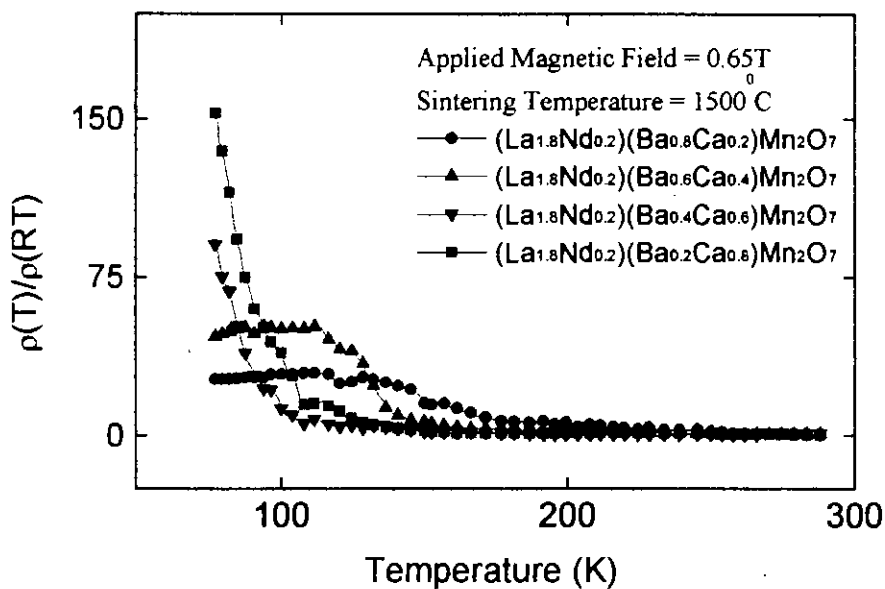


Figure 4.19 : The normalised resistivity with constant magnetic field 0.65T as a function of temperature for various $(\text{La}_{2-x}\text{Nd}_x)(\text{Ba}_{1-y}\text{Ca}_y)\text{Mn}_2\text{O}_7$ polycrystalline samples sintered at 1500°C in air.

Table 4.5 : The metal-insulator transition temperatures T_p for $H=0\text{T}$ and $H=0.65\text{T}$ for various $(\text{La}_{2-x}\text{Nd}_x)(\text{Ba}_{1-y}\text{Ca}_y)\text{Mn}_2\text{O}_7$ polycrystalline samples.

Sample Composition	Sintering Condition	T_p (K)	
		$H=0$ T	$H=0.65$ T
$(\text{La}_{1.8}\text{Nd}_{0.2})(\text{Ba}_{0.8}\text{Ca}_{0.2})\text{Mn}_2\text{O}_7$	1400°C	112	116
$(\text{La}_{1.8}\text{Nd}_{0.2})(\text{Ba}_{0.6}\text{Ca}_{0.4})\text{Mn}_2\text{O}_7$		97	103
$(\text{La}_{1.8}\text{Nd}_{0.2})(\text{Ba}_{0.4}\text{Ca}_{0.6})\text{Mn}_2\text{O}_7$		-	-
$(\text{La}_{1.8}\text{Nd}_{0.2})(\text{Ba}_{0.2}\text{Ca}_{0.8})\text{Mn}_2\text{O}_7$		-	-
$(\text{La}_{1.8}\text{Nd}_{0.2})(\text{Ba}_{0.8}\text{Ca}_{0.2})\text{Mn}_2\text{O}_7$	1500°C	121	128
$(\text{La}_{1.8}\text{Nd}_{0.2})(\text{Ba}_{0.6}\text{Ca}_{0.4})\text{Mn}_2\text{O}_7$		103	111
$(\text{La}_{1.8}\text{Nd}_{0.2})(\text{Ba}_{0.4}\text{Ca}_{0.6})\text{Mn}_2\text{O}_7$		-	-
$(\text{La}_{1.8}\text{Nd}_{0.2})(\text{Ba}_{0.2}\text{Ca}_{0.8})\text{Mn}_2\text{O}_7$		-	-

4.4 Magnetoresistance

The magnetoresistance (MR) as a function of temperature and applied magnetic field of the samples was measured at room temperature and liquid nitrogen temperature.

The MR was calculated using following formula :

$$MR(T, H)\% = -\frac{\rho(T, 0) - \rho(T, H)}{\rho(T, 0)} \times 100$$

For the magnetoresistance measurement, the magnetic field was applied perpendicularly to the surface of the samples.

4.5.1 Magnetoresistance of $(La_{2-x}Ba_x)BaMn_2O_7$

4.5.1.1 $MR(T)$ for $(La_{2-x}Ba_x)BaMn_2O_7$

The MR as a function of temperature for $(La_{2-x}Ba_x)BaMn_2O_7$ polycrystalline samples is shown in Figure-4.20 and Figure-4.21. In these figures, we have shown $MR(T)$ of $(La_{2-x}Ba_x)BaMn_2O_7$ polycrystalline samples sintered at 1400°C and 1500°C . The $MR(T)$ curve was taken in presence of 0.65T applied magnetic field. It is found that the samples show intrinsic peak MR and also extrinsic low temperature MR . The peak temperature of $MR(T)$ is higher than that of the T_p observed in the $\rho(T)/\rho(RT)$ curves. This is because, the presence of magnetic field accelerate the $M-I$ transition, as a result $M-I$ transition occurs at some elevated temperature. The intrinsic MR is found in this manganite due to the fact that for these samples, $M-I$ transition is accompanied with the ferromagnetic to paramagnetic transition [3,4]. The extrinsic MR observe at low temperature for this polycrystalline samples is due to the grain boundaries. This type of extrinsic MR is not present for single crystal manganite [5].

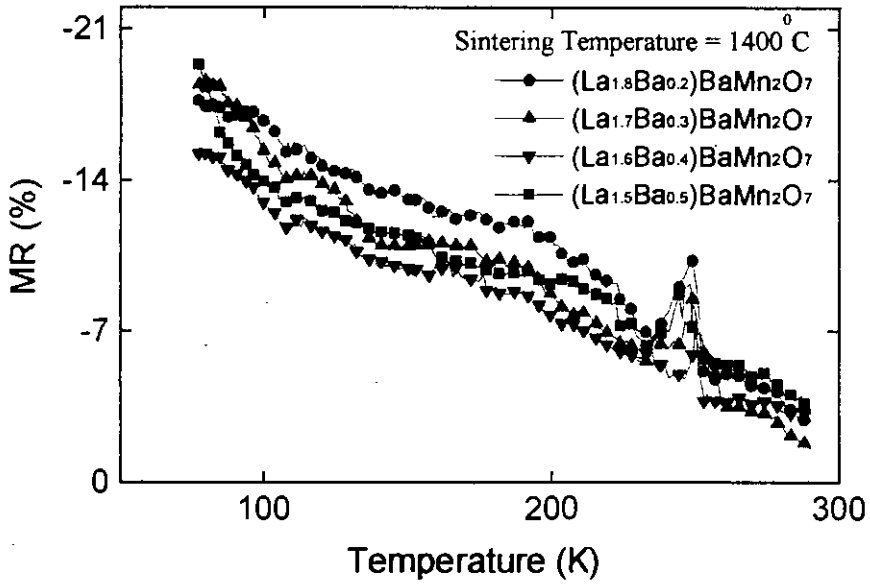


Figure 4.20 : MR as a function of temperature for various $(La_{2-x}Ba_x)BaMn_2O_7$ polycrystalline samples sintered at 1400°C in air.

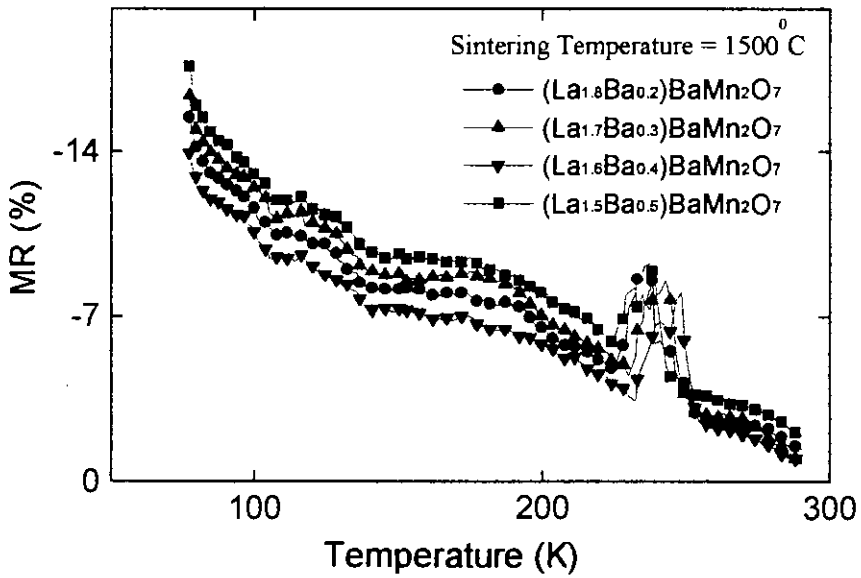


Figure 4.21: MR as a function of temperature for various $(La_{2-x}Ba_x)BaMn_2O_7$ polycrystalline samples sintered at 1500°C in air.

4.5.1.2 MR (H) for $(La_{2-x}Ba_x)BaMn_2O_7$

The magnetoresistance (MR) as a function of magnetic field for various $(La_{2-x}Ba_x)BaMn_2O_7$ samples sintered at 1400°C and 1500°C was measured at room temperature and at 77K . Figure 4.22 and Figure-4.23 show the MR as a function of magnetic field at room temperature. The observed MR is very low with a maximum value of 3.25% and is almost linear with the applied field as show in Figures 4.22 and 4.23. This linear increase of MR is due to the suppression of spin fluctuations with the applied field. The results of MR curves are summarised in Table 4.6.

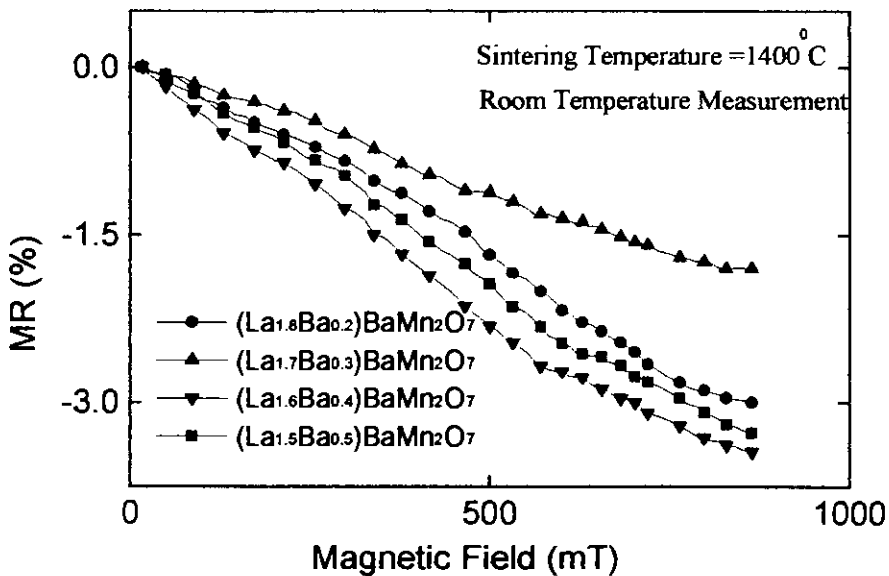


Figure 4.22 : MR as a function of magnetic field at room temperature for various $(La_{2-x}Ba_x)BaMn_2O_7$ polycrystalline samples sintered at 1400°C in air.

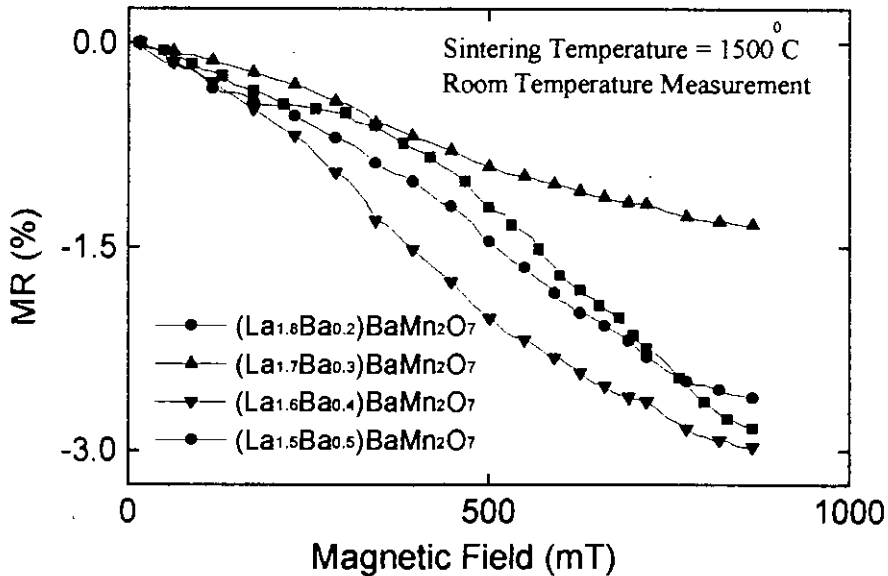


Figure 4.23 : MR as a function of magnetic field at room temperature for various $(\text{La}_{2-x}\text{Ba}_x)\text{BaMn}_2\text{O}_7$ polycrystalline samples sintered at 1500°C in air.

The MR at 77K for the samples sintered at 1400°C and 1500°C are shown in Figure 4.24 and Figure 4.25 respectively. From these figures, it is observed that, all samples exhibit MR with a maximum value about 20% at 77K . The MR in these polycrystalline samples exhibit two distinct regimes as a function of magnetic field. Highly sensitive low field MR is observed up to an applied magnetic field H^* (indicated in the graph). For these $(\text{La}_{2-x}\text{Ba}_x)\text{BaMn}_2\text{O}_7$ polycrystalline samples $H^* \approx 0.167\text{ T}$ and about 14% MR is seen at H^* at 77K . For $H < H^*$, the MR changes rapidly with H followed by a gradual change as H is increased further. Beyond H^* , MR has a weak function of the applied magnetic field. This may be due to the reason that as the material is subdivided into domains, low field is quite sufficient to align the domains spins and thus a sharp decrease in MR is observed but to align the spins at the domain boundary requires much larger field leading to a weak field dependence. The results of % MR curve are summarised in Table 4.6.

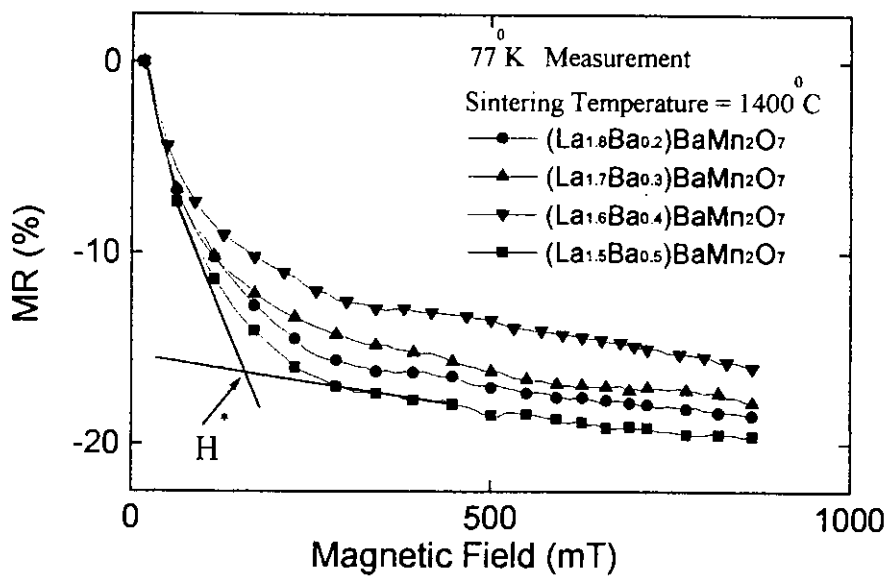


Figure 4.24 : MR as a function of magnetic field at 77K for various $(La_{2-x}Ba_x)BaMn_2O_7$ polycrystalline samples sintered at 1400^oC in air.

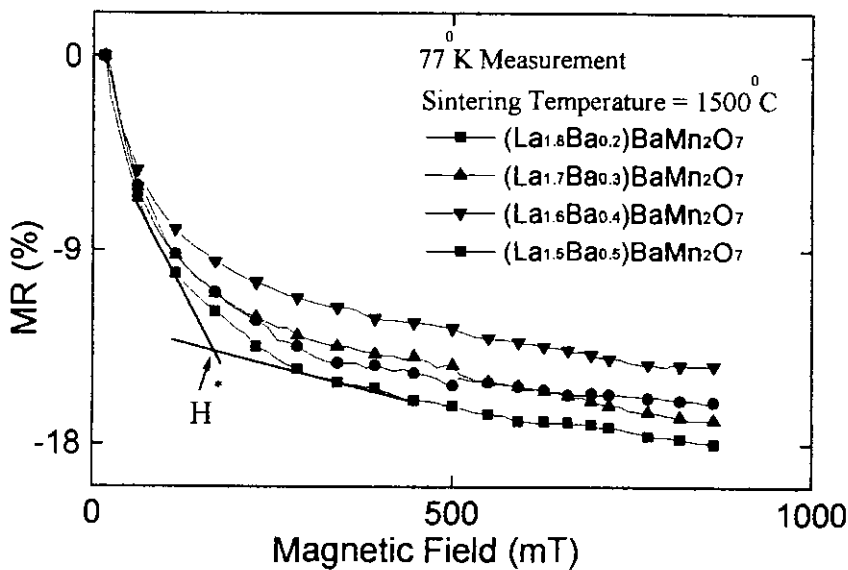


Figure 4.25 : MR as a function of magnetic field at 77K for various $(La_{2-x}Ba_x)BaMn_2O_7$ polycrystalline samples sintered at 1500^oC in air.

Table 4.6 : The % MR curve for various $(La_{2-x}Ba_x)BaMn_2O_7$ polycrystalline samples.

Sample Composition	Sintering Condition	%MR at room temperature	%MR at 77K
$(La_{1.8}Ba_{0.2})BaMn_2O_7$	1400 ^o C	2.92	18.64
$(La_{1.7}Ba_{0.3})BaMn_2O_7$		1.55	17.80
$(La_{1.6}Ba_{0.4})BaMn_2O_7$		3.24	16.22
$(La_{1.5}Ba_{0.5})BaMn_2O_7$		3.12	19.55
$(La_{1.8}Ba_{0.2})BaMn_2O_7$	1500 ^o C	2.61	16.06
$(La_{1.7}Ba_{0.3})BaMn_2O_7$		1.337	16.89
$(La_{1.6}Ba_{0.4})BaMn_2O_7$		2.97	14.35
$(La_{1.5}Ba_{0.5})BaMn_2O_7$		2.83	17.99

4.5.2 Magnetoresistance of $(La_{2-x}Nd_x)BaMn_2O_7$

4.5.2.1 $MR(T)$ for $(La_{2-x}Nd_x)BaMn_2O_7$

The MR as a function of temperature for $(La_{2-x}Nd_x)BaMn_2O_7$ polycrystalline samples is shown in Figure-4.26 and Figure-4.27. In these figures, we have shown $MR(T)$ of $(La_{2-x}Ba_x)BaMn_2O_7$ polycrystalline samples sintered at 1400^oC and 1500^oC. The $MR(T)$ curve was taken in presence of 0.65T applied magnetic field. It is found that the samples show intrinsic peak MR and also extrinsic low temperature MR . The peak temperature of $MR(T)$ is higher than that of the T_p observed in the $\rho(T)/\rho(RT)$ curves. This is because; the presence of magnetic field accelerated the $M-I$ transition, as a result $M-I$ transition occurs at some elevated temperature. The intrinsic MR is found in the manganite due to the fact that for these samples $M-I$ transition is accompanied with the ferromagnetic to paramagnetic transition [3,4]. The extrinsic MR observed at low temperature for this polycrystalline samples is due to the grain boundaries. This type of extrinsic MR is not present for single crystal manganite [5].

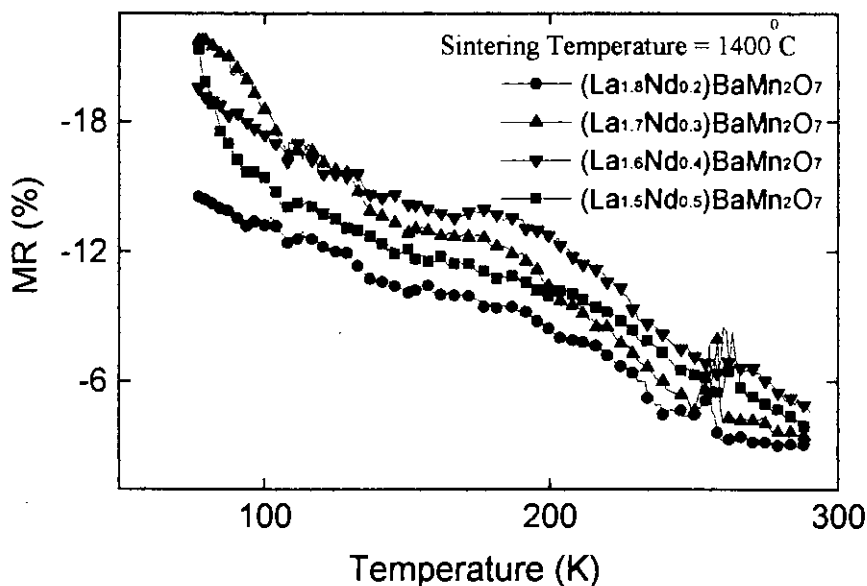


Figure 4.26 : MR as a function of temperature for various (La_{2-x}Nd_x)BaMn₂O₇ polycrystalline samples sintered at 1400°C in air.

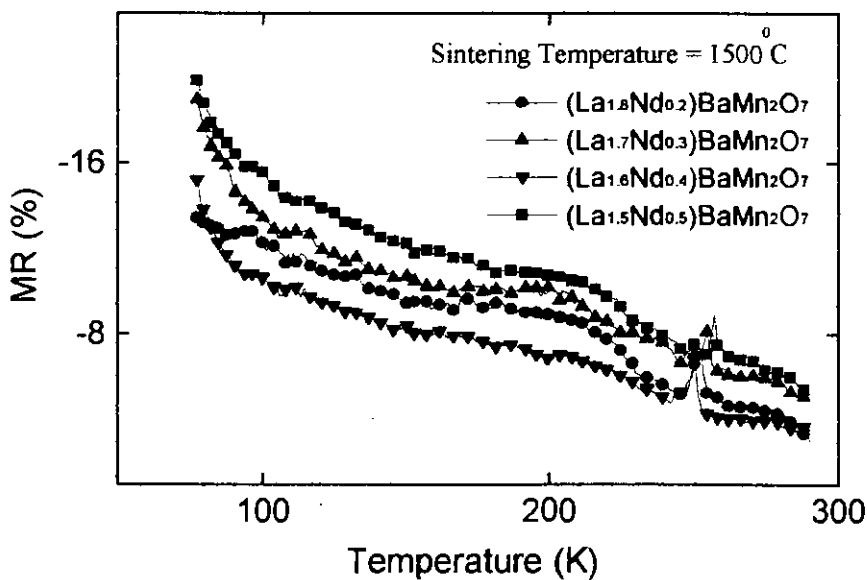


Figure 4.27 : MR as a function of temperature for various (La_{2-x}Nd_x)BaMn₂O₇ polycrystalline samples sintered at 1500°C in air.

4.5.2.2 MR (H) for $(La_{2-x}Nd_x)BaMn_2O_7$

The magnetoresistance (MR) as a function of magnetic field for various $(La_{2-x}Nd_x)BaMn_2O_7$ samples sintered at $1400^{\circ}C$ and $1500^{\circ}C$ was measured at room temperature and at $77K$. Figure 4.28 and Figure 4.29 show MR as a function of magnetic field at room temperature. The observed MR is very low with a maximum value of 5.25% and is almost linear with the applied field as shown in Figures-4.28 and 4.29. This linear increase in MR is due to the suppression of spin fluctuations with the applied field. The results of MR curve are summarised in Table 4.7.

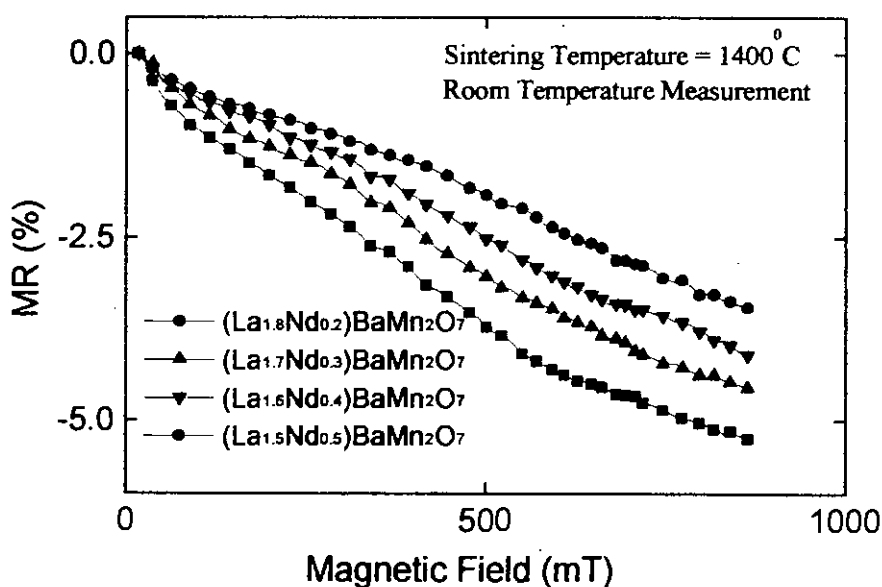


Figure 4.28 : MR as a function of magnetic field at room temperature for various $(La_{2-x}Nd_x)BaMn_2O_7$ polycrystalline samples sintered at $1400^{\circ}C$ in air.

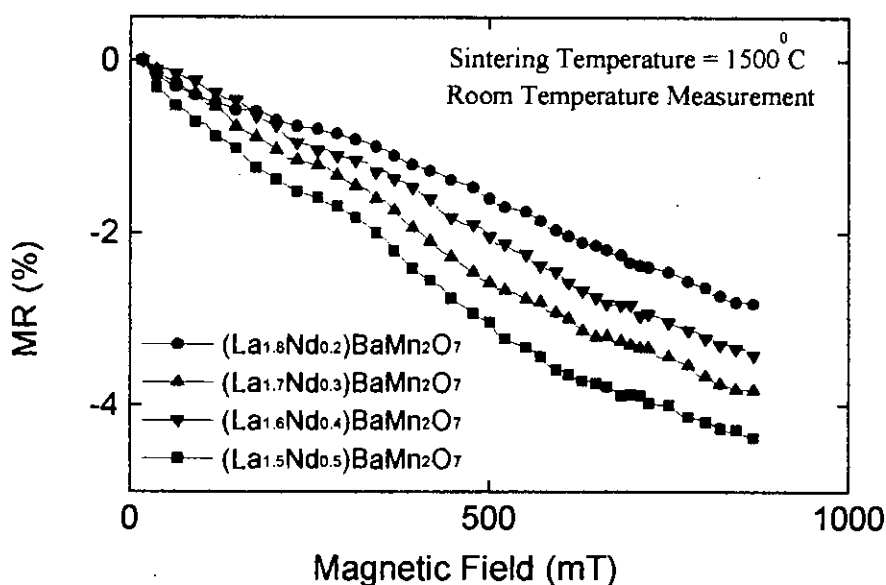


Figure 4.29 : MR as a function of magnetic field at room temperature for various $(La_{2-x}Nd_x)BaMn_2O_7$ polycrystalline samples sintered at 1500°C in air.

The MR at 77K for the samples sintered at 1400°C and 1500°C are shown in Figure 4.30 and Figure 4.31 respectively. From these figures, it is observed that all samples exhibit MR with a maximum value about 22.34% at 77K . The MR in these polycrystalline samples exhibit two distinct regimes as a function of magnetic field. Highly sensitive low field MR is observed up to an applied magnetic field H^* (indicated in the graph). For these $((La_{2-x}Nd_x)BaMn_2O_7)$ polycrystalline samples $H^* \approx 0.109\text{ T}$ and about 16% MR is seen at H^* at 77K . For $H < H^*$, the MR changes rapidly with H followed by a gradual change as H is increased further. Beyond H^* , MR is a weak function of the applied magnetic field. This may be due to the reason that as the material is subdivided into domains, low field is quite sufficient to align the domains spins and thus a sharp decrease in MR is observed but to align the spins at the domain boundary requires much larger field leading to weak field dependence. The results of $\%MR$ curve are summarised in Table 4.7.

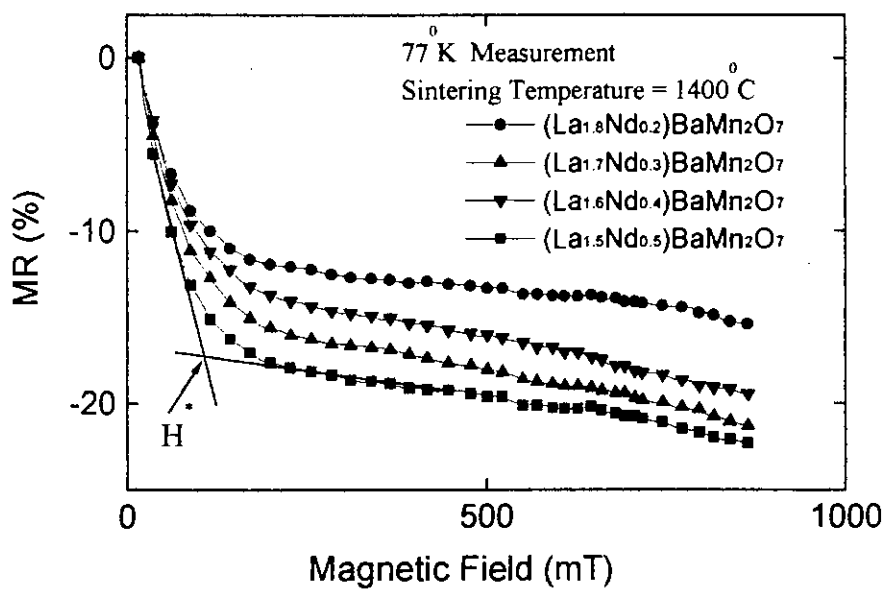


Figure 4.30 : MR as a function of magnetic field at 77K for various $(La_{2-x}Nd_x)BaMn_2O_7$ polycrystalline samples sintered at 1400°C in air.

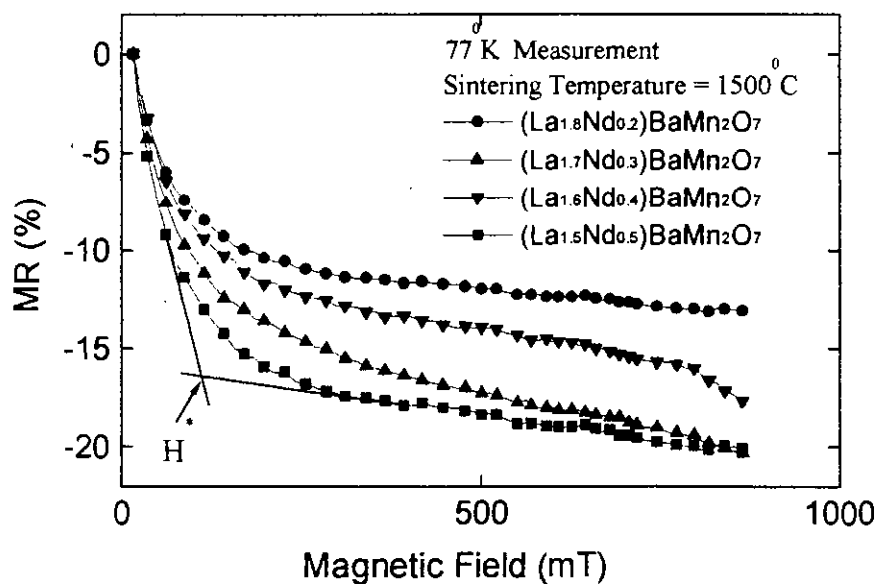


Figure 4.31 : MR as a function of magnetic field at 77K for various $(La_{2-x}Nd_x)BaMn_2O_7$ polycrystalline samples sintered at 1500°C in air.

Table 4.7: The % MR curve for various $(La_{2-x}Nd_x)BaMn_2O_7$ polycrystalline samples sintered at $1500^{\circ}C$ in air.

Sample Composition	Sintering Condition	%MR at room temperature	%MR at 77K
$(La_{1.8}Nd_{0.2})BaMn_2O_7$	$1400^{\circ}C$	3.45	15.45
$(La_{1.7}Nd_{0.3})BaMn_2O_7$		4.55	21.34
$(La_{1.6}Nd_{0.4})BaMn_2O_7$		4.41	19.47
$(La_{1.5}Nd_{0.5})BaMn_2O_7$		5.25	22.34
$(La_{1.8}Nd_{0.2})BaMn_2O_7$	$1500^{\circ}C$	2.82	13.05
$(La_{1.7}Nd_{0.3})BaMn_2O_7$		3.83	20.32
$(La_{1.6}Nd_{0.4})BaMn_2O_7$		3.42	17.65
$(La_{1.5}Nd_{0.5})BaMn_2O_7$		4.38	20.08

4.5.3 Magnetoresistance of $(La_{1.8}Nd_{0.2})(Ba_{1-y}Ca_y)Mn_2O_7$

4.5.3.1 $MR(T)$ for $(La_{1.8}Nd_{0.2})(Ba_{1-y}Ca_y)Mn_2O_7$

The MR as a function of temperature for $(La_{1.8}Nd_{0.2})(Ba_{1-y}Ca_y)Mn_2O_7$ polycrystalline samples are shown in figure-4.32 and figure-4.33. In these figures, we have shown $MR(T)$ of $(La_{1.8}Nd_{0.2})(Ba_{1-y}Ca_y)Mn_2O_7$ polycrystalline samples sintered at $1400^{\circ}C$ and $1500^{\circ}C$. The $MR(T)$ curve was taken in presence of 0.65T applied magnetic field. The intrinsic MR is found in this manganite due to the fact that for this samples $M-I$ transition is accompanied with the ferromagnetic to paramagnetic transition [3,4]. The extrinsic MR observe at low temperature for this polycrystalline samples is due to the grain boundaries. This type of extrinsic MR is not present for single crystal manganite [5].

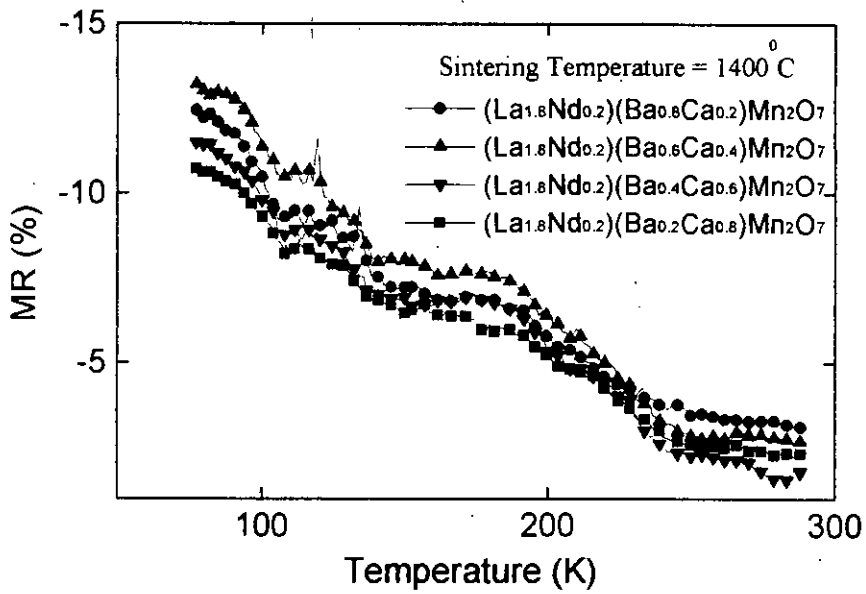


Figure 4.32 : MR as a function of temperature for various (La_{2-x}Nd_x)(Ba_{1-y}Ca_y)Mn₂O₇ polycrystalline samples sintered at 1400^oC in air.

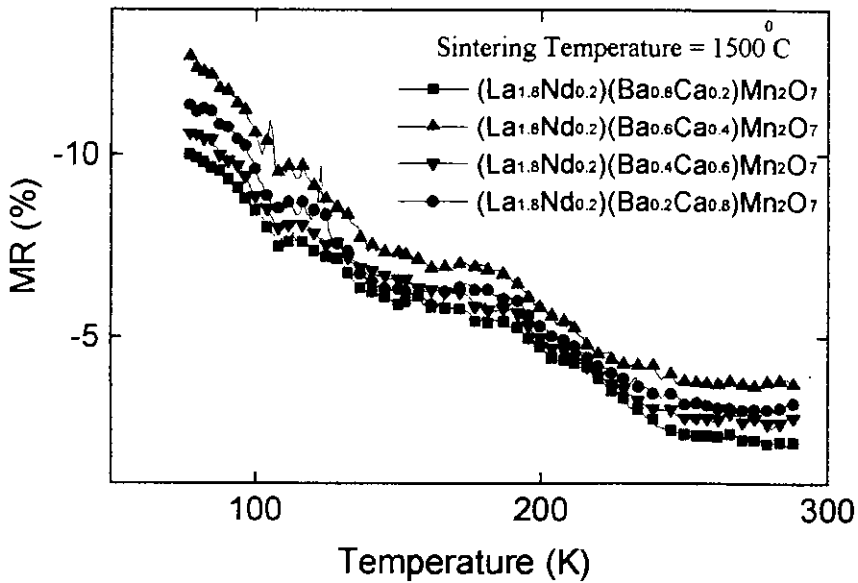


Figure 4.33 : MR as a function of temperature for various (La_{2-x}Nd_x)(Ba_{1-y}Ca_y)Mn₂O₇ polycrystalline samples sintered at 1500^oC in air.

4.5.3.2 $MR(H)$ for $(La_{1.8}Nd_{0.2})(Ba_{1-y}Ca_y)Mn_2O_7$

The magnetoresistance (MR) as a function of magnetic field for various $(La_{1.8}Nd_{0.2})(Ba_{1-y}Ca_y)Mn_2O_7$ samples sintered at $1400^{\circ}C$ and $1500^{\circ}C$ was measured at room temperature and at $77K$. Figure 4.34 and Figure-4.35 show MR as a function of magnetic field at room temperature. The observed MR is very low with a maximum value of 4.55% and is almost linear with field as shown in Figures 4.34 and 4.35. This linear increases in MR is due to the suppression of spin fluctuations with the applied field. The results of MR curve are summarised in Table 4.8.

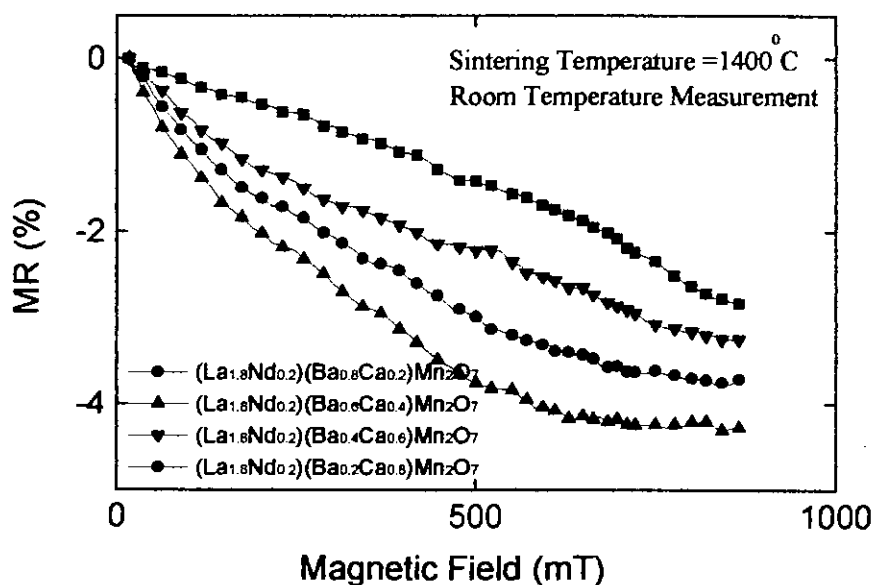


Figure 4.34 : MR as a function of magnetic field at room temperature for various $(La_{1.8}Nd_{0.2})(Ba_{1-y}Ca_y)Mn_2O_7$ polycrystalline samples sintered at $1400^{\circ}C$ in air.

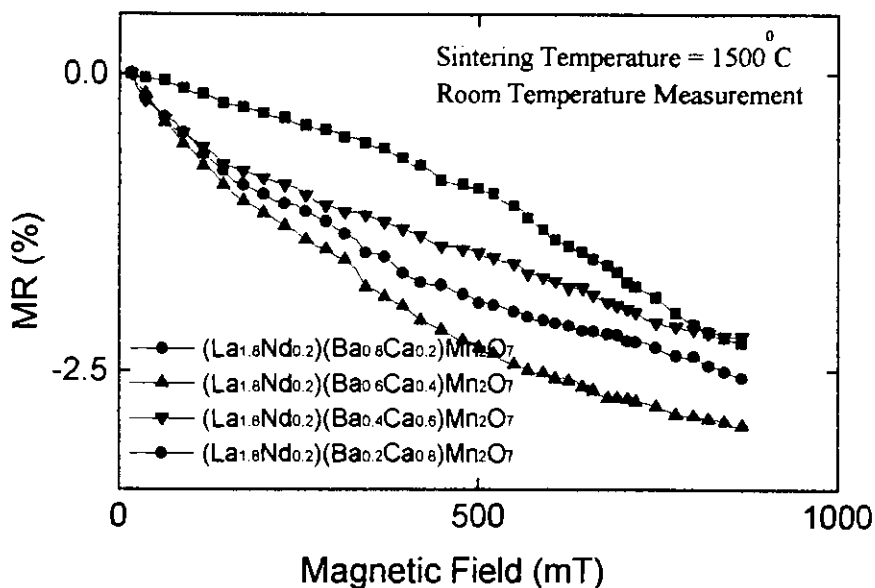


Figure 4.35 : MR as a function of magnetic field at room temperature for various $(\text{La}_{1.8}\text{Nd}_{0.2})(\text{Ba}_{1-y}\text{Ca}_y)\text{Mn}_2\text{O}_7$ polycrystalline samples sintered at 1500^oC in air.

The *MR* at 77K for the samples sintered at 1400^oC and 1500^oC are shown in Figure 4.36 and Figure 4.37 respectively. From these figures, it is observed that all samples exhibit *MR* with a maximum value about 13.43% at 77K. The *MR* in these polycrystalline samples exhibit two distinct regimes as a function of magnetic field. Highly sensitive low field *MR* is observed up to an applied magnetic field H^* (indicated in the graph). For these $(\text{La}_{1.8}\text{Nd}_{0.2})(\text{Ba}_{1-y}\text{Ca}_y)\text{Mn}_2\text{O}_7$ polycrystalline samples $H^* \approx 0.139$ T and about 9.15% *MR* is seen at H^* at 77K. For $H < H^*$, the *MR* changes rapidly with H followed by a gradual change as H is increased further. Beyond H^* , *MR* is a weak function of applied magnetic field. This may be due to the reason that as the material is subdivided into domains, low field is quite sufficient to align the domains spins and thus a sharp decrease in *MR* is observed but to align the spins at the domain boundary requires much larger field leading to weak field dependence. The results of %*MR* curve are summarised in Table 4.8.

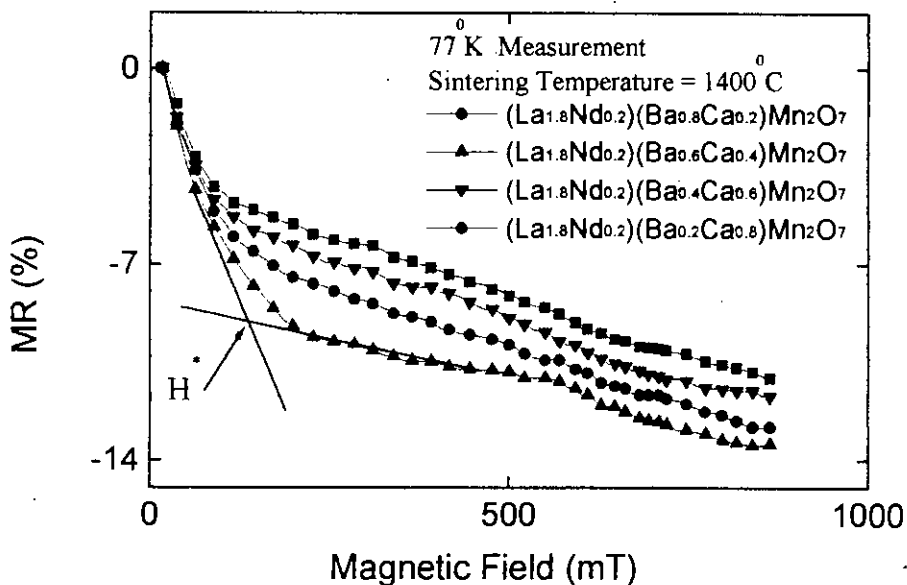


Figure 4.36 : MR as a function of magnetic field at 77K for various $(La_{1.8}Nd_{0.2})(Ba_{1-y}Ca_y)Mn_2O_7$ polycrystalline samples sintered at 1400°C in air.

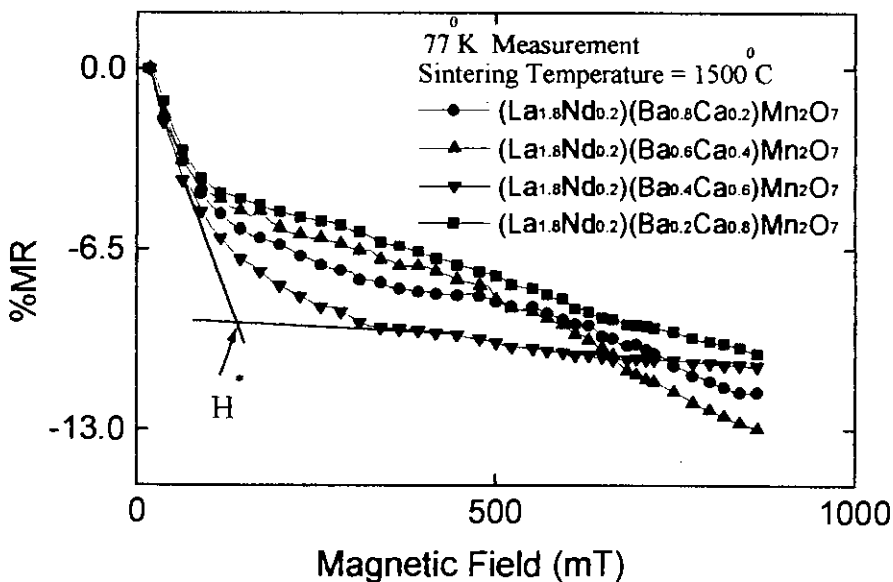


Figure 4.37: MR as a function of magnetic field at 77K for various $(La_{1.8}Nd_{0.2})(Ba_{1-y}Ca_y)Mn_2O_7$ polycrystalline samples sintered at 1500°C in air.

Table 4.8 : The % MR curve for various $(La_{1.8}Nd_{0.2})(Ba_{1-y}Ca_y)Mn_2O_7$ polycrystalline samples.

Sample Composition	Sintering Condition	%MR at room temperature	%MR at 77K
$(La_{1.8}Nd_{0.2})(Ba_{0.8}Ca_{0.2})Mn_2O_7$	1400 ^o C	3.71	12.82
$(La_{1.8}Nd_{0.2})(Ba_{0.6}Ca_{0.4})Mn_2O_7$		4.28	13.43
$(La_{1.8}Nd_{0.2})(Ba_{0.4}Ca_{0.6})Mn_2O_7$		3.25	11.72
$(La_{1.8}Nd_{0.2})(Ba_{0.2}Ca_{0.8})Mn_2O_7$		2.83	11.09
$(La_{1.8}Nd_{0.2})(Ba_{0.8}Ca_{0.2})Mn_2O_7$	1500 ^o C	2.56	11.65
$(La_{1.8}Nd_{0.2})(Ba_{0.6}Ca_{0.4})Mn_2O_7$		2.96	12.96
$(La_{1.8}Nd_{0.2})(Ba_{0.4}Ca_{0.6})Mn_2O_7$		2.21	10.71
$(La_{1.8}Nd_{0.2})(Ba_{0.2}Ca_{0.8})Mn_2O_7$		2.26	10.27

4.6 Explanation of the extrinsic *MR*

From the literature it is observed that two types of *MR* are observed for mixed valence manganite samples. The intrinsic *MR*, which is due to the semiconductor-metal transition along with paramagnetic to ferromagnetic transition, can be explain with the help of double exchange model [6]. This is also known, as intrinsic *MR*. Other *MR* is extrinsic. From the section 4.4, it is observed that almost all samples show extrinsic *MR*. This extrinsic *MR* can be observed only in polycrystalline samples and is absent in single crystal samples. In our studies, we have observed that this extrinsic *MR* strongly depends on the grain size of the samples. Moreover, at low temperatures this extrinsic *MR* show two slopes as a function of applied fields. The two slopes *MR* at low temperature can be explained with the help of the following grain and grain boundary model by *Hossain et al* [3].

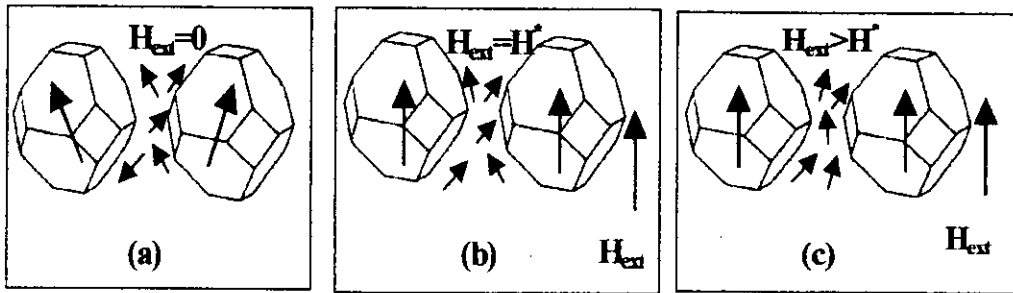


Figure 4.38 : Explanation of the two slopes MR at low Temperature ($T < T_c$)

At $T \ll T_c$ (T_c is the paramagnetic to ferromagnetic transition temperature which is close to the T_{p1}) the material is in the ferromagnetic regime. However, in the absence of field the magnetisation of the grain of the polycrystalline material will be like that in figure 4.38(a). Also, the individual spins at the grain boundary region are randomly oriented. In the absence of field, a carrier will suffer scattering from the unaligned magnetic domain, as well as disordered spin at the grain boundary region. By applying a low magnetic field, the magnetisation of each grain starts to align towards the direction of the external magnetic field direction as shown in figure 4.38(b). However, a large magnetic field is required to align the spins of the grain boundaries as shown in figure 4.38(c).

References

- [1] G.H. Jonker and J.H. Van Santen, *Physica* **16** 337 (1950)
- [2] E. O. Wollan and W. C. Koehler, *Phys. Rev.* **100**, 545 (1955)
- [3] A. K. M. Akther Hossain, L. F. Cohen, F. Damay, A. Berenov, J. L. MacManus-Driscoll, N. McN. Alford, N. D. Mathur, M. G. Blamire & J. E. Evetts, *J. Magnetism and Magnetic Materials*, **192(2)**, 263 (1999).
- [4] A. K. M. Akther Hossain, L. F. Cohen, A. Berenov & J. L. MacManus-Driscoll, *Materials Science & Engineering*, **83**, 79 (2001).
- [5] A. Urshibara, Y. Moritomo, T. Arima, A. Asamitsu, G. Kido & Y. Tokura, *Phys. Rev.* **B51**, 14103 (1995)
- [6] C. Zener, *Phys. Rev.*, **81**, 440 (1951)
- [7] H. Y. Hwang, S.-W. Cheong, P. G. Radaelli, M. Marezio & B. Batlogg, *Phys. Rev. Lett.* **75** (2), 914 (1995).
- [8] J. L. Garcia-Munoz, J. Fontcuberta, M. Suaaidi, & X. Obradors, *J. of Phys.: Cond. Matt.* **8**, L787 (1996a).
- [9] P. S. I. P. N. de Silva, F. M. Richards, L. F. Cohen, J. A. Alonso, M. J. Martinez-Lope, M. T. Casais, T. Kodenkandath & J. L. MacManus-Driscoll, *J. App. Phys.* **83** (1), 394 (1998).
- [10] J. L. Garcia-Munoz, J. Fontcuberta, B. Martinez, A. Seffar, S. Pinol & X. Obradors, *Phys. Rev. B* **55** (2), R-668 (1997).
- [11] M. Lide, Rodriguez-Martinez and J. Paul Attfield, *Phys. Rev. B* **58** (5), 2426 (1998).

Chapter 5

Conclusions

In the present study, the polycrystalline $(La_{2-x}Nd_x)(Ba_{1-y}Ca_y)Mn_2O_7$ samples were prepared by standard solid state reaction method. The samples were sintered at two different temperatures $1400^{\circ}C$ and $1500^{\circ}C$ in air. X-ray diffraction analysis was performed on these samples to examine phase purity. It is clear from the XRD pattern that the samples are crystalline and single phase.

The DC electrical resistivity for various $(La_{2-x}Nd_x)(Ba_{1-y}Ca_y)Mn_2O_7$ polycrystalline samples were measured by using standard four point probe method using vander Pauw technique from room temperature down to liquid nitrogen temperature. The temperature dependence of normalized resistivity $\rho(T)/\rho(RT)$, at zero and 0.65T applied magnetic field for various $(La_{2-x}Nd_x)(Ba_{1-y}Ca_y)Mn_2O_7$ polycrystalline samples sintered at $1400^{\circ}C$ and $1500^{\circ}C$ were investigated. It is found that all samples show a peak in the $\rho(T)/\rho(RT)$ curves at T_p , where a metal-insulator (*M-I*) transition occur.

The *M-I* transition temperature for samples of $(La_{2-x}Ba_x)BaMn_2O_7$ increase with the increase of Ba concentration up to $x=0.4$. Beyond $x=0.4$ of Ba concentration, the transition temperature decrease slightly. This is due to, when La is substituted by Ba, the valance state of some Mn^{3+} ions change to Mn^{4+} ions. So the increase of transition temperature with increase of Ba concentration up to $x=0.4$ is most probably due to the coupling between Mn^{3+} and Ba^{2+} favoring ferromagnetic. The decrease of transition temperature for beyond Ba of $x=0.4$, is probably due to the anti-ferromagnetic coupling between Mn^{3+} and Ba^{2+} ions. Besides, the larger atomic diameter of Ba compared to La may be a added factor.

The *M-I* transition temperature for samples of $(La_{2-x}Nd_x)BaMn_2O_7$ increase with the increase of Nd concentration. This is due to the interaction mechanism between the manganese ions that occur via oxygen ions. Since the *M-I* transition temperature is related to the Mn-O-Mn angle and the Mn-Mn transfer integral. The *M-I* transition temperature change by bending the Mn-O-Mn angle. As the atomic diameter of Nd is smaller than that of La, so substitution of La by Nd favoring of changing the bond angle between Mn-O-Mn ions, there by the *M-I* transition temperature increase with the increase of Nd concentration.

The samples of $(La_{1.8}Nd_{0.2})(Ba_{1-y}Ca_y)Mn_2O_7$ exhibit a metal-insulator ($M-I$) transition for $y=0.2$ and 0.4 but for $y=0.6$ and 0.8 , the samples show an antiferromagnetic insulator behavior. This may be due to, when Ba is substituted by Ca seem to enhance the insulator phase. This means, the electron transfer between the manganese site via Oxygen is hampered.

So, doping by La and Nd favor of increase the transition temperature of the samples, but doping by Ca does not so. The $M-I$ transition occur at different temperature depending on the different composition of samples. The variation of T_p is due to the composition of the samples.

The $M-I$ transition temperature for all the composition of samples enhance by few Kelvin in the presence of $0.65T$ applied magnetic field, as the applied field accelerate magnetic ordering. The resistivity of the samples decrease throughout the measured temperature range with the increase of sintering temperature. This is probably due to the increase of grain size of the samples, which result in decrease in the grain boundary.

All compositions of samples show temperature dependent of $MR(T)$ in presence of $0.65T$ applied magnetic field. Also all samples show field dependent of $MR(H)$ both at room temperature and liquid nitrogen ($77K$) temperature. All samples show almost a linear increase of $MR(H)$ with the increase of applied magnetic field at room temperature. This linear increase of MR is due to the suppression of spin fluctuation with the applied field.

The $MR(H)$ at liquid nitrogen temperature exhibit two slopes in $MR(H)$ curves for all compositions of samples. The applied field H^* designate the boundary of the two slopes. Highly sensitive low field MR is observed up to an applied magnetic field H^* . For $H < H^*$, the MR change rapidly with H followed by a gradual change as H is increased further. But for $H > H^*$, MR has a weak function of the applied magnetic field. This may be due to the reason that as the material is subdivided into domains, low field is quite sufficient to align the domain spins and thus a sharp decrease in MR is observed but to align the spins at the domains boundary require much larger field leading to a weak field dependence.

